UC Berkeley
UC Berkeley Electronic Theses and Dissertations

Title
Texture Development and Polycrystal Plasticity of Two-Phase Aggregates

Permalink
https://escholarship.org/uc/item/2tg1s46z

Author
Zepeda-Alarcon, Eloisa

Publication Date
2017

Peer reviewed|Thesis/dissertation

eScholarship.org Powered by the California Digital Library
University of California

Texture Development and Polycrystal Plasticity of Two-Phase Aggregates

by

Eloisa Zepeda-Alarcon

A dissertation submitted in partial satisfaction of the
requirements for the degree of
Doctor of Philosophy

in

Earth and Planetary Science

in the

Graduate Division

of the

University of California, Berkeley

Committee in charge:

Professor Hans-Rudolf Wenk, Chair
Professor Bruce Buffett
Professor Andrew Minor

Summer 2017

Texture Development and Polycrystal Plasticity of Two-Phase Aggregates

Copyright 2017
by
Eloisa Zepeda-Alarcon

Abstract

Texture Development and Polycrystal Plasticity of Two-Phase Aggregates

by

Eloisa Zepeda-Alarcon

Doctor of Philosophy in Earth and Planetary Science

University of California, Berkeley

Professor Hans-Rudolf Wenk, Chair

The vast majority of rocks that constitute the Earth are composed of multiple mineral phases and complicated deformation conditions are found everywhere, yet little is known about plastic deformation of polyphase polycrystalline rocks, especially with low symmetry phases and highly contrasting mechanical properties. In particular, plastic deformation of mantle rocks is of interest for its connection to geophysical processes, such as mantle convection, slab subduction and upwelling plumes. Seismic observations show regions in the mantle where seismic waves encounter large scale anisotropy of the rocks they propagate in. Although there are many possible reasons for this large scale anisotropic signature of these particular regions, in the upper mantle it has been connected to the development of crystallographic preferred orientation, hereafter called *texture*, of the mineral olivine due to plastic deformation produced by specific geodynamical processes. Studies have also connected measured seismic anisotropy to texture in the minerals that compose the core mantle boundary region, in the mantle transition zone and in the core of the Earth. Deformation of lower mantle minerals is still poorly understood. Although large convective cells, upwhelling plumes and subducted slabs are expected, the bulk of the lower mantle remains seismically isotropic. The lower mantle is mainly composed of the mineral bridgmanite and ferropericlase, with a small volume fraction of Ca-Si-perovskite. Understanding plastic deformation of the bridgmanite and ferropericlase mineral aggregate can provide valuable information to better understand lower mantle dynamics, and to explain seismic observations. The objective of this dissertation is to explore plastic deformation of bridgmanite and periclase polycrystalline aggregates from both modeling and experimental approaches. In particular to understand the influence of microstructure in texture development and the role of deformation heterogeneities at the local grain scale.

A finite element framework is used in Chapter 2 to explore plastic deformation by dislocation glide of a virtual two phase polycrystal with a random microstructure. Aggregates are deformed up to 20% strain under uniaxial compression and two different simulations where performed using the FEpX code, one where the yield strength of both phases is

the same, and the second where the yield strength of the bridgmanite phase is 8 times higher than the periclase. This approach enabled the investigation of the effects of yield strength contrast in the mechanical response of the phases under uniaxial compression. Trends in texture development, plastic deformation rates and intragranular misorientation distributions are analyzed. Single phase bridgmanite and single phase periclase simulations were also performed for comparison with their two phase counterparts. It is found that both the bridgmanite and periclase phase develop weak texture in both the single and two phase simulations. Distributions of the plastic deformation rate show that as the yield strength contrast is increased in the two phase simulations, heterogeneities in the distribution of the plastic deformation rate across the bulk of the sample increase drastically. However, a wider distribution of the plastic deformation rate is observed in the single phase bridgmanite simulation, than in the two phase simulation where both phases have the same yield strength. This indicates that deformation heterogeneities in bridgmanite are mainly due to the high anisotropy of its single phase mechanical properties. Misorientation of each element in a grain with respect to the grain average orientation is calculated and statistical trends of the grains of the bridgmanite phase and the periclase phase are analyzed separately and compared. While misorientation distributions for the bridgmanite phase remain very similar across the different simulations, misorientation distributions of the periclase phase become much wider and with a larger mean misorientation as the yield strength contrast is increased. In addition, the distribution of misorientations in the periclase phase when deformed on its own is the narrowest of them all, indicating that deformation heterogeneities in the periclase phase are introduced by deforming in the two phase scenario with a harder phase. Slip system activity calculations show most of the deformation by dislocation slip is carried by the periclase phase in the two phase simulation with large yield strength contrast.

A fast Fourier transform formulation implemented in the VPFFT code is used in Chapter 3 to study the effects of microstructure in texture development of a two phase polycrystalline aggregate composed of 75% bridgmanite and 25% periclase, and also single phase simulations for comparison. Using this approach, it is also found that bridgmanite and periclase develop weak texture, even when deformed as single phase aggregates. Furthermore, it is observed that there is little microstructure dependence of the texture and strain rate distributions for a microstructure where periclase is at the cores of bridgmanite grains, one where grains of both phases are randomly distributed across the aggregate and one where periclase grains are at triple junctions of the bridgmanite grains. A microstructure where periclase grains is percolating around bridgmanite grains is found to be the outlier of this study, it develops very strong texture in the bridgmanite phase and presents sharper distributions of the strain rate in this phase than the other tested microstructures, indicating a microstructure dependance of the deformation of bridgmanite in this case. Since grains are discretized into smaller elements, statistical trends in the distribution of strain rates of regions at grain boundaries and regions in interior of grains can be compared. It is found that in two phase simulations, regions at grains boundaries in grains of the periclase phase develop the widest distribution of strain rate values, suggesting that deformation heterogeneities are mainly concentrated in

these regions.

High pressure diamond anvil cell experiments were performed on the bridgmanite + periclase two phase system to explore texture development at high pressure due to dislocation slip. Diamond anvil cell experiments were performed in synchrotron x-ray sources, where 2D diffraction patterns are collected and samples are laser heated to induce phase transformations at high pressures. The sample grains sizes that were previously possible to analyze using the traditional Rietveld technique were limited to grain sizes that produced smooth powder diffraction patters in order to analyze intensity variations along Debye rings and determine the texture developed in the sample. Recently the high pressure diamond anvil cell community has adopted a more novel multigrain data collection and analysis technique, where diffraction images with sharp diffraction spots originating from multiple grains can be indexed and clusters in orientation space are searched to correlate multiple diffraction spots with the particular grain they originate from. Applying this data collection technique presents challenges in the diamond anvil cell, in particular when non hydrostatic conditions are desired for texture development studies. The small rotation angle accessible to the diamond anvil cell, peak overlap due to plastic deformation in the grains and low intensity of diffraction spots due to weakly diffracting materials are some of the challenges encountered in these experiments. An overview of the implementation of this data collection and analysis technique to the diamond anvil cell for texture studies, together with some preliminary results, is presented in Chapter 4.

To the millennia and physical forces that shape our world

Without them there is no polycrystal plasticity in the interior of the Earth, and no polyphase aggregates to study.

To Xiaani, may the fight for a better world never end.

Contents

Contents **ii**

1 Introduction **1**

2 Finite Element Modeling with FEpX **11**
2.1 Introduction 12
2.2 Simulation Method 13
2.3 Results 16
2.4 Discussion 23
2.5 Conclusions 26

3 Polycrystal Plasticity with the VPFFT Code **30**
3.1 Introduction 30
3.2 Methods 31
3.3 Results 44
3.4 Discussion 53
3.5 Conclusion 58

4 Multigrain Crystallography **64**
4.1 Introduction 64
4.2 Experimental Methods 66
4.3 The HEXRD Multigrain Analysis Software 72
4.4 Preliminary Results 96
4.5 Discussion and Conclusions 100

5 Concluding Remarks **105**

A FEpX Postprocessing Scripts **110**

B VPFFT Postprocessing Scripts **123**

Acknowledgments

Hans-Rudolf Wenk, an outstanding advisor, thanks to him this is all possible. Carnegie/DOE Alliance Center (CDAC) for funding the majority of my graduate degree, travel to experiments and conferences, and summer internships at Los Alamos National Laboratory and Cornell University. Department of Earth and Planetary Science for full support during my first year of graduate school and all the administrative and academic knowledge and kindly given to me. Paul Dawson in Cornell University for his insight and FEpX code for polycrystal plasticity modeling using a finite element approach. Matthew Kasemer from Cornell University for closely working with me on the FEpX code, solving bugs and problems, and for providing post processing scripts. Matthew Kasemer is the main contributor of Section 2.2 in Chapter 2. Rob Carson from Cornell University for his changes to the FEpX code that enable the use of different CRSS values for the slip systems used in the code. Ricardo Lebensohn and Carlos Tome from Los Alamos National Laboratory (LANL) for their mentorship in my summer internship at LANL, and after, working with the VPFFT code. Jason Knight, Alastair McDowel for work in resistive heating of the diamond anvil cell and support during beamtimes at beamline 12.2.2 of the Advanced Light Source (ALS) at Lawrence Berkeley Laboratory (LBL). Martin Kunz, Andrew Doran, Christine Beavers and Jinyuan Yan for their support at beamtime at 12.2.2 of the ALS. In particular Martin Kunz for his advice, mentoring and sharing expertise for sample preparation and experimental procedures. Jesse Smith, Stanislav Sinogoikin and Guoyin Shen for their support in diamond anvil cell experiments at the HPCAT sector 16 of the Advanced Photon Source at Argonne National Laboratory. Joel Bernier for collaboration during multigrain diamond anvil cell experiments at ALS, and in particular with data analysis using his software HEXRD. Nathan Barton for work done at summer internship in Lawrence Livermore National Laboratory, work is not presented in this dissertation. Sven Vogel, Heinz Nakotte, Katherine Page, Graham King, Mikhail Feygenson, for work on goethite nuclear and magnetic structure, work is not presented in this dissertation. Steve Gramsch and Morgan Philips for their support through CDAC. Jane Kanitpanyacharoen for her mentoring through graduate school and training in diamond anvil cell experiments, and for being a great friend. Lowell Miyagi for discussion on polycrystal plasticity modeling and diamond anvil cell expertise. Pamela Kaercher for team work at beamtimes. Roman N. Vasin for teamwork at beamtimes, discussions about finite element modeling, VPFFT modeling, life, robots, waffles, and for being a great friend.

Chapter 1

Introduction

The interior of the Earth is composed of a series of complex mineral aggregates that are constantly being deformed by shear forces due to mantle convection and are at high pressures and temperatures. Understanding materials at these extreme conditions is crucial for interpreting seismic data and developing informed geophysical models. In particular, seismic data shows that there are large regions in the mantle and core of the Earth that present elastic anisotropy. Previous studies have linked this measured seismic anisotropy to the crystallographic preferred orientation of the mineral aggregates (e.g. Dawson and Wenk, 2000; Wenk et al., 2011; Cottaar et al., 2014). If these mineral aggregates are elastically anisotropic, and they are preferably aligned in a certain direction, seismic waves that propagate through this region will encounter a highly anisotropic mineral aggregate, giving rise to measurable velocity differences in the different propagation directions of the seismic waves. Seismic anisotropy in the mantle can also be due to shape preferred orientation (SPO) of materials with contrasting rheologies (Romanowicz and Wenk, 2017). Understanding the deformation mechanisms that give rise to crystallographic preferred orientation (CPO), also called texture, in these mantle mineral aggregates can help interpret seismic anisotropy data and make connections withe the direction of flow in that region of the mantle (Miyagi et al., 2010). There are a few reasons why polycrystalline aggregates can develop texture. It can be due to plastic deformation by lattice rotation due to dislocation glide or grain boundary migration, recrystallization under an applied stress can also develop a texture, grain nucleation in preferred orientations and growth due to grain boundary migration (Karato, 2013). The study presented here concentrates in the development of texture due to dislocation glide by means of different modeling efforts, and explores new techniques to experimentally quantify texture development in polycrystals deformed at high pressure under compression in a diamond anvil cell.

Seismic waves enable us to probe the elastic properties of the interior of the Earth. There are discontinuities in the propagation of seismic waves through the Earth, which indicate that there are distinct layers with different elastic properties (Dziewonski and Anderson, 1981). Observations of material exposed by tectonic activity and volcanic eruptions suggest that

the upper mantle has a peridotite composition, where the mineral olivine is a predominant phase (McDonough and Sun, 1995). As we go deeper in the mantle, pressure and temperature increase inducing phase transformations of mantle minerals. These new phases have different elastic properties and are held responsible for the discontinuities observed seismically (Birch, 1952). Ringwood (1962) suggested that olivine Mg_2SiO_4 would transform to a denser polymorph, wadsleyite, plus stishovite around 400Km depth. As the pressure increases at around 600 km deep, olivine inverts to a spinel structure with the same composition Mg_2SiO_4, now named ringwoodite. Finally, Ringwood (1962) predicts that the spinel breaks down into denser, close packed phases, $MgSiO_3$ with a corundum structure plus periclase (MgO). The $MgSiO_3$ corundum structure predicted by Ringwood (1962) was synthesized at high pressure and temperature by Liu (1974) and found it to have an orthorhombic perovskite structure. This phase has recently been found in a shocked meteorite and named bridgmanite (Tschauner et al., 2014). Bridgmanite transforms to post-perovskite at high pressure, and it is probably the most important mineral phase near the cold mantle boundary (e.g Murakami et al., 2004; Ohtani and Sakai, 2008). Although a number of minority phases exist, bridgmanite + ferropericlase are the main mineral components of the bulk of the lower mantle (Irifune and Tsuchiya, 2015).

Seismic anisotropy is the direction dependent propagation of seismic waves. In general, to produce observable anisotropy in the mantle it is necessary for deformation to either align individual crystallites producing CPO or align inclusions (like pores, fractures or melt) with contrasting elastic properties producing SPO (Romanowicz and Wenk, 2017). Although in cold regions of the mantle this deformation can be frozen in over geologic time scales, in hotter regions it is most likely that this anisotropy indicates the presence of high strains that could be due to the flow of mantle materials (Becker et al., 2003; Lin et al., 2011). In order to interpret seismic anisotropy in relation to mantle convection, it is important to determine the deformation behavior of mantle minerals. In particular to understand deformation by dislocation slip and its connection to CPO development (Cottaar et al., 2014).

The structure of mantle flow has been a long standing problem that remains controversial. In general terms there are two proposed scenarios, one where convection cells flow through the whole mantle and another is where the transition zone acts as a mid-mantle boundary layer that impedes the pass of subducting slabs or upwhelling plumes. Current and past tectonic plate subduction zones have been found to correlate with seismically imaged and tomographically observed regions with higher than average seismic wave speeds in the deep lower mantle (Romanowicz and Wenk, 2017). This spatial correlation is consistent with the idea of descending lithosphere that is colder than its surroundings. Furthermore, locations of hotspot volcanism have been spatially correlated with regions of lower than average wave speeds in the deep mantle (Garnero et al., 2016). In addition to tomographic imaging of subducting lithosphere descending into the lower mantle in some regions, these aforementioned spatial correlations has led to a greater acceptance of whole mantle convection.

Global models of seismic anisotropy agree on a highly anisotropic upper mantle with VSH>VSV starting at about 80 km under oceanic crust and 200 km under continental

lithosphere that is likely due to horizontal mantle flow (Panning and Romanowicz, 2006). As these models look a little deeper in the mantle, about 300 km depth, they find an opposite polarization anisotropy with VSV>VSH beneath major ridge systems suggesting vertical flow. In general, seismic anisotropy in the upper mantle is mainly attributed to CPO in olivine. Although olivine has been extensively studied and its deformation mechanisms well understood, there is still some controversy as to how it deforms in the upper mantle. This controversy is due to the sensitivity of slip systems of olivine with temperature (Katayama and Karato, 2006) and water content (Jung and Karato, 2001), and to uncertainties of these values in the mantle. The vast majority of results report slip in the [100] direction while the others agree with [001] slip directions (Mainprice, 2015). Depending on the dominant slip system activity is the resulting CPO upon deformation, and the resulting potential seismic anisotropy in the mantle. Independent of this controversy, seismic anisotropy in the upper mantle is highly correlated to tectonic activity and subducting slabs, suggesting that plastic deformation of mantle minerals and subsequent texture development is responsible of the observed anisotropy (e.g. Lin et al., 2011).

The transition zone is defined by two large seismic discontinuities at 410 km and 660 km, they are associated with the phase transition of olivine to wadsleyite, then to ringwoodite and finally to bridgmanite and periclase (Irifune and Tsuchiya, 2015). Although the anisotropic signature of this region is weaker than in the upper mantle, global models have found a correlation of observed VSV>VSH anisotropy with subduction zones at this depth range (Visser et al., 2008; Panning and Romanowicz, 2006). These observations suggest that the vertical flow in subduction zones may lead to the observed anisotropy, which initially can be thought of as a result of CPO and/or SPO of transition zone minerals (Karato, 1998). Karato (1998) shows that it is most likely that anisotropy in this region is due to CPO, since contrasts of elastic properties in coexisting mantle minerals, usually about 10%, would produce a very small anisotropic signature due to SPO or laminated structures.

Complementing the idea of vertical flow in subduction zones presented by global models, regional models have found evidence for horizontal flow in the vicinity of the 660 km discontinuity, suggesting that subducting slabs might be spreading along the transition zone, or even passing through the transition zone and blobbing into the uppermost lower mantle (Wookey et al., 2002). This idea of horizontal flow in the transition zone is supported by deformation experiments on wadsleyite. They have found the [001] axis and the (010) plane subparallel to the shear direction and the shear plane during deformation, suggesting that the observed polarization anisotropy might be attributed to CPO of wadsleyite caused by horizontal mantle flow (Kawazoe et al., 2013). Considering the importance of this region, it becomes necessary to understand not only deformation mechanisms of minerals of the transition zone but also of the lower mantle, namely bridgmanite and periclase, to be able to correlate seismic anisotropy measurements with mantle flow structures.

It has been reported that there is a weak anisotropy with VSV>VSH and VPV>VPH in the lower 660- 1000 km of the mantle (Montagner, 1998). This anisotropy was proposed by Karato (1998) to be due to CPO of perovskite and possibly ferropericlase, obtained by

deformation at the convective boundary layer that the transition zone provides. Karato also points out that the transition from diffusion creep to dislocation creep of MgO and perovskite happens at conditions very close to those of the mantle, which could explain regional pockets of seismic anisotropy, as for example in Wookey et al. (2002), in the uppermost lower mantle. Kawakatsu and Niu (1994) found a discontinuity at 920 km under the Tonga, Japan and Flores sea subduction zones with a 2.4% S wave velocity change. They suggest that the discontinuity can be due to a change in mantle composition or the garnet layer of a subducted slab. From a depth of about 1000 km to 2700 km the mantle is isotropic, although the reason for this remains controversial, high temperature shear experiments on a calcium analog of perovskite show that it deforms by diffusion creep, which does not develop CPO and hence produces no seismic anisotropy (Karato et al., 1995). More recent experimental studies on plastic deformation under uppermost lower-mantle conditions show that $MgSiO_3$ perovskite deforms by dislocation creep and may contribute to seismic anisotropy at these depths (Cordier et al., 2004). In addition, there is no evidence for significant anisotropy in the bulk of the lower mantle (Romanowicz and Wenk, 2017).

The D" region has showed itself to be a very interesting and anisotropic region of the mantle. It is the region above the core mantle boundary and has a thickness that ranges from 60-300 km. It has prominent VSH>VSV anisotropy of about 1% (Panning and Romanowicz, 2006). Although the mineral physics is not well constrained in the D", it suggests that the observed anisotropy is due to horizontal flow under downgoing slabs producing either CPO (McNamara et al., 2002) or SPO. A new high pressure perovskite phase, post-perovskite, has been synthesized and it is believed that it might be stable in the pressure and temperature conditions of D" (Merkel et al., 2007; Miyagi et al., 2010). Experimentally measured CPO development of post-perovskite has a strong correlation with observed anisotropy in this region (Romanowicz and Wenk, 2017; Wenk et al., 2011).

Studies of texture development at high pressure in the bridgmanite + periclase system remain controversial, suggesting that there is a strong dependence with the starting material and possibly microstructure. Wenk et al. (2004) presents experimental radial diamond anvil cell (rDAC) results on axially compressed olivine up to 50GPa at room temperature. Olivine is transformed to the bridgmanite + ferropericlase mixture at about 23GPa and a pronounced (100) transformation texture is reported. As deformation evolves a $\{0\,1\,2\}$ deformation texture develops. Wenk et al. (2004) also find a weak $\langle 1\,1\,1\rangle$ transformation texture in ferropericlase that changes towards a $\langle 0\,0\,1\rangle$ maximum with increasing deformation. A review of a suite of high pressure rDAC deformation experiments on Mg-Si perovskite (now named bridgmanite) is presented in Wenk et al. (2006). Strong deformation textures in bridgmanite form a variety of different starting materials are also reported in this study. In contrast with these findings, Merkel et al. (2003) found no texture development in rDAC experiments on $(Mg_{0.9},Fe_{0.1})SiO_3$ perovskite when synthesized from orthopyroxene in a multi anvil apparatus. More recent rDAC experiments by Miyagi and Wenk (2016) on bridgmanite and bridgmanite + ferropericlase aggregates, from enstatite and olivine or ringwoodite starting materials respectively, find a strong 001 transformation texture in

bridgmanite when deformed as a single phase and a weaker 100 transformation texture when deformed as a two phase aggregate with ferropericlase. It is also reported in this study that ferropericlase, when deformed together with bridgmanite, develops no texture. In addition, simple shear deformation experiments done in a Kawai type deformation-DIA apparatus find that the dominant slip system in bridgmanite is (1 0 0)[0 0 1] at conditions of the uppermost lower mantle (25GPa and 1873K), and explained reported seismic shear wave anisotropy near several subducted slabs with their findings (Tsujino et al., 2016). Girard et al. (2016) conduct high pressure and temperature deformation experiments on bridgmanite and periclase aggregates at shallow lower mantle conditions in a Drickamer apparatus. They found that bridgmanite is considerably stronger than periclase, and that periclase largely accommodates the strain. Their findings explain the lack of seismic anisotropy in the bulk of the lower mantle.

Further investigation into plastic deformation of bridgmanite + ferropericlase is required to explain inconsistencies in past deformation experiments and modeling efforts. In particular the influence of microstructure, yield strength contrast, and the behavior of the local grain environment, on texture development is of interest. In the following chapters, modeling and experimental efforts on plastic deformation and subsequent texture development in bridgmanite + periclase aggregates is presented.

Chapter 2 presents modeling results using a finite element framework. The effect of yield strength contrast on the development of local grain scale heterogeneities in two phase and single phase polycrystalline aggregates with a random microstructure. A weak texture in both bridgmanite and periclase is developed in two phase and single phase simulation under compression up to 20% strain. Plastic deformation rate distributions show large deformation heterogeneities when yield strength contrast is large between the two phases. Moreover, a more narrow distribution of plastic deformation rates is observed when the yield strength of the two phases is equal, than when bridgmanite is deformed as a single phase, indicating that single crystal anisotropy of this low symmetry phase is an important factor in the development of deformation heterogeneities in bridgmanite. Plastic deformation rate distributions in the single phase periclase simulations show a very narrow distribution, indicating that heterogeneities are introduced by being deformed in a polyphase environment. Slip system activity confirms that most of the deformation is carried by the periclase phase when it is softer than bridgmanite, and misorientation distributions confirm this result.

Chapter 3 deals with modeling polyphase polycrystal plastic deformation using a fast Fourier transform formulation. Here the influence of microstructure on texture development in two phase aggregates is explored. Four ideal two phase microstructures were created and deformed under compression up to 30% strain. No microstructure development was observed for three of the tested microstructures and very weak texture was developed in bridgmanite and periclase. In the microstructure where periclase percolates around bridgmanite grains, strong texture in the bridgmanite phase develops and deformation appears to have a strong microstructure dependence. Strain rate distributions analyzed separately for the two different phase and for regions at grain boundaries and in the interior of

grains show that regions at grain boundaries of periclase grains carry most of the deformation.

Application of a novel experimental and data analysis technique in synchrotron x-ray high pressure diamond anvil cell deformation experiments is presented in Chapter 4. It is common in high pressure diamond anvil cell experiments to obtain grain sizes that are large and render unfit for analysis with the traditional Rietveld analysis techniques. This can be due to high temperature studies where grain growth is inevitable, or to having samples with larger grain sizes to start with. High pressure single crystal experiments are also problematic, it is common that the single crystals break, and diffraction signals are recorded from two independent domains. Traditional single crystal x-ray diffraction analysis software is unable to analyze data in such conditions. The multigrain analysis technique is able to analyze data in these conditions where the Rietveld and single crystal formulations fail. The application of this technique to high pressure texture studies in the diamond anvil cell is considered, and preliminary results are shown.

References

Becker, T., Kellog, J., Ekstrom, G., and O'Connell, R. J. (2003). Comparison of azimuthal seismic anisotropy from surface waves and finite strain from global mantle circulation models. *Geophysical Journal International*, 155:696–714.

Birch, F. (1952). Elasticity and constitution of the earth's interior. *Journal of Geophysical Research*, 57:227–286.

Cordier, P., Ungar, T., Zsoldos, L., and Tichy, G. (2004). Dislocation creep in $MgSiO_3$ perovskite at conditions of the earth's uppermost lower mantle. *Nature*, 428:837–840.

Cottaar, S., Li, M., McNamara, A., Romanowicz, B., and Wenk, H.-R. (2014). Synthetic seismic anisotropy models within a slab impinging on the core-mantle boundary. *Geophysical Journal International*, 199:164–177.

Dawson, P. and Wenk, H.-R. (2000). Texturing of the upper mantle during convection. *Philosophical Magazine A*, 80:573–598.

Dziewonski, A. M. and Anderson, D. L. (1981). Preliminary reference earth model. *Physics of the Earth and Planetary Interiors*, 25:297–356.

Garnero, E., McNamara, A., and Shim, S.-H. (2016). Continent-sized anomalus zones with low seismic velocity at the base of the earth's mantle. *Nature Geoscience*, 9:481–489.

Girard, J., Amulele, G., Farla, R., Mohiuddin, A., and Karato, S.-i. (2016). Shear deformation of bridgmanite and magnesiowustite aggregates at lower mantle conditions. *Science*, 351:144–147.

Irifune, T. and Tsuchiya, T. (2015). 2.03 - phase transitions and mineralogy of the lower mantle. In Schubert, G., editor, *Treatise on Geophysics (Second Edition)*, pages 33 – 60. Elsevier, Oxford, second edition edition.

Jung, H. and Karato, S. (2001). Water-induced fabric transitions in olivine. *Science*, 293:1460–1463.

Karato, S.-I. (1998). Seismic anisotropy in the deep mantle, boundary layers and the geometry of mantle convection. *Pure and Applied Geophysics*, 151:565–587.

Karato, S.-I. (2013). *Seismic Anisotropy Due to Lattice Preferred Orientation of Minerals: Kinematic or Dynamic?*, pages 455–471. American Geophysical Union.

Karato, S.-I., Zhang, S., and Wenk, H.-R. (1995). Superplasticity in the earth's lower mantle: Evidence from seismic anisotropy and rock physics. *Science*, 270:458–461.

Katayama, I. and Karato, S.-I. (2006). Effect of temperature on the b- to c-type olivine fabric transition and implication for flow patterns in subduction zones. *Physics of the Earth and Planetary Interiors*, 157:33–45.

Kawakatsu, H. and Niu, F. (1994). Seismic evidence for a 920-km discontinuity in the mantle. *Nature*, 371:301–305.

Kawazoe, T., Ohuchi, T., Nishihara, Y., Nishiyama, N., Fujino, K., and Irifune, T. (2013). Seismic anisotropy in the mantle transition zone induced by shear deformation of wadsleyite. *Physics of the Earth and Planetary Interiors*, 216:91–98.

Lin, F.-C., Ritzwoller, M. H., Yang, Y., Moschetti, M., and Fouch, M. J. (2011). Complex and variable crustal and uppermost mantle seismic anisotropy in the western united states. *Nature Geoscience*, 4:55–61.

Liu, L.-g. (1974). Silicate perovskite from phase transformations of pyrope-garnet at high pressure and temperature. *Geophysical Research Letters*, 1(6):277–280.

Mainprice, D. (2015). Seismic anisotropy of the deep earth from a mineral and rock physics perspective. *Treatise on Geophysics*, 216:437–491.

McDonough, W. and Sun, S.-s. (1995). The composition of the earth. *Chemical Geology*, 120:223–253.

McNamara, A., van Keken, P., and Karato, S.-I. (2002). Development of anisotropic structure in the earth's lower mantle by solid-state convection. *Nature*, 416:310–314.

Merkel, S., McNamara, A., Kubo, A., Speziale, S., Miyagi, L., Duffy, T., and Wenk, H.-R. (2007). Deformation of (Mg,Fe)SiO_3 post-perovskite and D" anisotropy. *Science*, 316:1729–1732.

Merkel, S., Wenk, H.-R., Badro, J., Montagnac, G., Gillet, P., Mao, H.-k., and Hemley, R. (2003). Deformation of $(Mg_{0.9},Fe_{0.1})SiO_3$ perovskite aggregates up to 32GPa. *Earth and Planetary Science Letters*, 209:351–360.

Miyagi, L., Kanitpanyacharoen, W., Kaercher, P., Lee, K., and Wenk, H.-R. (2010). Slip systems in $MgSiO_3$ post-perovskite: Implications for D" anisotropy. *Science*, 329:1639–1641.

Miyagi, L. and Wenk, H.-R. (2016). Texture development and slip systems in bridgmanite and bridgmanite + ferropericlase aggregates. *Physics and Chemistry of Minerals*, 43:597–613.

Montagner, J. P. (1998). Where can seismic anisotropy be detected in the earth's mantle? in boundary layers... *Pure and Applied Geophysics*, 151:223–256.

Murakami, M., Hirose, K., Kawamura, K., Sata, N., and Ohishi, Y. (2004). Post-perovskite phase transition in $MgSiO_3$. *Science*, 304(5672):855–858.

Ohtani, E. and Sakai, T. (2008). Recent advances in the study of mantle phase transitions. *Physics of the Earth and Planetary Interiors*, 170(3):240 – 247. Frontiers and Grand Challenges in Mineral Physics of the Deep Mantle.

Panning, M. and Romanowicz, B. (2006). A three-dimensional radially anisotropic model of shear velocity in the whole mantle. *Geophysics Journal International*, 167:361–379.

Ringwood, A. (1962). Mineralogical constitution of the deep mantle. *Journal of Geophysical Research*, 67:4005–4010.

Romanowicz, B. and Wenk, H.-R. (2017). Anisotropy in the deep earth. *Physics of the Earth and Planetary Interiors*, 269:58–90.

Tschauner, O., Ma, C., Beckett, J., Prescher, C., Prakapenka, V., and Rossman, G. (2014). Discovery of bridgmanite, the most abundant mineral in earth, in a shocked meteorite. *Science*, 346(6213):1100–1102.

Tsujino, N., Nishihara, Y., Yamazaki, D., Seto, Y., Higo, Y., and Takahashi, E. (2016). Mantle dynamics inferred from the crystallographic preferred orientation of bridgmanite. *Nature*, 539:81–84.

Visser, K., Trampert, J., Lebdev, S., and B.L.N., K. (2008). Probability of radial anisotropy in the deep mantle. *Earth and Planetary Science Letters*, 270:241–250.

Wenk, H.-R., Cottaar, S., Tome, C., McNamara, A., and Romanowicz, B. (2011). Deformation in the lowermost mantle: from polycrystal plasticity to seismic anisotropy. *Earth and Planetary Science Letters*, 306:33–45.

Wenk, H.-R., Lonardelli, I., Merkel, S., Miyagi, L., Pehl, J., Speziale, S., and Tommaseo, C. (2006). Deformation textures produced in diamond anvil experiments, analyzed in radial diffraction geometry. *Journal of Physics: Condensed Matter*, 18:S933–S947.

Wenk, H.-R., Lonardelli, I., Pehl, J., Devine, J., Prakapenka, V., Shen, G., and Mao, H.-K. (2004). In situ observation of texture development in olivine, ringwoodite, magnesiowustite and silicate perovskite at high pressure. *Earth and Planetary Science Letters*, 226:507–519.

Wookey, J., Kendall, J. M., and Barruol, G. (2002). Mid-mantle deformation inferred from seismic anisotropy. *Nature*, 415:777–780.

Chapter 2

Finite Element Modeling with FEpX

Modeling plastic deformation in two-phase polycrystalline materials comprised of phases with pronounced strength contrast is of interest because of their abundance in the Earth and for specific engineering applications. Large strength contrast between phases and single crystal anisotropy is known to influence the development of stress and strain heterogeneity within grains. Texture development in these systems has a strong dependence on the orientation distribution, and the development of misorientation within each grain is dependent on their orientations and the strengths of grains within the local grain neighborhood. The classical Taylor theory and the more sophisticated self-consistent models are successful in modeling average properties, but do not accurately predict intragranular heterogeneity, and typically lead to more pronounced textures than those which are experimentally observed. In this study, the deformation response of a two-phase polycrystal with a mixture of orthorhombic bridgmanite ($MgSiO_3$) and cubic periclase (MgO) is simulated by means of a crystal plasticity finite element framework. This material is significant because it composes most of the Earths mantle and is important for understanding geodynamic processes. Special attention is drawn to the evolution of intragranular misorientation, and its dependence on the grain neighborhood and strength contrast between the phases. It is found that when the bridgmanite phase is 8 times harder than periclase, periclase carries almost 70% of the total plastic deformation of the aggregate, and intragranular misorientation is larger in periclase than in bridgmanite. Furthermore, interconnected soft grains exhibit larger deformation rates and intragranular misorientations than soft grains surrounded by predominantly hard grains. The opposite trend is witnessed when inspecting the hard bridgmanite phase. The development of this intragranular misorientation is responsible for the weak texture development that has been experimentally observed in the soft periclase phase when deformed in this two-phase aggregate with a large strength contrast.

2.1 Introduction

Plastic deformation of polycrystalline solids has been of interest for over half a century for both its relevance to fundamental questions, and the wide technological applications of these materials. There are many different plasticity theories that have been developed and implemented into numerical models over the years. Taylor (1938) and Sachs (1928) proposed models where equal strain (Taylor) and stress (Sachs) are assumed in all grains of a polycrystalline aggregate. These models are successful in capturing the average mechanical response in a polycrystal undergoing plastic deformation, and they provide an upper and lower bound to the average stress in the aggregate, respectively. The Taylor theory assumes that strain in the aggregate is achieved by slip in multiple directions, this analysis has been applied mainly to cubic polycrystalline metals (Kocks, 1958), and has successfully predicted cold deformation textures in these systems (Van Houtte and Aernoudt, 1976). Due to its fundamental assumptions, the Taylor model predicts a very rigid interaction in between grains, and it does not allow for local inhomogeneities in the shearing rates of different grains. In order to model grain interactions more realistically, one can apply a self consistent approach where each grain is treated as an inclusion in an effective medium that represents an average over all other grains. This formulation accounts for the interaction of grains with their neighborhood, and for plastic anisotropy in the matrix and in the grains (Molinari et al., 1987). This self consistent approach has been applied to successfully predict deformation textures in a wide variety of materials, capturing the effects of grain morphology and anisotropy in the polycrystal (Lebensohn and Tome, 1994). Most rocks and engineering materials are polyphase polycrystalline aggregates which challenge the Taylor and the self consistent approaches, large hardness contrasts in between the phases produces intricate heterogeneities at the inter and intra grain scale (Brechet and Dawson, 1996). Also, low symmetry of the constituent phases presents problems due to an open single crystal yield surface and high anisotropy. First attempts at modeling this type of low symmetry multi-phase materials were done by Canova et al. (1992), where they apply a self consistent approach to a virtual aggregate where grains are divided into cells that can deform differently.

Fully space resolved numerical calculations that solve crystal plasticity equations in a virtual 3D polycrystal provide quantitative information about the local sub-grain environment (Dawson et al., 1994). The results of these full-field crystal plasticity simulations can be used to explain the tendencies of texture development observed experimentally in two-phase aggregates (Raabe et al., 2002), without being hindered by simplifications in the model. A parallelized finite element approach to the problem is often used in this case because of its ability to capture deformation heterogeneities (e.g. Christman et al., 1989; Barbe et al., 2001), enabling the study of the influence of grain interactions in the distribution of the applied deformation (Mika and Dawson, 1998), subgrain misorientation as a function of the local grain environment (Barton and Dawson, 2001a), strain and lattice orientation distributions at a sub grain scale due to sample heterogeneities (Barton and Bernier, 2012), and more. Because of their capabilities, these models are perfectly suited for studying the influence

of the local grain environment in the evolution of texture in polyphase polycrystalline aggregates (Quey et al., 2015), in particular with large hardness contrast in between the different phases (Barton and Dawson, 2001b).

In Earth Science there is a wide variety of multi-phase systems who's plastic deformation is of interest for understanding the Earth's dynamic phenomena. The composition of the Earth's lower mantle is dominated by the minerals ferropericlase (Mg, Fe)O and bridgmanite (Mg,Fe)SiO_3 (Ringwood, 1962; McDonough and Sun, 1995; Irifune and Tsuchiya, 2015),which present contrasting rheology. Understanding plastic deformation in this mineral aggregate provides insight into the Earth's internal structure (Madi et al., 2005). Geodynamic considerations suggest large scale solid state convection in the Earth's interior with significant plastic deformation, giving rise to regions with elastic anisotropy that are revealed through seismological observations of the anisotropic propagation of seismic waves in these deformed structures (McNamara et al., 2002). Plasticity models have been applied to predict texture development in the upper mantle (e.g. Dawson and Wenk, 2000), the lower mantle (e.g. Wenk et al., 2006, 2011; Cottaar et al., 2014) and in the solid inner core composed of hcp iron (e.g. Buffett and Wenk, 2001). The models applied in these studies use simplifying assumptions that on one hand allow for swift numerical calculations, but on the other fail in capturing heterogeneities at the sub grain scale that can have important effects in the macroscopic properties of the aggregates. In this case a finite element approach is order.

Recent experiments and calculations have been done on the bridgmanite (Mg,Fe)SiO_3 + ferropericlase (Mg,Fe)O system deformed under compression up to 61GPa in a diamond anvil cell (DAC), observations show that when these phases are deformed as a mixture, the soft periclase phase develops little to no texture, contrary to when it is deformed as a single phase polycrystalline aggregate where it develops a considerable texture (Miyagi and Wenk, 2016). Mineral analogs to the bridgmanite + ferropericlase system have been studied and it is found that the soft phase controls deformation with volume fractions as low as 15%, weakening the texture of the hard bridgmanite analog phase (Kaercher et al., 2016).

In this work we demonstrate how the fully space resolved full-field finite element model implemented by the FEpX code can be used to study plastic deformation due to dislocation glide in the bridgmanite (Mg,Fe)SiO_3 and ferropericlase (Mg, Fe)O two-phase aggregate. With particular interest in texture and intragranular misorientation development, and the effect of phase strength contrast on these quantities.

2.2 Simulation Method

Simulation Parameters

A two-phase virtual polycrystal with 1000 grains, composed of orthorhombic bridgmanite ($MgSiO_3$) which is selected to be the hard phase and the soft periclase (MgO) phase that has cubic symmetry with a phase volume fraction of 75% and 25% respectively (Figure2.1a)

has been created using the software package Neper (Quey et al., 2011). The grain structure is generated with a highly regularized voronoi tessellation to avoid sharp artifacts in the microstructure, and the grains of phase 2 are selected randomly according to the 25% volume fraction. The initial orientations of the grains are chosen at random by the Neper software. Approximately 100 elements per grain is achieved by applying meshing algorithms to the voronoi tessellation, ensuring an appropriate resolution in the polycrystal to capture mechanical behavior at the crystal scale, a close up of the aggregate shows the elements in which the grains are subdivided (Figure2.1a). The aggregate has been deformed by compression in the sample Z direction up to 20% strain in increments of 0.1% strain, using the parallelized finite element based crystal plasticity code FEpX (Dawson and Boyce, 2015) (Figure2.1b). The aggregate is plastically deformed by dislocation glide exclusively; each phase has a set of slip systems, that are particular to their symmetry and atomic structure, through which dislocations migrate. Deformation rate of the slip systems is described as (Dawson and Boyce, 2015):

$$\begin{aligned} \hat{\mathbf{D}}^{P'} &= \sum_{\alpha} \dot{\gamma}^{\alpha} \hat{\mathbf{P}}^{\alpha} \\ \text{where } \hat{\mathbf{P}}^{\alpha} &= \text{sym}\left(\hat{\mathbf{s}}^{\alpha} \otimes \hat{\mathbf{m}}^{\alpha}\right) \end{aligned} \tag{2.1}$$

where $\dot{\gamma}^{\alpha}$ denotes the shearing rate on a slip system, α, and $\hat{\mathbf{P}}^{\alpha}$ is the symmetric portion of a slip system's Schmid tensor - constructed using a slip system's slip direction, $\hat{\mathbf{s}}^{\alpha}$, and a slip system's plane normal, $\hat{\mathbf{m}}^{\alpha}$. The shearing rate of a given slip system is defined using a power law expression to introduce rate dependence (controlled by m), and relates the shearing rate on a slip system to the resolved shear stress of a system, τ^{α} (Dawson and Boyce, 2015):

$$\begin{aligned} \dot{\gamma}^{\alpha} &= \dot{\gamma}_0 \left(\frac{|\tau^{\alpha}|}{g^{\alpha}}\right)^{\frac{1}{m}} \text{sgn}(\tau^{\alpha}) \\ \text{where } \tau^{\alpha} &= \text{tr}(\hat{\mathbf{P}}^{\alpha} \boldsymbol{\tau}') \end{aligned} \tag{2.2}$$

where the shearing rate on a slip system is scaled by the fixed-state strain rate scaling coefficient, $\dot{\gamma}_0$, and is dependent on a slip system's current strength, g^{α}. Rocks typically have a rate sensitivity, m in Equation 2.2, between 3 and 5 (Wenk and Christie, 1991), a rate sensitivity of 3 is selected because of its application to the lower mantle of the Earth. A small strain rate exponent like this effectively rounds the single crystal yield surface (SCYS) making the response of the aggregate more isotropic, and also aids in convergence of the code.

Each slip system's initial strength g_0^{α} is calculated multiplying the base strength for the material times the scalar that defines the relative strength of each slip system, this defines the slip systems critical resolved shear stress (CRSS) in the undeformed aggregate (Dawson and Boyce, 2015):

$$\dot{g}^{\alpha} = \dot{\gamma} h_0 \left(\frac{g_s^{\alpha}(\dot{\gamma}) - g^{\alpha}}{g_s^{\alpha}(\dot{\gamma}) - g_0^{\alpha}} \right)$$
$$\text{where } g_s^{\alpha}(\dot{\gamma}) = g_{s0}^{\alpha} \left(\frac{\dot{\gamma}}{\dot{\gamma}_{s0}} \right)^{m'} \text{ and } \dot{\gamma} = \sum_{\alpha} |\dot{\gamma}^{\alpha}| \tag{2.3}$$

Here, each slip system may evolve independently, and is controlled using the strength hardening rate coefficient, h_0, as well as each slip system's initial strength, g_0^{α}, and each slip system's saturation strength, g_s^{α}. These variables are selected by the user in the FEpX code. In this study, slip systems for each phase have been selected based on experimental observations and calculations done on these particular minerals and activities are calculated based on average slip system shear rates calculated using Equation 2.1 (Table2.1). In the orthorhombic phase, the experimentally observed and theoretically calculated slip systems do not close the single crystal yield surface, which presents problems for numerical convergence. An auxiliary $\{1\,1\,1\}$ $(0\,1\,1)$ cubic slip system has been added with a high CRSS value so it is not activated, this slip system closes the single crystal yield surface and aids in convergence of the code. A hardness contrast of 1:1 between phase 1 and phase 2 is presented as a reference for the case where we have one phase stronger than the other, here both phases are selected to have a base strength of 50 MPa. For the later case, phase 1 has been selected to have a initial strength of 450 MPa, which is 8 times stronger than the soft periclase phase 2 with 50 MPa, this large contrast is selected because of its relevance to the lower mantle (Madi et al., 2005). Also, single phase simulations were done to compare results with the two phase simulations to understand the effects of a second softer phase. Two single phase simulations are presented, one where the whole of the aggregate is composed of the bridgmanite phase with a base strength of 300 MPa and another where the whole of the aggregate is composed of periclase with a base strength of 50 MPa. All simulations are done with the same tessellation, meshing and phase distribution for direct comparison with each other.

Post-processing of the calculated results are done using MATLAB scripts developed in the Deformation Processes Laboratory of Cornell University and also others developed particularly for the needs of this study, see Appendix A for a list of postprocessing scripts. It is of interest to quantify the development of texture in the aggregate and to understand its connection to misorientation development at a subgrain level. For this purpose we use the software BEARTEX, in particular for its capabilities to calculate an orientation distribution function from discrete orientations and then to calculate and plot inverse pole figures of the compression direction, and also for its capability to plot pole figures of single orientations using the PTXX script embedded in BEARTEX (Wenk et al., 1998). PTXX is used to plot the starting orientation of selected grains in the aggregate, and track how the orientations of all the elements in the aggregate rotate and how misorientation within a single grain evolves as the polycrystal deforms.

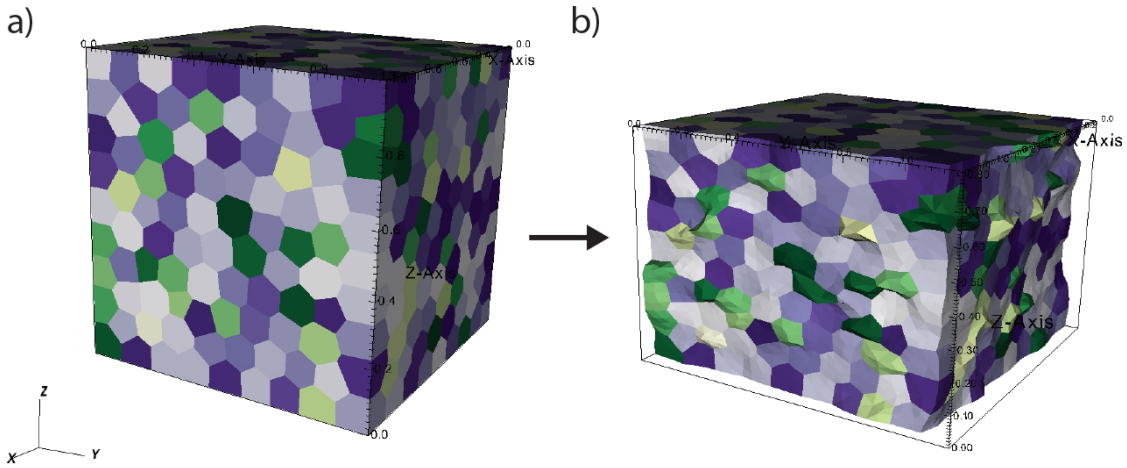

Figure 2.1: *Virtual aggregate instantiated by the software Neper. Color coding is by grain number, purple color map corresponds to phase 1 and yellow to green color map corresponds to phase 2. A) shows aggregate before deformation. Bottom right corner shows the mesh that is used for the finite element calculation. B) is the deformed aggregate at 20% strain for the 8:1 hardness contrast case.*

2.3 Results

Results of finite element simulations of a two phase polycrystalline aggregate composed of bridgmanite + periclase, and single phase simulations using the FEpX code are presented in this section. First, general trends in the plastic deformation rate distributions are considered, with particular interest in differences between the response of the hard and soft phase, and to how these compare when the same aggregate is deformed with a single phase of bridgmanite or periclase (Figure 2.2). Inverse pole figures are plotted and enable us to understand the effect of the large strength contrast imposed between the phases on the relative texture strength and components in the different simulations (Figure 2.4). Average slip system activity over the whole aggregate is calculated with the objective of comparing the slip system activity between the phases, and understanding the influence of strength contrast in this quantity. It is also of interest to connect the observed slip system activity trends with the bulk texture (Table 2.1). In order to understand the effect of these simulation conditions in the development of intragranular misorientation, the misorientation of each element within the grain is calculated with respect to the average grain orientation and results are compared between the different simulations. It is of interest to understand the effects of the local grain environment in the development of intragranular misorientation, for this purpose a total of four grains are selected for further analysis (Figure 2.5). Selected grains are in the interior of the aggregate to eliminate possible surface effects and are chosen on the basis of their neighborhood, for each phase there is one grain that is interconnected with grains of the

same phase, referred to as interconnected grains, and another that is mainly surrounded by grains of the other phase, these are referred to as isolated grains. Pole figures with the orientation of the poles of the (0 0 1) plane for orthorhombic symmetry and the poles to the {1 0 0} family of planes in the case of the cubic symmetry are plotted in the sample coordinate frame for each element of the selected grains to visually compare the behavior of the different grains as deformation evolves (Figure 2.6).

Plastic deformation rates at 20% strain are plotted for the 1:1 hardness ratio, the 8:1 ratio and the single phase bridgmanite and single phase periclase simulations in Figure 2.2. A 2D slice perpendicular to the y-axis and through the center of the aggregate is shown point out heterogeneities in the plastic deformation rate of the deformed sample. For all four simulations, the grain structure at 20% strain is shown in the top row, second row plots plastic deformation rates of phase 1 with the grains of phase two colored for reference, and in the case of the single phase simulations the plastic deformation rate of all the grains in the slice are shown. The third row shows plastic deformation rate of the periclase phase with the grains of the bridgmanite phase colored for reference. Although deformation bands do appear in the 1:1 case, there is very little contrast in between the two phases in terms of the magnitude of the plastic deformation rate (Figure 2.2a). As the strength contrast between the phases is increased to an 8:1 ratio (Figure 2.2b), deformation bands appear in the same regions as the more isotropic case, but there is a large contrast in between the deformation rates of the two phases, in this case phase 2 presents higher deformation rates than phase 1, as can be seen by comparing row 2 with row 3 in Figure 2.2b.

Histograms of the plastic deformation rate at 20% strain were calculated and are shown in Figure 2.3, bins were selected to be 0.0001 wide for all four plots. A first thing to notice in the distribution of plastic deformation rate values is that for all four simulations the distributions are asymmetrical, with a positive skewness that is calculated as the Pearson's moment coefficient of skewness. The run with lowest skewness is that in Figure 2.3a, with a skewness of 0.42, in this case we have two phases but they are both the same hardness, even though they are both equally stiff there is a difference in the symmetry of the phases which provides different deformation conditions for the grains of different phases. In Figure 2.3b a histogram of the plastic deformation rate of the two phase case where the orthorhombic bridgmanite phase is 8 times harder than the cubic periclase phase is shown, this is the case with the widest and most asymmetric distribution of values of the plastic deformation rate with a skewness of 2.58. The single phase simulations serve as an important reference for the two phase cases. Results are shown for the single phase orthorhombic bridgmanite phase in Figure 2.3c. This single phase case has a higher skewness of 0.54, with respect to the two phase case with phases of equal strength, which suggest that the low content of the cubic phase facilitates plastic deformation. The single phase run with the cubic periclase phase has a skewness of 0.50, which indicates that in this case there is also stronger heterogeneity than in the two phase case with 1:1 hardness ratio. As for measures of central tendency we have chosen to calculate the mode of the raw plastic deformation rate results since it represents the most frequent value of the plastic deformation rate for each run. The mode

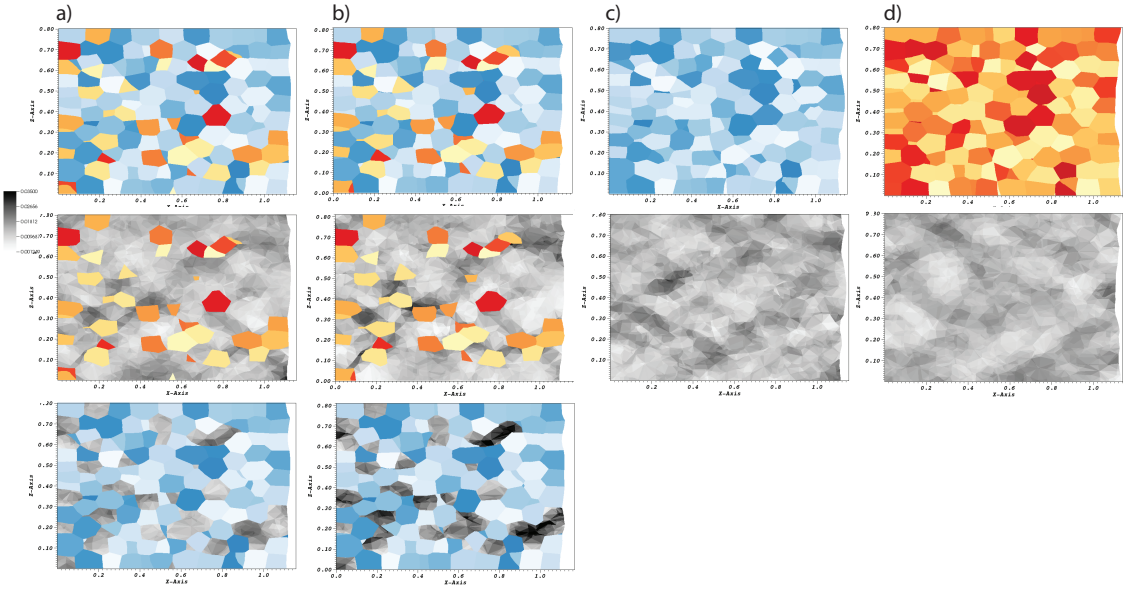

Figure 2.2: *Plastic deformation rate ZX slices for a) 1:1 strength contrast b) 8:1 strength contrast at 20% strain, c) single phase bridgmanite run and d) single phase periclase run. Top row shows grains at deformed state, purple color map corresponds to phase 1 and yellow to green color map corresponds to phase 2. Second row shows plastic deformation rate in grey scale and grains for the cubic periclase phase 2 are colored for reference in the two phase cases. Third row show plastic deformation rate of periclase phase 2, grains of phase 1 are colored for reference in the two phase simulations. Deformation bands appear in both two phase cases in the same locations but with different contrast in between the two phases, the large strength contrast in b) promotes larger heterogeneities in the plastic deformation rate of both phases.*

in Figure 2.3a is 0.011, while for the 8:1 case in Figure 2.3b is considerably higher at 0.015. As for the single phase runs, the mode is the same in both runs, with a value of 0.013.

Bulk texture sees about a 10% decrease in the case with large strength contrast with respect to the 1:1 calculations (Figure 2.4). Figure 2.4 shows inverse pole figures of the compression direction for the orthorhombic bridgmanite phase (top row) and the cubic periclase phase (bottom row), for both the 1:1 case (Figure 2.4a) and the 8:1 case (Figure 2.4b). For the orthorhombic phase, the maximum of the orientation distribution function reaches 2.24 multiples of random distribution (m.r.d.) in the 1:1 case and it is reduced to 2.03 m.r.d. when we have a large strength contrast (Figure 2.4b). The overall texture in the 8:1 case shown in Figure 2.4b has a larger spread than the 1:1 case (Figure 2.4a) but has the same shape. Compared to the single phase orthorhombic simulation in Figure 2.4c, the texture maximum of the 8:1 simulation is practically the same value, with a difference in shape due to slight changes in relative slip system activity calculated in Table 2.1. The cubic

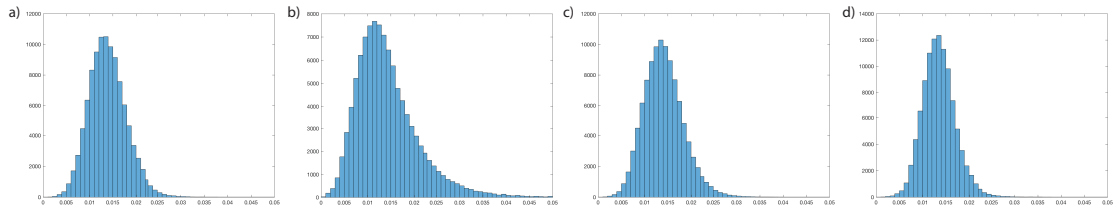

Figure 2.3: *Histograms of the plastic deformation rate at 20% strain for all four simulations. a) Two phase simulation where phases have same hardness (1:1 case). b) Two phase simulation where orthorhombic bridgmanite phase is 8 times harder than the cubic periclase phase. c) Single phase run where whole aggregate is composed of the orthorhombic bridgmanite phase. d) Single phase run with cubic periclase phase.*

periclase phase has significant changes in the resulting texture components for the different simulations. In the 1:1 case there is a defined maximum for the poles of the $\{1\,1\,0\}$ family of planes, whereas in the 8:1 case the texture starts spreading towards the $\{1\,0\,0\}$ and develops a small maximum for the poles of this family. When the aggregate is deformed as a single periclase phase aggregate the texture spreads between the poles of the $\{0\,1\,1\}$ and $\{1\,0\,0\}$ planes. Texture strength is also reduced in the cubic periclase phase, from a maximum of 1.73 m.r.d. for the 1:1 case to 1.57 m.r.d. for the 8:1 case, the single phase simulation has a similar texture to the 8:1 case with a maximum of 1.61 m.r.d.

Slip system activity is calculated based on the shearing rates of each system as is calculated in Equation 2.2. For each deformation step, an average slip system activity for each slip system is calculated by averaging the shearing rate of the slip system, $\dot{\gamma}^{\alpha}$ in Equation 2.2, over all the elements of the phase it belongs to. In order to compare average activity between phase 1 and 2, the averaged activities for each slip system of each phase are normalized to the total average activity of the aggregate (Table 2.1). In the orthorhombic bridgmanite phase, activity in the $(0\,0\,1)$ plane and the different possible directions shown in Table 2.1 is selected to be the easiest with a relative CRSS value of 1. In both two phase simulations the most active slip system is the $(0\,0\,1)\langle 1\,1\,0\rangle$ with 10% activity in the 1:1 hardness contrast case, 8% in the 8:1 case, as well as in the single phase orthorhombic run with an activity of 22%. The second most active in these three cases is the $(1\,0\,0)[0\,1\,0]$ with 5, 4 and 12% activity for the 1:1, 8:1 and single phase orthorhombic simulations respectively. It is important to note that in the case of the two phase simulations the percentage of activity must add to 100% when the sum of activities from all slip systems corresponding to both phases is considered. It is most important to compare the total slip activity (sum of relative activities) of phase 1 with that of phase 2, and to see how this comparison changes as the hardness contrast is increased between bridgmanite and periclase. In the simulation where bridgmanite and periclase have the same hardness (i.e. the 1:1 simulation) the activity is evenly distributed between the two phases, indicating that both the orthorhombic and cubic phases have close to the same slip system activity, with phase 1 carrying 44% of the activity

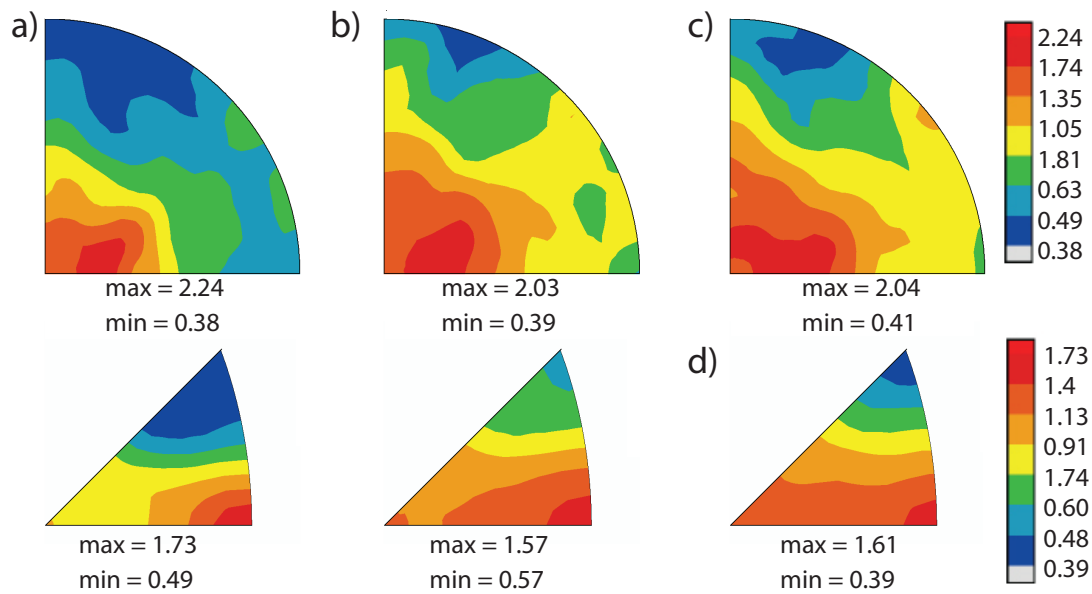

Figure 2.4: *Inverse pole figures of the compression direction for the orthorhombic phase (top row) and for the cubic phase (bottom row). a) Inverse pole figures after 20% strain for the 1:1 strength contrast case. b) Inverse pole figures after 20% strain for the 8:1 strength contrast case. A reduction of 10% in the texture strength from case 1:1 to case 8:1 is seen for both phases. c) Single phase perovskite calculated inverse pole figure after 20% strain. d) Single phase periclase run. Inverse pole figures are calculated using the software BEARTEX, and orientation output exported using a script shown in Appendix A.*

and phase 2 carrying 54% of the activity. This can be seen in the last two columns of Table 2.1 where the sum of activity of phase 1 and 2 are presented. As the hardness contrast is increased to the 8:1 case where the orthorhombic bridgmanite phase 1 is 8 times stronger than the cubic periclase, the activity of the soft periclase phase goes up to a 67% and the activity of the hard orthorhombic phase lowers to a 33%, indicating that in this case the soft periclase is absorbing most of the plastic deformation of the whole aggregate.

Intragranular misorientation was quantified by calculating misorientation between the average orientation of each grain with the orientation of each element it contains. The average orientation is obtained by averaging the weighed orientations (by volume) of all the elements that belong to the grain and averaging over the norm of the sum of weighed orientations, and the misorientation is calculated in quaternion space by finding the linear transformation that takes the grain average orientation to the orientation of the particular element in the grain and taken to the fundamental region of the particular symmetry in question to account for symmetry equivalent orientations, these orientation quaternions are then converted to angular values for analysis, the script used to perform these calculations is shown in Appendix A. It is found that a log normal distribution fits the distribution of

	Bridgmanite								Periclase				
n	(1 0 0)	(1 0 0)	(0 1 0)	(0 1 0)	(0 0 1)	(0 0 1)	(0 0 1)	{1 1 1}	{1 1 1}	{1 1 0}	{1 0 0}		
b	[0 1 0]	⟨0 1 1⟩	[1 0 0]	⟨1 0 1⟩	[1 0 0]	[0 1 0]	⟨1 1 0⟩	⟨0 1 $\bar{1}$⟩	⟨0 1 $\bar{1}$⟩	⟨1 $\bar{1}$ 0⟩	⟨0 1 1⟩		
CRSS Multiplier	2	2	3	3	1	1	1	5	2	1	5		
Slip Activity	Bridgmanite								Periclase			SumPh1	SumPh2w
1:1	0.05	0.02	0.02	0.01	0.01	0.00	0.10	0.23	0.39	0.12	0.05	0.44	0.54
8:1	0.04	0.02	0.01	0.01	0.00	0.00	0.08	0.17	0.50	0.11	0.06	0.33	0.67
Ortho	0.12	0.05	0.04	0.03	0.01	0.01	0.22	0.51				1.00	
Cubic									0.43	0.56	0.01		1.00

Table 2.1: *Selected slip systems for the orthorhombic bridgmanite and cubic periclase phases shown in top rows. Slip system activity after 20% strain for the 1:1, 8:1 and single phase orthorhombic and cubic simulations. Activity is calculated as an average of the shear rates of individual slip systems over the whole aggregate, once averaged they are normalized to capture the relative activity. Slip systems are calculated using a postprocessing script presented in Appendix A.*

misorientation values for all elements and the four different simulations, statistical quantities of the fitted distributions are shown in Table 2.2. For the two phase simulations, the grains from each phase are considered separately and misorientation of each element with respect to the grain average is calculated. For the case where the orthorhombic bridgmanite phase has the same hardness of the cubic periclase it is found that the mean of the misorientation is similar for both phases, 4.42 and 4.98 degrees for phase 1 and phase 2 respectively (Table 2.2). The periclase phase 2, however, shows a larger variance of 10.63 degrees compared to 8.5 degrees for phase 1, suggesting that the periclase phase presents more heterogeneous deformation conditions than the orthorhombic bridgmanite although on average grains from both phases present equivalent conditions as shown by the mode and similar skewness as well. It is important to point out that even though the hardness of the two different phases is the same, the orthorhombic phase presents more anisotropy due to the limited directions in which dislocations can migrate in, making it harder for bridgmanite phase to deform. As the difference in materials properties is increased, and set to more realistic parameters, it is observed that in the 8:1 case there is large difference in the misorientation distribution of the two phases. As can be seen in Table 2.2, the mean misorientation for the orthorhombic phase is a slightly higher than in the 1:1 case at 4.91 degrees but with a considerably larger variance of 12.88 degrees and a more skewed distribution. Furthermore, the cubic phase 2 presents a 76% increase with respect to phase 1 for this 8:1 simulation, with a value of 8.68 degrees, and very large variance of 35.58 degrees, suggesting very heterogeneous deformation conditions for this phase. Single phase simulations present very interesting results. In particular, the bridgmanite single phase simulation has a mean misorientation of 5.03 degrees and a variance of 11.28 degrees which are larger values than when this phase is deformed with 25% periclase by volume when the two phases have the same hardness (i.e. 1:1 simulation). This suggests that the presence of the cubic phase promotes a less heterogenous deformation in bridgmanite than when deformed as a single phase. Finally, the single phase cubic simulation presents

Misorientation lognormal distribution parameters

Simulation	Phase	Mean	Variance	Skewness
Two phase 1:1	Ortho	4.42	8.5	6.99
	Cubic	4.98	10.63	6.91
Two phase 8:1	Ortho	4.91	12.88	8.29
	Cubic	8.68	35.58	7.47
Single phase	Ortho	5.03	11.28	7.13
Single phase	Cubic	3.66	5.59	6.76

Table 2.2: *Misorientation distribution parameters calculated from fit with a lognormal distribution to misorientation of each element with respect to the grain average orientation. Values are expressed in degrees.*

the lowest misorientation mean of 3.66 degrees, and also the smallest variance of 5.59 degrees out of the four simulations presented in this study. The lower anisotropy introduced by the cubic symmetry promotes a less heterogeneous deformation in the aggregate, indicating that anisotropy introduced by symmetry is a key factor in the development of high intragranular misorientation.

A cluster of grains is selected in the center of the aggregate to remove possible surface or edge effects in our analysis (Figure 2.5). From this cluster a subset of 4 grains have been selected, two of which belong to the orthorhombic bridgmanite phase and two of the cubic periclase phase. In both cases a grain that is mostly interconnected with grains of its own phase and one that is isolated, mostly surrounded by grains of the other phase, were selected with the objective of finding any possible differences these two types of grains might have. Figure 2.6 shows pole figures that plot the starting orientation of all elements in the 4 selected grains as a red cross, and then the orientation of all elements of the grains at 20% strain in black crosses. For the orthorhombic phase (0 0 1) pole figures are plotted and {1 0 0} pole figures are plotted for the cubic phase. In general, in the two phase simulations it is seen that there is less spread of the intragranular orientations in the case where there is no strength contrast (Figure 2.6a), with respect to the 8:1 strength contrast case (Figure 2.6b) where a larger spread in the final intragranular orientations is observed, especially in the soft cubic phase. Grain 917, a grain of the orthorhombic phase 1, is an isolated grain that is mostly surrounded by grains of phase 2, while grain 860 of the same phase is an interconnected grain, that is mostly surrounded by grains of its own phase. It is noted that grain 917 develops a strong bifurcation as the hardness contrast increases and the orientation spread of grain 860 does not change considerably from the 1:1 to the 8:1 simulation. For phase 2, grain 735 is an isolated grain and presents considerably less intragranular misorientation than grain 793 of the soft phase that is an interconnected grain. Single phase runs show a very small spread in intragranular misorientation compared to the two phase runs. Pole figures for the orthorhombic bridgmanite single phase run (Figure 2.6c) show that for grain 917 the

orientation tends to one of the directions of the bifurcated grain the 8:1 case (Figure 2.6b). The single cubic periclase phase run shows a considerable difference in the development of misorientation if grain 735 and 793 is compared with the two phase 8:1 case in Figure 2.6b.

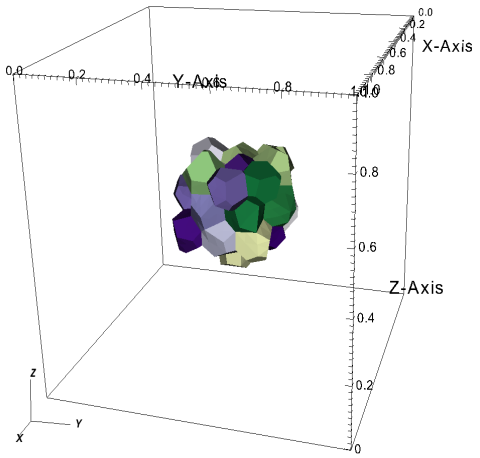

Figure 2.5: *Selected region in center of aggregate. 4 grains (2 of each phase) were selected from this region for further analysis. Purple color map corresponds to phase 1 and yellow to green color map corresponds to phase 2.*

2.4 Discussion

The dependence of bulk texture development on intragranular misorientation, deformation heterogeneities and slip system activity in a 75% bridgmanite 25% periclase aggregate deformed by slip is considered in this section. It is show in Table 2.2 that the largest intragranular misorientation is obtained in the simulation where the orthorhombic bridgmanite phase is 8 times harder than the cubic periclase phase. In particular it is this cubic phase 2 that develops the largest misorientation of the two phases which explains the weakening of the texture from 1.73 m.r.d. in Figure 2.4a to 1.57 m.r.d. in the inverse pole figures of the periclase phase shown in Figure 2.4b. The development of this large intragranular misorientation can explain the weak texture observed in this periclase phase in diamond anvil cell experiments (DAC) where the bridgmanite and periclase mixture is synthesized from the mineral olivine and the mineral ringwoodite in the DAC and diffraction images in the radial DAC geometry are taken to measure texture development in the polycrystalline samples (Miyagi and Wenk, 2016). Large volume press experiments on an analog system to bridgmanite + periclase mixture composed of the minerals neighborite and halite also find weak texture in the cubic halite phase, and an overall reduction in the texture as well (Kaercher et al., 2016). These tendencies are in agreement with a recent experimental study

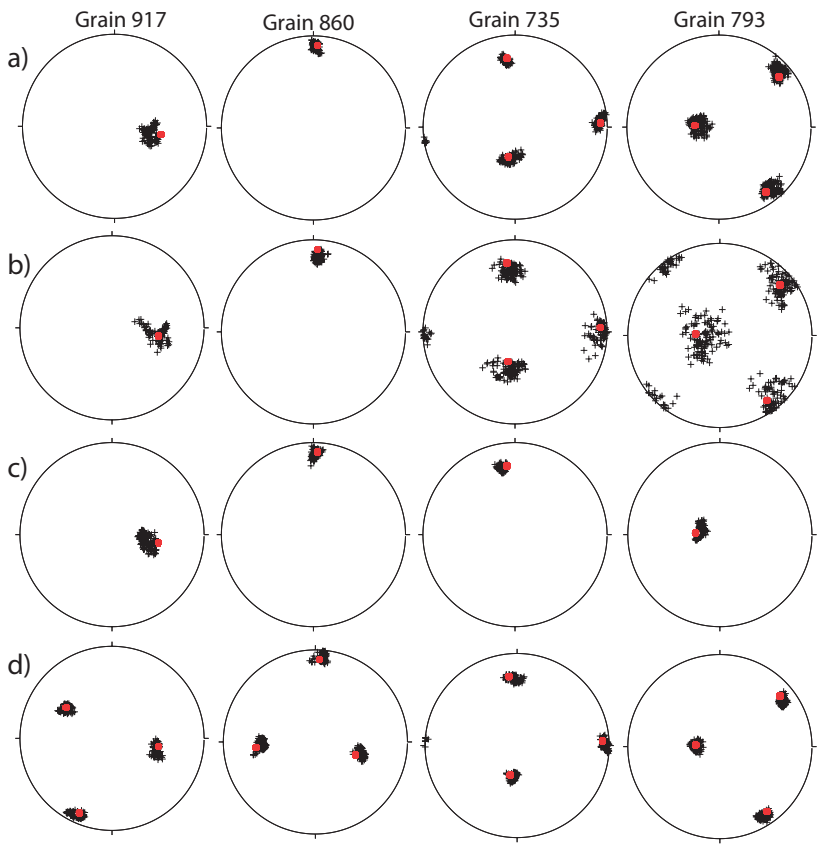

Figure 2.6: *Pole figures of the orientation of all elements in selected grains. Red cross is initial orientation of the grain and black crosses are the orientation of all the elements of the grain after 20% strain. a) Two phase run with 1:1 strength contrast. b) Two phase run with 8:1 contrast. c) Single phase orthorhombic bridgmanite run. d) Single phase cubic periclase run. Orientations for all the elements of a grain are selected using a script shown in Appendix A, and pole figures plotted using PTXX.*

on the bridgmanite + periclase mixture where sophisticated diamond anvil cell experiments were done and it was found that the periclase phase accommodates most of the strain during deformation up to approximately 100% strain (Girard et al., 2016).

Slip system activity show that the soft periclase phase largely responds to changes in microstructure and mechanical properties of the aggregate. The relative activity between the most active orthorhombic slip systems $(0\,0\,1)\langle 1\,1\,0\rangle$ and $(1\,0\,0)[0\,1\,0]$ remains practically constant across the different simulations, where the first is two times more active than the latter (Table 2.1). In contrast with this stable behavior, the periclase phase changes considerably its activity across the different simulations, which results in large changes of the maxima shapes in inverse pole figures of the compression direction (Figure 2.4). Furthermore, while slip system activity in the 1:1 two phase simulation is equally distributed in the two

phases, with an activity of 44% in bridgmanite and 54% in periclase, the soft periclase phase is responsible for 67% of the slip system activity and the hard bridgmanite phase a 33% in the 8:1 two phase simulations.

Histograms of the plastic deformation rate show interesting tendencies in how this quantity is distributed in the aggregate. The simulation with the lowest most frequent value of the plastic deformation rate and with the smallest skewness is the 1:1 strength contrast simulation (Figure 2.3a) and the simulation with the highest mode and largest skewness is the when there is a large strength contrast between the phases (Figure 2.3b). The single phase simulations have very similar values of mode and skewness with respect to each other, and they lie in between the values for the 1:1 and 8:1 runs. The fact that the 1:1 two phase simulation is the run with the lowest central value and smallest skewness suggests that the introduction of the 25% volume of the soft periclase phase aids in accommodating strain and smoothes some of the heterogeneities introduced by a large hardness contrast between two phases or just the local grain environment in the single phase cases. This is in agreement with what is shown in Table 2.2 where the mean of the misorientation distribution of phase 1 in the 1:1 two phase simulation is 4.42 degrees, which is a lower value than when the orthorhombic phase 1 is deformed as a single phase with a mean of 5.03 degrees of misorientation of the elements of the grain with respect to its average orientation, and also a lower variance of 8.5 degrees in the 1:1 case than the variance in the single phase orthorhombic run of 11.28 degrees. The cubic periclase phase presents the opposite trend, where the single phase run presents a lower mean and variance than the two phase 1:1 simulation. This points toward a strong dependence of intragranular misorientation on anisotropy introduced by symmetry.

Pole figures plotting the poles of all the elements of 4 selected grains provide insight into differences in how intragranular orientation spreads with different deformation conditions (Figure 2.6). It is observed that while the two selected grains of the soft periclase phase develop a larger orientation spread of the $\{1\,0\,0\}$ poles, it is grain number 793 that presents a larger difference between the 1:1 case in Figure 2.6a and the 8:1 case in Figure 2.6b. Grain 793 of the soft cubic periclase phase is a grain that is mostly surrounded by grains of the same phase, providing an environment that facilitates deformation. This can also be observed in plastic deformation plots, in particular in Figure 2.2b column three, where in the bottom and top right corners there are two sections of interconnected grains of the soft periclase phase where high values of the plastic deformation rate are concentrated in the interior of the grain cluster. Pole figures of the single phase run in 2.6d confirm that very little intragranular misorientation develops in this single phase case, like shown in Table 2.2 where this run presents the lowest misorientation mean and variance. If the orientation spread of grains 917 and 860 are compared in Figure 2.6 it is found that in the two phase simulations shown in Figure 2.6a and b, a bifurcation in the grain develops that is stronger in the 8:1 case. Compared to the single phase simulation shown in Figure 2.6c, it appears as the grain selected one of the directions of the bifurcation, indicating that the heterogeneities introduced by the second phase might make certain grain orientations more susceptible to bifurcation.

2.5 Conclusions

A study was performed on a two phase polycrystalline mineral aggregate with 75% bridgmanite ($MgSiO_3$) and 25% periclase (MgO) deformed under compression up to 19% strain by finite element simulations, these phases have orthorhombic and cubic symmetry respectively, and the location of the cubic periclase phase grains is selected randomly. Plastic deformation is considered to be due to dislocation glide exclusively, and no grain boundary sliding is modeled. Specifically, the influence of elastic anisotropy due to symmetry and particular material properties, and phase hardness contrast on the development of intragranular misorientation and bulk texture development is explored. Slip system activity is analyzed to understand the effect of both hardness contrast and elastic anisotropy on bulk texture development. Statistical trends of misorientation of individual elements with respect to average grain orientation at 19% strain are considered. Pole figures of the collection of poles of all the elements that compose 4 selected grains are plotted. The grains are selected on a neighborhood basis, by manually selecting one interconnected grain and one isolated grain (with respect to its own phase), special care must be taken in the analysis of these plots since the initial orientation of the grains with respect to the loading axis is not taken into account. Plastic deformation rates are plotted for the different simulations and 2D slices of the aggregate are shown. Plastic deformation rates shows structures with a scale larger than the grain size, and trends can be seen in terms of differences between deformation rates of the orthorhombic versus the cubic phase. Single phase simulations are also carried out for comparison with the two phase simulations, both the orthorhombic bridgmanite phase and the cubic periclase phase are deformed in the same conditions and with the same microstructure as their two phase counterparts. It is found that when the hardness contrast is increased between the phases, the majority of the plastic deformation occurs in the softer cubic phase as is seen by an increase in slip system activity, the mean intragranular misorientation of this phase also increases and it presents a wider and more asymmetric distribution of this value and these values are larger than for the orthorhombic phase. As a result of this larger misorientation the texture in the cubic periclase phase is reduced as the hardness contrast increases. If the periclase phase is deformed as a single phase the misorientation mean over the whole aggregate is the lowest. The orthorhombic phase presents a different behavior than the cubic phase. The mean misorientation does not increase as dramatically when the strength contrast is amplified and it presents a lower mean misorientation value than when deformed as a single phase. Although the findings presented in this study shed light into the mechanical response of this lower mantle mineral assemblage, deformation conditions in the lower mantle are most likely more complex. FEpX assumes dislocation glide as a sole deformation mechanism which may not apply to the lower mantle, where other mechanisms such as climb, grain boundary sliding and recrystallization might be relevant.

References

Barbe, F., Decker, L., Jeulin, D., and Cailletaud, G. (2001). Intergranular and intragranular behavior of polycrystalline aggregates. part 1: F.e. model. *International Journal of Plasticity*, 17:513–536.

Barton, N. R. and Bernier, J. (2012). A method for intragranular orientation and lattice strain distribution determination. *Journal of Applied Crystallography*, 45:1145–1155.

Barton, N. R. and Dawson, P. R. (2001a). A methodology for determining average lattice orientation and its application to the characterization of grain substructure. *Metallurgical and Materials Transactions A*, 32:1967–1975.

Barton, N. R. and Dawson, P. R. (2001b). On the spatial arrangement of lattice orientations in hot-rolled multiphase titanium. *Modeling Simulation in Materials Science and Engineering*, 9:433–463.

Brechet, Y. and Dawson, P. (1996). Effects of interactions among crystals on the inhomogeneous deformations of polycrystals. *Acta Materialia*, 44:1937–1953.

Buffett, B. and Wenk, H.-R. (2001). Texturing of the inner core by maxwell stresses. *Nature*, 413:60–63.

Canova, G., Wenk, H.-R., and Molinari, A. (1992). Deformation modeling of multi-phase polycrystals: Case of a quartz-mica aggregate. *Acta Metallurgica et Materialia*, 40:1519–1530.

Christman, T., Needleman, A., and Suresh, S. (1989). An experimental and numerical study of deformation in metal-ceramic composites. *Acta Metallurgica*, 37:3029–3050.

Cottaar, S., Li, M., McNamara, A., Romanowicz, B., and Wenk, H.-R. (2014). Synthetic seismic anisotropy models within a slab impinging on the core-mantle boundary. *Geophysical Journal International*, 199:164–177.

Dawson, P. and Boyce, D. (2015). Fepx - finite element polycrystals: Theory, finite element formulation, numerical implementation and illustrative examples.

Dawson, P., Needleman, A., and Suresh, S. (1994). Issues in the finite element modeling of polyphase plasticity. *Materials Science and Engineering A*, 175:43–48.

Dawson, P. and Wenk, H.-R. (2000). Texturing of the upper mantle during convection. *Philosophical Magazine A*, 80:573–598.

Girard, J., Amulele, G., Farla, R., Mohiuddin, A., and Karato, S.-i. (2016). Shear deformation of bridgmanite and magnesiowustite aggregates at lower mantle conditions. *Science*, 351:144–147.

Irifune, T. and Tsuchiya, T. (2015). 2.03 - phase transitions and mineralogy of the lower mantle. In Schubert, G., editor, *Treatise on Geophysics (Second Edition)*, pages 33 – 60. Elsevier, Oxford, second edition edition.

Kaercher, P., Miyagi, L., Kanitpanyacharoen, W., Zepeda-Alarcon, E., Wang, Y., Parkinson, D., Lebensohn, R., De Carlo, F., and Wenk, H.-R. (2016). Two phase deformation of lower mantle mineral analogs. *Earth and Planetary Science Letters*, 456:134–145.

Kocks, U. (1958). Polyslip in polycrystals. *Acta Metallurgica*, 6:294.

Lebensohn, R. and Tome, C. (1994). A self-consistent viscoplastic model: prediction of rolling textures of anisotropic polycrystals. *Materials Science and Engineering A*, 175:71–82.

Madi, K., Forest, S., Cordier, P., and Boussuge, M. (2005). Numerical study of creep in two-phase aggregates with a large rheology contrast: Implications for the lower mantle. *Earth and Planetary Science Letters*, 237:223–238.

McDonough, W. and Sun, S.-s. (1995). The composition of the earth. *Chemical Geology*, 120:223–253.

McNamara, A., van Keken, P., and Karato, S.-I. (2002). Development of anisotropic structure in the earth's lower mantle by solid-state convection. *Nature*, 416:310–314.

Mika, D. P. and Dawson, P. R. (1998). Effects of grain interaction on deformation in polycrystals. *Materials Science and Engineering A*, 257:62–76.

Miyagi, L. and Wenk, H.-R. (2016). Texture development and slip systems in bridgmanite and bridgmanite + ferropericlase aggregates. *Physics and Chemistry of Minerals*, 43:597–613.

Molinari, A., Canova, G., and Ahzi, S. (1987). A self consistent approach of the large deformation polycrystal viscoplasticity. *Acta Metallurgica*, 35:2983–2994.

Quey, R., Dawson, P., and Barbe, F. (2011). Large-scale 3d random polycrystal for the finite element method: Generation, meshing and remeshing. *Comput. Methods Appl. Mech. Engrg.*, 200:1729–1745.

Quey, R., Driver, J., and Dawson, P. (2015). Intra-grain orientation distributions in hot-deformed aluminium: Orientation dependence and relation to deformation mechanisms. *Journal of the Mechanics and Physics of Solids*, 84:506–527.

Raabe, D., Zhao, Z., and Mao, W. (2002). On the dependence of in-grain subdivision and deformation texture of aluminum on grain interaction. *Acta Materialia*, 50:4379–4393.

Ringwood, A. (1962). Mineralogical constitution of the deep mantle. *Journal of Geophysical Research*, 67:4005–4010.

Sachs, G. (1928). Zur Ableitung einer fliessbedingung. *Z. Verein Deut. Ing.*, 72:734–736.

Taylor, G. (1938). Plastic strain in metals. *Journal of the Institute of Metals*, 62:307.

Van Houtte, P. and Aernoudt, E. (1976). Considerations on the crystal and the strain symmetry in the calculation of deformation textures with the taylor theory. *Materials Science and Engineering*, 23:11–22.

Wenk, H.-R. and Christie, J. (1991). Comments of the interpretation of deformation textures in rocks. *Journal of Structural Geology*, 13:1091–1110.

Wenk, H.-R., Cottaar, S., Tome, C., McNamara, A., and Romanowicz, B. (2011). Deformation in the lowermost mantle: from polycrystal plasticity to seismic anisotropy. *Earth and Planetary Science Letters*, 306:33–45.

Wenk, H.-R., Matthies, S., Donovan, J., and Chateigner, D. (1998). Beartex: a windows-based program system for quantitative texture analysis. *Journal of Applied Crystallography*, 31:262–269.

Wenk, H.-R., Speziale, S., McNamara, A., and Garnero, E. (2006). Modeling lower mantle anisotropy development in a subducting slab. *Earth and Planetary Science Letters*, 245:302–314.

Chapter 3

Polycrystal Plasticity with the VPFFT Code

3.1 Introduction

Understanding plastic deformation of heterogenous polycrystalline materials has been a long withstanding problem (e.g. Brechet and Dawson, 1996; Tullis and Wenk, 1994). With the advancement of experimental characterization techniques that provide information on materials properties from bulk average properties Wenk et al. (2006) to local grain scale properties (Vigano et al., 2016), it is of interest to develop models that allow the introduction of the complex structures observed in experiments, and to determine the local states in these systems. The finite element method (FEM) (e.g. Dawson et al., 1994) as well as 1-site and multisite homogenization models (e.g. Lebensohn and Tome, 1994) have been used to model the local behavior of plastically deformed polycrystals with complex microstructures (e.g. Canova et al., 1992). FEM based codes have been applied to computer generated polyphase polycrystalline aggregates to capture intra-grain orientation distributions (Quey et al., 2015), to understand the influence of grain morphology on yield strength and ductility (Kasemer et al., 2017), and to study the effect of phase hardness contrast in grain and sub-grain deformation heterogeneities and subsequent lattice orientation variations (Barton and Dawson, 2001). However, the complexity of the microstructures that are accessible to FEM based modeling, with respect to experimentally observed microstructures (e.g. Girard et al., 2016), are limited due to the current meshing capabilities and the large number of degrees of freedom involved. From a multisite homogenization approach, where ideal crystals are assumed to deform in a homogeneous medium with average properties, active slip systems that explain experimentally observed textures in polyphase earth materials have been determined (e.g Miyagi and Wenk, 2016; Kaercher et al., 2016; Merkel et al., 2002) using the visco plastic self consistent code (VPSC) developed by Lebensohn and Tome (1994). These homogeneous medium approaches tend to predict shaper textures than

observed experimentally due to the lack of intra granular misorientation that develops in the physical systems. Furthermore, the size of the problem that is accessible to n-site self consistent formulations are limited by the total number of sites involved in the calculation, even in the idealized case of considering only first neighbor interactions.

The limitations discussed above of both the FEM and n-site self consistent models can be overcome by using a fast Fourier transform (FFT) based algorithm. The FFT formulation was first formulated by Moulinec and Suquet (1998) to determine the local and bulk responses of nonlinear composites. It was presented as an alternative to finite element approaches based on the Fourier series, avoiding meshing and enabling the direct use of experimental microstructure data. The method was originally used to model the behavior of isotropic two phase composites, and has been adapted by Lebensohn (2001) to model the local response of anisotropic polycrystals, where heterogeneities are introduced by grains with directional properties and different crystallographic orientations. The VPFFT code models plastic deformation in viscoplastic anisotropic 3D polycrystals deforming by dislocation glide, it provides an exact solution of the governing equations and has better numerical performance than FEM algorithms that require extensive computer resources that are not always available. Together with an ad-hoc microstructure updating scheme, it calculates local states, morphology and texture evolution in anisotropic polycrystals. It predicts strain localization, intragranular misorientation, sub-grain formation, and predicts smoother textures than self consistent approaches. Recently, the FFT formulation has been adapted to solve elasto-viscoplastic problems to study the role of rotation gradients on the local and effective macro scale mechanical response of nanocrystalline materials (Upadhyay et al., 2016a) and has been used to study lattice strain evolution during uniaxial and biaxial loading of stainless steal (Upadhyay et al., 2016b). This approach has also been used to to model recrystallization of plastically deformed polycrystals in 3D (Chen et al., 2015). Comparisons of measured strain localization in 3D aggregates with predicted strains from elasto-viscoplastic FFT formulations, using experimental microstructures as input, show that model predictions are reasonable in a statistical perspective, but the direct spatial correspondence with measured strain fields is still not accurate (Mello et al., 2016).

The scope of this chapter is to explore plastic deformation of single and two phase (75% bridgmanite + 25% periclase) polycrystalline aggregates by means of the full field viscoplastic fast Fourier transform (VPFFT) code developed by Lebensohn (2001). Particularly, it is of interest to understand the influence of microstructure on texture evolution in polycrystalline aggregates, and to explore the effects of deforming two phases with contrasting material properties in the development of heterogeneities at the local grain scale.

3.2 Methods

The FFT formulation and its particular implementation in the VPFFT code are presented in this section. An brief explanation of how the plasticity equations are solved in VPFFT

are described, for a detailed review of the theory and numerical implementation in the code the reader is referred to Lebensohn (2001). The FFT method solves a cell problem for a representative volume element (RVE) with periodic boundary conditions. There are many problems in which the microstructure is periodic, in which case the size of the RVE is the unit cell that generates the structure by repeating it periodically. When the microstructure of interest is not periodic, the RVE must be chosen to be statistically representative of the whole volume. In the case of this study, ideal microstructures are used and they are considered to be a unit cell in a microstructure that repeats itself periodically. Due to these periodic conditions, there is the implicit assumption that heterogeneities are small compared to the sample dimensions. The FFT formulation does not involve any homogenization assumptions, so that the interactions between regions of the 3D aggregate have no cut-off distance, which means that the interaction of each material point with all the other material points in the RVE is taken into account.

VPFFT Formulation

First a polycrystal (RVE) must be created and discretized into a Fourier grid. In Figure 3.1 and ideal 3D polycrystal adapted from Figure 1 of Lebensohn (2001) is shown to exhibit the discretization of a polycrystal to be used in VPFFT. The RVE has 512 grains arranged in a 8x8x8 regular structure, and each grain is assigned an initial orientation depicted with an arrow (Figure (Lebensohn, 2001)a). Each grain is subdivided into 512 cubes (voxels), also arranged in a 8x8x8 structure (Figure 3.1b). The Fourier grid is 64x64x64 in this case, and Fourier points lie in the centers of the voxels (cubes) that make the grains. Naturally, the voxels that belong to the same grain all start with the same orientation like seen in Figure 3.1b, and as the aggregate is deformed, each voxel rotates according to their local stress state developing intragranular misorientation. The derivation of the basic equations used in VPFFT presented here relies heavily on what is presented in Lebensohn (2001), the reader is referred to this publication for a more detailed description.

The viscoplastic formulation implemented in the VPFFT code involves the solution of the local problem of a inhomogenous viscoplastic medium responding to the application of a velocity gradient V_{ij}. The strain rate D_{ij} and the rotation rate Ω_{ij} are equal to the symmetric and skewsymmetric components of V_{ij}:

$$D_{ij} = \frac{1}{2}(V_{i,j} + V_{j,i}) \tag{3.1}$$

$$\Omega_{ij} = \frac{1}{2}(V_{i,j} - V_{j,i}). \tag{3.2}$$

The VPFFT code considers anisotropic polycrystals deforming by dislocation glide exclusively. Under this assumption, the local behavior of the inhomogeneous viscoplastic medium (the polycrystal) can be described in terms of a tangent approximation (Lebensohn and Tome, 1993):

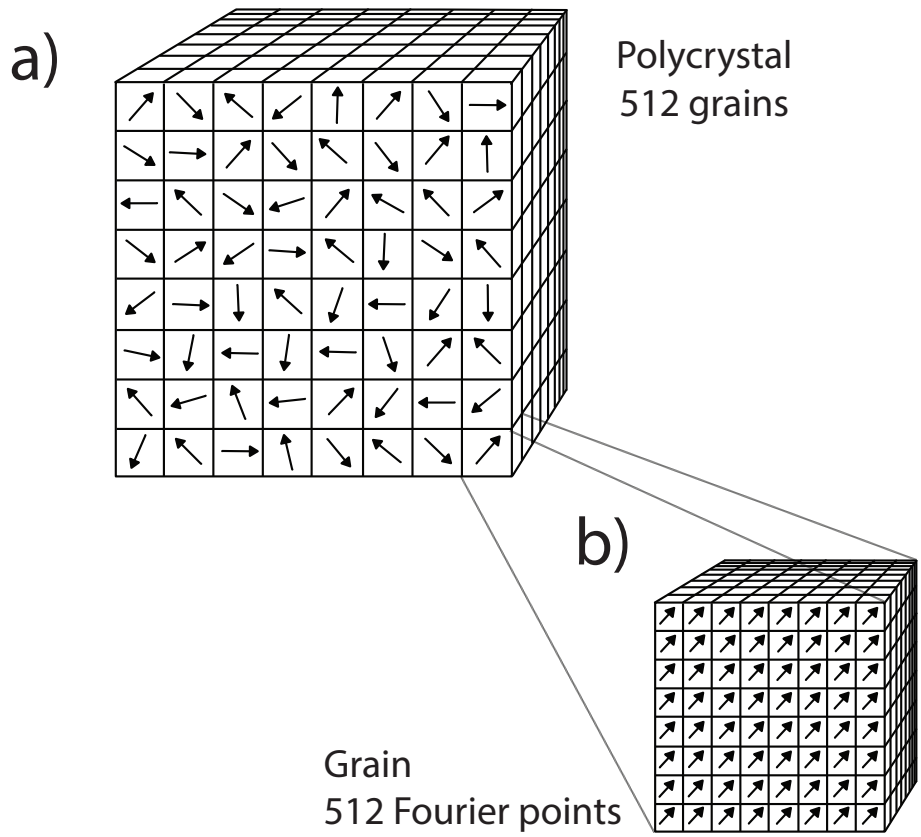

Figure 3.1: *Figure adapted from Figure 1 of Lebensohn (2001). a) Initial idealized polycrystal with 512 grains in a 8x8x8 grid. b) Each grain is subdivided into 512 cubes (voxels) that contain a Fourier point in the center of each one. The total Fourier grid is 64x64x64.*

$$\sigma^{'}(\mathbf{x}) = (M^{tg})^{-1}(\mathbf{x}) : d(\mathbf{x}) + S^{o}(\mathbf{x}), \tag{3.3}$$

where $d(\mathbf{x})$ and $\sigma^{'}(\mathbf{x})$ are the strain rate and deviatoric stress at material point $\mathbf{x}$, $S^{o}(\mathbf{x})$ is a back extrapolated stress term and the tangent compliance modulus $M^{tg}(\mathbf{x})$ is equal to:

$$M^{tg}(\mathbf{x}) = n\dot{\gamma}_o \sum_s \frac{m^s(\mathbf{x}) \otimes m^s(\mathbf{x})}{\tau_o^s(\mathbf{x})} \Big(\frac{m^s(\mathbf{x}) : \sigma^{'}(\mathbf{x})}{\tau_o^s(\mathbf{x})} \Big)^{n-1}, \tag{3.4}$$

where $m^s(\mathbf{x})$ and $\tau_o^s(\mathbf{x})$ are the symmetric Schmid tensor and the critical stress of each slip system , and the sum goes over are all the potentially active slip systems. The inverse of the rate-sensitivity of the material is the viscoplastic exponent n and $\dot{\gamma}_o$ is a normalization parameter. The local inhomogeneities of the system can be expressed as a perturbation to a homogeneous reference medium that can also be described with the tangent approximation:

$$\Sigma^{'} = L_o^{tg} : D + S^{oo}, \tag{3.5}$$

where L_o^{tg} is the tangent stiffness, S^{oo} the back extrapolated stress and D the strain rate of the reference homogeneous medium. Assuming incompressibility, the system of equations to solve is:

$$\begin{cases} L_{o_{ijkl}}^{tg}(\mathbf{x}) + \tau_{ij,j}(\mathbf{x}) - p_{,i}(\mathbf{x}) = 0 & \text{in RVE} \\ v_{k,k}(\mathbf{x}) = 0 & \text{in RVE} \\ \text{periodic boundary conditions across RVE} \end{cases} \tag{3.6}$$

where $v_k(\mathbf{x})$ is the velocity field. Given this set of equations, the perturbation field that describes the deviation of the viscoplastic medium from the homogeneous reference medium can be written as:

$$\tau_{ij} = \tilde{\sigma}_{ij}^{'} - L_{o_{ijkl}}^{tg}\tilde{d}_{kl}, \tag{3.7}$$

where $\tilde{d} = d - D$ is the local fluctuation of the strain-rate, and $\tilde{\sigma}^{'} = \sigma^{'} - \Sigma^{'}$ is the local fluctuation of the deviatoric stress. In VPFFT, the system of equations 3.6 is solved using the Green functions method (Lebensohn et al., 1998; Roatta et al., 1997):

$$\begin{array}{l} L_{o_{ijkl}}^{tg} G_{km,lj}(\mathbf{x} - \mathbf{x}^{'}) + H_{m,i}(\mathbf{x} - \mathbf{x}^{'}) + \delta_{im}\delta(\mathbf{x} - \mathbf{x}^{'}) = 0 \\ H_{km,K}(\mathbf{x} - \mathbf{x}^{'}) = 0 \end{array}, \tag{3.8}$$

where $H_{m,i}(\mathbf{x}-\mathbf{x}^{'})$ is the hydrostatic pressure, and $G_{km,lj}(\mathbf{x}-\mathbf{x}^{'})$ is the velocity component in the $x - k$ direction at the point $\mathbf{x}^{'}$ that results when a unit force is applied in the $\mathbf{x}m$ at point $\mathbf{x}^{'}$ of the RVE. If one solves the system of equations using the Green function method in Equation 3.8, the perturbation of the velocity with respect to the homogeneous reference medium can be written as a convolution:

$$\tilde{v}_k(\mathbf{x}) = \int_{R^3} G_{ki}(\mathbf{x} - \mathbf{x}^{'})\tau_{ij,j}(\mathbf{x}^{'})d\mathbf{x}^{'}. \tag{3.9}$$

After integrating by parts, renaming $\Gamma_{ijkl} = G_{ik,jl}$, and transforming into Fourier space, equation 3.9 can be re-written as:

$$\hat{\tilde{v}}_{ij} = \hat{\Gamma}_{ijkl}\hat{\tau}_{kl}. \tag{3.10}$$

$\hat{\Gamma}_{ijkl}$ can be calculated by taking the Fourier transform of Equations 3.8 and doing some tensor algebra:

$$\hat{\Gamma}_{ijkl} = -\xi_j\xi_l\hat{G}_{ik}, \tag{3.11}$$

where ξ is a point of Fourier space or frequency. With $\hat{\Gamma}_{ijkl}$ and $\hat{\tau}_{kl}$, $\hat{\tilde{v}}_{ij}$ can be calculated by solving Equation 3.10. Nonetheless, the perturbation field in real space τ_{ij} is not known,

since it depends on the local fluctuations of the stress and strain-rate, see Equation 3.7. In consequence, an initial guess of the deviatoric stress $\tilde{\sigma}'$ and the local fluctuations of the strain-rate $\tilde{d}$ must be made, and the problem solved iteratively with an appropriate convergence criteria, refer to Lebensohn (2001) for a detailed derivation. For each step in the iteration, the perturbation in the velocity field $\tilde{v}_{i,j}$ in real space can be calculated by taking the Fourier transform of Equation 3.10, and the local fluctuation of the strain-rate and rotation-rate can be obtained by taking the symmetric and skewsymmetric components of $\tilde{v}_{i,j}$:

$$\tilde{d}_{ij} = d_{ij} - D_{ij} = \frac{1}{2}(\tilde{v}_{i,j} + \tilde{v}_{j,i}), \tag{3.12}$$

$$\tilde{\omega}_{ij} = \omega_{ij} - \Omega_{ij} = \frac{1}{2}(\tilde{v}_{i,j} - \tilde{v}_{j,i}). \tag{3.13}$$

After convergence is achieved and anti-transforming back to real space, the macroscopic velocity is calculated using:

$$v_i(\mathbf{x}) = V_i(\mathbf{x}) + \tilde{v}_i(\mathbf{x}) \tag{3.14}$$

where $V_i(\mathbf{x})$ is the velocity field that is a result of the applied velocity gradient $V_{i,j}$.

Basic Operation of the VPFFT Codex

In the following section, the basic structure of the VPFFT code will be introduced, describing the input and output files for the pre and post processing scripts, and for the main code. A flow chart showing the general steps that must be followed is shown in Figure 3.2, where red boxes are scripts (typically written in Fortran) that must be compiled and executed, navy blue boxes are text files containing input and output information, light blue boxes are image files and black arrows indicate input, while green arrows indicate output. One must start a microstructure for the VPFFT code to use. In the case of this study idealized microstructures are created using the voro1.for and voro2.for that create arrays, table1 and table2, that contain grain and position information. The orient file is then used to assign orientations to the grains. It is also possible to input microstructure information obtained from experimental data, in this case it is necessary read grain numbers and orientations in a discrete cubic regular grid and write in a .dat file with the format like described in the following pre-processing section. Once the microstructure information is written in the .dat file format, simulation parameters must be set in the fft.in file where the velocity gradient, number of phases, strain step size and number of steps, maximum iterations and other parameters are set. The single crystal properties files, .sx files, have the slip system information for each phase. After the VPFFT simulation is performed and converged, a number of output files are generated with slip system activity information, stress-strain data, strain rate, stress tensor and orientation for each material point (voxel). The stress

or strain rate fields can be processed using the post.for script and plotted in 2D using the gnuplot program. 3D plots can also be done in the software ParaView (Ahrens et al., 2005) or VisIt (Childs et al., 2012) by using the vtknew.for script. A detailed explanation of all the input and output files is presented below.

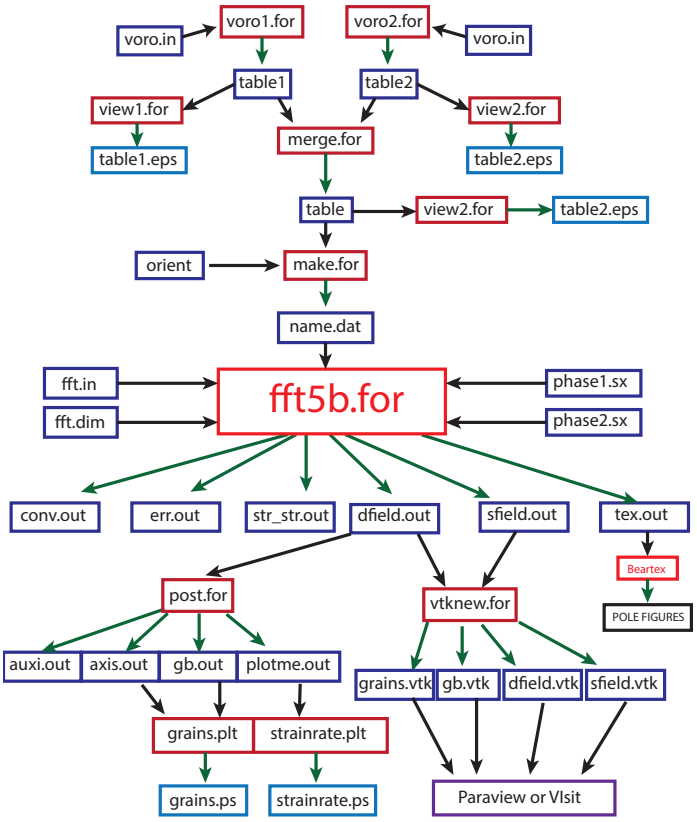

Figure 3.2: *Flow chart depicting the process to run a VPFFT simulation, including pre-processing of ideal microstructures and post processing results. Scripts that must be compiled and executed are in red boxes, text files containing input/output information in navy blue boxes and image files in light blue boxes. Black arrows indicate input and green arrows indicate output.*

Pre-processing

voro1.for and voro2.for Generates a set of 64x64x64 points and assigns grain numbers to each one. This program creates the initial microstructure that will be used in VPFFT. voro1 creates the microstructure for phase 1 with negative grain numbers in the places where grains of phase 2 are inserted in a later step. voro2 creates the microstructure for grains of phase 2, these have a high grain number for plotting purposes.

- Input
  - voro.in
- Output
  - table1 or table2

voro.in Assigns values to variables used in voro.for
NGR= number of grains
NPTS= number of points
NEIGH= this variable is not used
RANDOM SEED= random seed for voronoi cell generation

table1 This file is the output of voro1.for. It contains a 64x64x64 array of numbers organized as 64x64 matrices for each k=n (where n is an integer that goes from 1 to 64). These are 2D sections at each k coordinate. Negative numbers are placeholders programmed in selected spots for where the grains of face two will be merged in.

view1.for This program creates an .eps file from table1. It is an image of the microstructural information contained in table1. You can open the .eps file with the image viewer of your choice.

- Input
  - table1
- Output
  - table1.eps

table2 Same format as table1, a series of k = n slices with arrays corresponding to each Fourier point and the grain number assigned to it. table2 has information of phase 2, in this case phase 2 has smaller grains. The idea is to generate a second microstructure that fills the whole cube, this microstructure will contain the grain size that is desired for phase 2. Grains of phase 2 are assigned higher numbers by voro2.for so when they are plotted together with phase 2 there is some color contrast in between the phases, phase 1 would correspond to the low grain number values and phase 2 would correspond to the colors from high grain number values.

view2.for This program creates an .eps file from table2. It is an image of the microstructural information contained in table2.

- Input
  - table2
- Output
  - table2.eps

merge.for This program merges table1 and table2 into table. Basically replaces the negative values in table1 with the grain number on that position in table2. This is the microstructure that will be used by VPFFT.

- Input
  - table1
  - table2
- Output
  - table

orient File with list of random Euler angles and a weight. Must have a least as many rows as grains in the microstructure.

Columns: (phg, thg, omg, 1)

make.for Assigns an orientation to each grain in table, as well as a phase number, and is the initial microstructure that will be used by the VPFFT code. You assign the .dat file name here.

- Input
  - orient
  - table
- Output
  - name.dat

name.dat Initial microstructure to be used in FFT. Gives the three Euler angles, Fourier point coordinates, grain number and phase number for each Fourier point.

Columns: (phg, thg, omg, i, j, k, grain number, phase number)

VPFFT

fft.in Contains general information for fft calculations. Here the user inputs number of phases, number of Fourier points, name of .dat file to be used, name of .sx files containing slip system information for each phase. Also conditions for deformation can be assigned in this file, in our case it is set to deform under compression along the sample z axis. Strain is assigned in the variable equincr in the *other section of the file.

- Input
  - phase1.sx
  - Phase2.sx
  - name.dat

phase1.sx Lists slip system activities of phase. The user may choose the name of this file and must write it in fft.in. Contains crystallographic information of the phase and main slip system activities.

icryst symmetry group of phase crystal axes a, b,c unit cell values nmodesx total number of modes written in the file nmode number of modes to be used in the calculations mode(i) lists of the slip systems to be used

$(1\,1\,1)$ $\langle 1\,0\,\bar{1}\rangle$ SLIP example of how you define a slip system

modex,nsmx,nrsx,gamd0x,twshx,isectwx

tau0xf,tau0xb,tau1x,thet0,thet1

hselfx,hlatex

Then list all equivalent slip systems by symmetry, for each slip system written in file.

You will need a second file like this containing the information for phase2.

fft.dim Defines variables and dimensions for fft5.for.

fft5.for This is the actual program that does viscoplastic modeling. It starts with the initial microstructure on the .dat file and applies the stress field of the users choice in fft.in. The program then uses the fft method to solve viscoplastic law for the strain of each grain, considering their deformation by slip systems stated in the .sx file. The output is the orientation of each grain of the mesh after deformation, strain field, strain rate filed, and others. You must compile this fortran source code file to obtain an executable than when executed performs all the calculations.

- Input
  - fft.in
  - name.dat

  - phase1.sx
  - phase2.sx

- Output
  - dfield.out
  - sfield.out
  - conv.out
  - err.out
  - str_str.out

conv.dat Tells you strain steps and number of iterations.

dfield.out List of strain rate for each point in the mesh.
Columns: (i, j, k, grain number, phase, $\dot{e}11$, $\dot{e}22$, $\dot{e}33$, $\dot{e}23$, $\dot{e}13$, $\dot{e}12$)
This file is created in the FIELDS.OUT section of fft5.for.

sfield.out List of strain for each point in the mesh.
Columns: (i, j, k, grain number, phase, e11, e22, e33, e23, e13, e12)
This file is created in the FIELDS.OUT section of fft5.for.

err.out States various error calculations for each iteration. Prints slip system activities.
Columns: (Iteration, ERRD, ERRS, DVM, SVM, ACT)

str_str.out Gives only one line containing values for variables in err.out with values of strain and strain rate.
Columns: (EVM, DVM, SVM, no name column, $\dot{e}11$, $\dot{e}22$, $\dot{e}33$, $\dot{e}23$, $\dot{e}13$, $\dot{e}12$, e11, e22, e33, e23)

tex.out Final discrete orientation file.
Columns: (ph, th, om, strain, i, j, k, grain number, phase)

Post-processing

post.for Post-processing script that makes a 2D slice of the 3D mesh in the XY, XZ or YZ plane. It creates files that contain grain and strain information that can be later visualized in a 2D plot.
Script prompts:

SELECT PLANE: (1) YZ - (2) XZ - (3) XY ->

SELECT LEVEL (1...64) ->

- Input
  - dfield.out
- Output
  - auxi.out: Array containing grain number and location information
  - axis.out: Names axes and size ratio
  - gb.out: Plotting parameters
  - plotme.out: (list of (i, j), (i, k) or (j, k) Fourier points, strain rate, Grain number)

grains.plt Gnuplot script that creates a postscript file from plotme.out. It plots the Fourier points with their corresponding boundaries and phase distinction. Postscript file must then be converted to pdf for viewing with the program of your choice (Adobe Acrobat should be able to do it). It is the plot of the slice selected in post.for.

You must download gnuplot and run this script by typing the command: gnuplot> load grains.plt

- Input
  - axis.out
  - gb.out
  - plotme.out
- Output
  - grains.ps

strainrate.plt Gnuplot script that creates a postscript file from plotme.out. Plots the Von Misses strain-rate in the section selected in post.for.

- Input
  - axis.out
  - gb.out

  - plotme.out

- Output
  - strainrate.ps

vtknew.for Script that prepares .vtk files for plotting in ParaView or VisIt. It creates separate vtk files for the grains, grain boundaries, strain rate and stress field.

- Input
  - sfield.out
  - dfield.out
- Output
  - grains.vtk
  - gb.vtk
  - sfield.vtk
  - dfield.vtk

Simulation Parameters

A total of six simulations were carried out using the VPFFT code. All of the microstructures were composed of a grid of 64x64x64 Fourier points. Simulations were done with a total of 6 steps of 5% strain to achieve a total of 30% strain, and there are 100 iterations in each step. The polycrystalline aggregates were deformed under compression with the following applied velocity gradient $V_{i,j}$:

$$\begin{pmatrix} 0.5 & 0 & 0 \\ 0 & 0.5 & 0 \\ 0 & 0 & -1 \end{pmatrix}.$$

Figure 3.3 shows the four different microstructures used in VPFFT simulations. Blue-green-yellow colors correspond to phase 1 and orange-red colors to phase 2. Grains of the harder bridgmanite phase 1 are 5 times larger than those of the softer periclase phase 2, with 75% and 25% volume fractions respectively . The core microstructure in Figure 3.3a is a microstructure with periclase grains in the core of the larger bridgmanite grains. This microstructure could arise when two phases nucleate after the phase transformation from a single phase, where the minority phase nucleates in the cores of the parent phase. The core microstructure has 300 bridgmanite grains and 1587 periclase grains. The percolate microstructure in Figure 3.3b is one where the soft phase 2 is interconnected and completely

surrounding all of the grains of the hard phase 1 (e.g Zhang et al., 2013); it has 55 grains of phase 1 and 79 grains of phase 2. A random microstructure is shown in Figure 3.3c where the grain numbers for phase 2 are selected randomly and tend to form clusters. These type of microstructures are found in many polyphase systems and are observed experimentally in deformation experiments of bridgmanite and periclase analog materials (Kaercher et al., 2016). The random microstructure has 300 hard phase 1 grains and 1337 grains of phase 2. A microstructure where grains of phase 2 are in triple junctions of the larger grains of phase 1 is shown in Figure 3.3d. This microstructure has 300 bridgmanite grains and 1751 periclase grains, this is also a common two phase microstructure (e.g. Gottstein et al., 2005). The two single phase simulations were performed using the random microstructure, assigning all the grains to the bridgmanite and the periclase phase respectively.

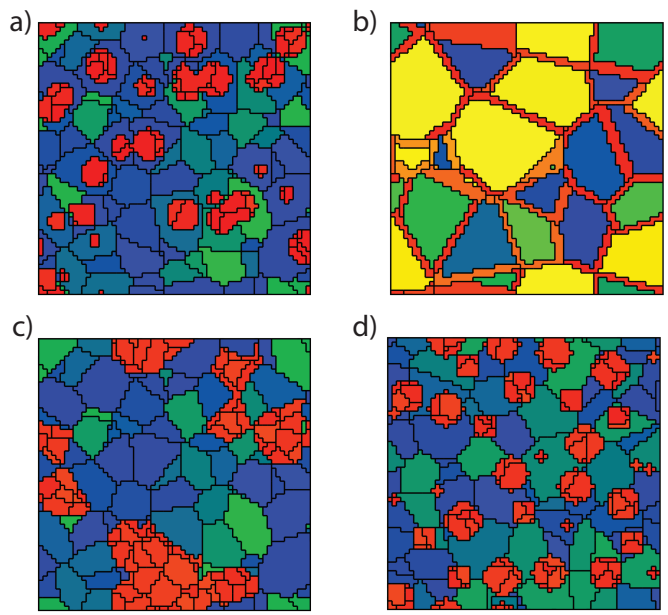

Figure 3.3: *2D slices along the XY plane of the four different microstructures used in the VPFFT simulations. All microstructures have two phases with 75% and 25% of relative volume fraction and phase 2 has grains 5 times smaller than those of phase 1. In general cool colors correspond to grains of phase 1 and orange to red colors correspond to grains of phase 2, and phase 1 is assigned to bridgmanite and phase 2 to periclase. a) The core microstructure has grains of phase 2 in the interior of the larger phase 1 grains. b) The percolate structure has grains of phase 2 surrounding the larger grains of phase 1, grains of phase 2 are only 1 voxel wide. c) A random microstructure where the grains of phase 2 are selected randomly. d) In the triple junction microstructure the grains of phase 2 are in the triple junctions of the large phase 1 grains.*

3.3 Results

In order to understand the influence of microstructure in the evolution of the orientation of grains of a polycrystalline aggregate a suite of four different virtual microstructures have been created. In the case of this study phase 1 is the bridgmanite orthorhombic phase and phase 2 is the cubic periclase phase. The phases have 75% and 25% volume fractions respectively. Phase 2 is 3 times softer than phase 1 (Girard et al., 2016) and the aggregates are compressed up to 30% strain along the z axis. In Figure 3.3 2D sections of four different proposed microstructures are shown. The VPFFT code outputs stress and strain rate tensors for each material point, the equivalent stress and strain rate are shown in 3D representations of the different aggregates in Figure 3.4 in order to exhibit general trends in the distribution of these quantities across the different phases. To understand the influence of microstructure in texture evolution of these two phase aggregates, inverse pole figures of the compression direction are calculated using the software BEARTEX and plotted for the four microstructures in Figure 3.5. Slip system activity shown in Table 2.1 gives information on how the total deformation is distributed between the two phases, and particularly is auxiliary in explaining differences in texture maxima of the different microstructures. The strain rate tensor is calculated at each material point (voxel) by the VPFFT code. The distribution of the strain rate after 30% strain is calculated, and the differences between the microstructures are displayed in Figure 3.6. It is of interest to understand deformation at the local grain scale. For this purpose, voxels at grain boundaries versus grain interior voxels are separated, and their probability density function is calculated, comparing the behavior of these different voxels with other voxel types in the same aggregate in Figure 3.7. Strain rate distributions of voxels of the same type across the different microstructures are also compared (Figure 3.8). Finally, single phase simulations are done using the random microstructure with both the bridgmanite and periclase material properties separately. This is done to compare results with two-phase deformation and discern between the effects of having two phases, and the effect of anisotropy due to the single crystal material properties on plastic deformation.

It is of interest to explore the influence of the local grain environment on plastic deformation due to dislocation glide. In particular, how it affects grain rotation due to dislocation glide and what is the subsequent texture evolution. In metals, these relationships have been studied from a variety of different approaches (e.g. Dey et al., 2009), but little information is available for the bridgmanite and periclase aggregate in terms of the expected microstructure in the lower mantle of the Earth (e.g. Girard et al., 2016; Miyajima et al., 2009), and what the influence of this microstructure on texture development is. Here we present a study with four idealized microstructures. General trends of the equivalent stress and equivalent strain rate provide information on how these fields are distributed in the different phases. Studies show that the stress distribution within a polycrystalline aggregate varies systematically with the anisotropy of the single crystal, and probably also depends on orientation (Kumar et al., 1996). In Figure 3.4 3D plots of the microstructure after 30% strain are shown in

column 1, the equivalent stress distribution for the four different microstructures in column 2 and the equivalent strain rate values at each voxel (pixel) in column three. It is observed that, in general, phase 2 is the one that accommodates most of the deformation, due to the high strain rates and low stress it presents. In contrast, phase 1 has high stress values particularly in the interior of grains and low strain rates reflecting little plastic deformation (Figure 3.4b). This is in agreement with experimental studies done on $CaGeO_3$ perovskite + MgO (periclase) aggregates (analog system to the bridgmanite periclase system) under high pressure and temperature, where they find that the stresses in the MgO phase are about a factor of 2 lower than those in the $CaGeO_3$ perovskite (Wang et al., 2013). Furthermore, stress distribution of the grains of phase 2 appear to be homogeneous, as opposed to the stress distribution of phase 1 that is considerably heterogeneous. The largest contrast in the equivalent strain rate between phase 1 and phase 2 is observed in the percolate microstructure (Figure 3.4b), where phase 2 shows a higher equivalent strain rate than grains of phase 1.

Texture Evolution

Inverse pole figures (IPF) of the compression direction are plotted using the software BEARTEX (Wenk et al., 1998) by calculating an orientation distribution function from the discrete orientations that VPFFT outputs (Figure 3.5). IPF's of both the orthorhombic phase 1 and the cubic phase 2 show maxima in similar places for the four different microstructures (Figure 3.5a-d), showing only small variations between them. The texture of the orthorhombic phase in the percolate microstructure shown in Figure 3.5b lies outside of the general trend, having a very sharp texture with a maximum of 4.43 multiples of random distribution (m.r.d.). The softer periclase phase shows a lower texture when compared to the bridgmanite phase, but they both have close to no texture with a maximum at 1.53 m.r.d, excluding the bridgmanite IPF for the percolate microstructure. The random microstructure develops the strongest texture in both the orthorhombic and the cubic phase when the core, random and triple junction microstructures are compared. The strong bridgmanite texture seen in the percolate phase requires careful interpretation due to the small number of grains that this microstructure contains.

Slip systems for the bridgmanite and periclase phase are selected from experimental and modeling efforts (e.g. Miyagi and Wenk, 2016; Gouriet et al., 2014; Wang et al., 2013; Cordier, 2002; Merkel et al., 2002; Amodeo and Cordier, 2012) (Table 3.1), and hypothetical critical resolved shear stress (CRSS) values are selected in order to understand the effect of microstructure and the local grain environment in grain rotation and subsequent texture development in these two phase aggregates. Bridgmanite is assumed in these simulations to have a dominant $(0\,0\,1)\langle 1\,1\,0\rangle$ slip system with a relative CRSS value of 1.5. All other slip systems have a relative CRSS value of 3 except for the $\{1\,1\,1\}\langle 0\,1\,\bar{1}\rangle$ which is used to close the single crystal yield surface (SCYS) since the physically possible slip systems of bridgmanite do not close them on their own. The $\{1\,1\,1\}\langle 0\,1\,\bar{1}\rangle$ has a relative CRSS of 250 so it closes the SCYS but is not activated. This introduces a very anisotropic (flat shaped)

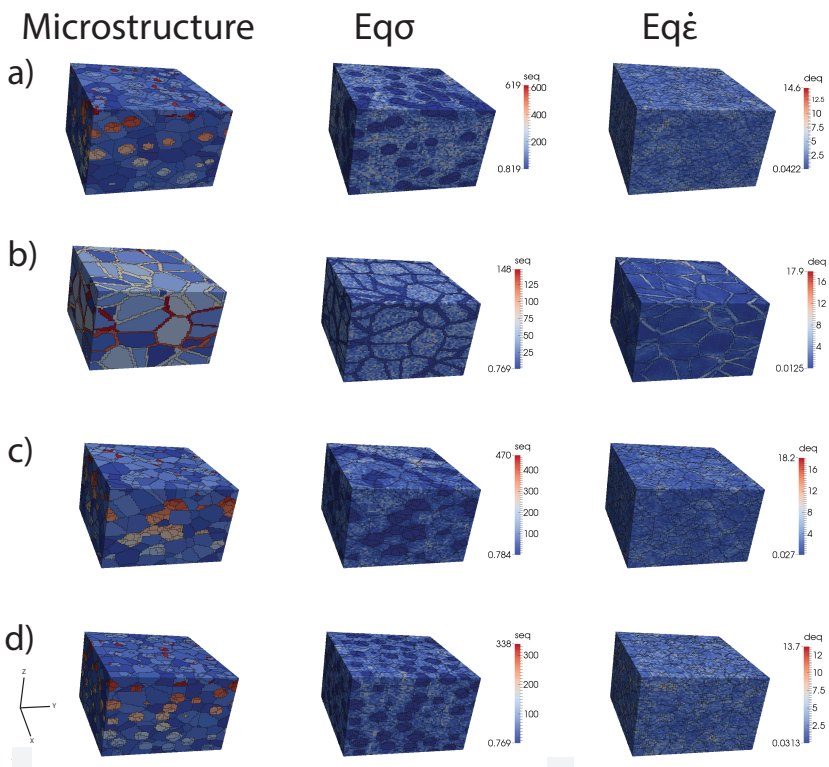

Figure 3.4: *Plots of the microstructure, equivalent stress ($Eq\sigma$) and equivalent strain rate ($Eq\dot{\epsilon}$) in the 3D aggregates after 30% strain. a) Core microstructure. Notice how there is low stress in the interior soft periclase grains. b) Percolate microstructure. Stress is highest in interior of the hard bridgmanite grains and lowest in the surrounding periclase grains due to their high deformation rates. c) Random microstructure. High deformation rates in the soft grains is observed in both interconnected and isolated grains. d) Triple junction microstructure. The general trend across all microstructures is a low stress and high deformation rates in the soft phase 2 and the opposite for the hard phase 1.*

SCYS. The periclase phase is selected to be 3 times softer than the bridgmanite phase by designating a relative CRSS value of 0.5 for the softest $\{1\,1\,0\}\langle\bar{1}\,1\,0\rangle$ slip system. Slip system activity behavior is the same for the core, random and triple microstructures. In bridgmanite most of the deformation is concentrated in the softest $(0\,0\,1)\langle1\,1\,0\rangle$, where about 30% of the total deformation is concentrated. Then follows the $(1\,0\,0)\langle0\,1\,1\rangle$, $(0\,1\,0)\langle1\,0\,1\rangle$, $(0\,1\,0)[1\,0\,0]$ and $(1\,0\,0)[0\,1\,0]$ with about 8% of the total deformation carried by each one. The periclase phase exhibits a similar behavior, slip system activity is the same for the core, random and triple microstructures with most of the activity concentrated in the $\{1\,0\,0\}\langle0\,1\,1\rangle$ slip system, carrying about 15% of the total activity. It is important to note that this $\{1\,0\,0\}\langle0\,1\,1\rangle$ carries most of the deformation despite the fact that it is not the softest slip system of the periclase phase. Activity of the $\{1\,1\,1\}\langle0\,1\,\bar{1}\rangle$ and the softest $\{1\,1\,0\}\langle\bar{1}\,1\,0\rangle$ follows, with

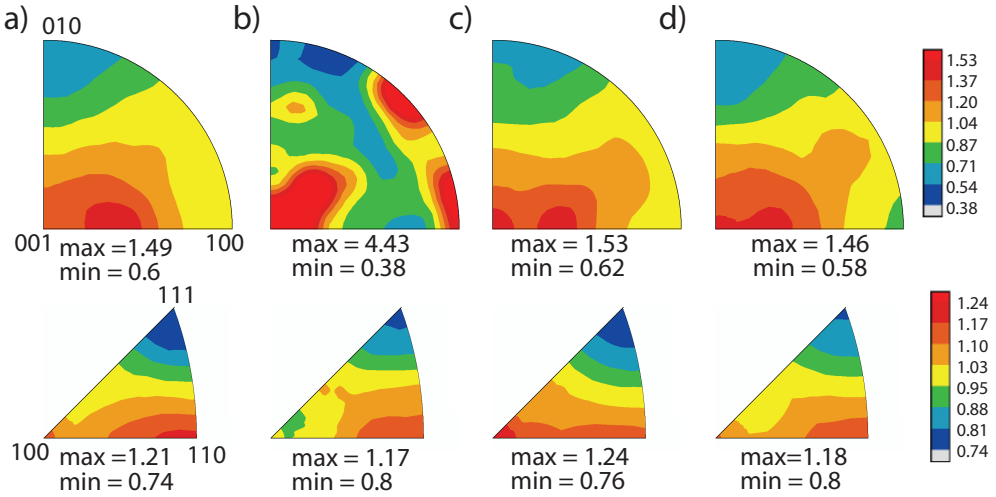

Figure 3.5: *Inverse pole figures of the compression direction shown for the four different microstructures a) core, b) percolate, c) random and d) triple junction after 30% strain. Location of maxima is very similar for all four microstructures and for all, except the percolate microstructure, the texture is very weak in both phases. The percolate microstructure shows a particularly sharp texture of the bridgmanite phase. Pole figures plotted in BEARTEX.*

about a 10% of total activity on each one. The percolate microstructure presents a different behavior, the order of most to least active systems remains the same with respect to the core, random and triple microstructures, but the relative activity between bridgmanite and periclase changes. In the percolate structure the activity between phase 1 and phase 2 is almost equally distributed, with a 45% of the activity in the bridgmanite phase and 55% of the activity in the periclase phase. For the core, random and triple microstructures, most of the deformation is carried by the harder bridgmanite phase, with a total activity of 65% on average. This result contradicts experimental findings on this two phase system, that through various experimental and modeling efforts have found that most of the deformation is carried by the softer periclase phase (e.g Miyagi and Wenk, 2016; Girard et al., 2016; Cordier et al., 2012).

Strain Rate Distributions

Inverse pole figures of the compression direction and slip system activities show that the core, random and triple junction microstructures have similar behaviors, with most of the deformation concentrated in the bridgmanite phase and very little texture development in both bridgmanite and periclase. The bridgmanite phase shows stronger texture in the percolate microstructure and in this case deformation is equally distributed between the two

	Bridgmanite								**Periclase**				
n	$(1\,0\,0)$	$(1\,0\,0)$	$(0\,1\,0)$	$(0\,1\,0)$	$(0\,0\,1)$	$(0\,0\,1)$	$(0\,0\,1)$	$\{1\,1\,1\}$	$\{1\,1\,1\}$	$\{1\,1\,0\}$	$\{1\,0\,0\}$		
b	$[0\,1\,0]$	$\langle 0\,1\,1\rangle$	$[1\,0\,0]$	$\langle 1\,0\,1\rangle$	$[1\,0\,0]$	$[0\,1\,0]$	$\langle 1\,1\,0\rangle$	$\langle 0\,1\,\bar{1}\rangle$	$\langle 0\,1\,\bar{1}\rangle$	$\langle \bar{1}\,1\,0\rangle$	$\langle 0\,1\,1\rangle$		
CRSS	3	3	3	3	3	3	1.5	250	1	0.5	1		
Slip Activity	**Bridgmanite**								**Periclase**			**SumBrdg**	**SumM**
Core	0.076	0.086	0.076	0.078	0.023	0.02	0.294	0.006	0.098	0.093	0.151	0.658	0.342
Percolate	0.043	0.056	0.043	0.05	0.018	0.015	0.23	0	0.155	0.148	0.24	0.457	0.543
Random	0.074	0.085	0.074	0.077	0.023	0.02	0.293	0.002	0.101	0.099	0.153	0.647	0.353
Triple	0.075	0.086	0.075	0.077	0.023	0.019	0.294	0	0.101	0.097	0.154	0.649	0.351

Table 3.1: *Slip systems, slip system CRSS values and activity for the four different microstructures.*

phases. The distribution of the 33 component of the strain rate tensor (where 33 is the compression direction) is calculated for all voxels of each microstructure and compared in Figure 3.6. These plots are calculated by taking the discrete values of the $\dot{\epsilon}_{33}$ component for each material point (voxel) and making a kernel density estimation to estimate the probability density function of the data. In Figure 3.6, the probability density function (PDF) of $\dot{\epsilon}_{33}$ is plotted for the core microstructure in blue, the percolate microstructure in green, the random microstructure in purple and the triple junction microstructure in orange. Distributions of $\dot{\epsilon}_{33}$ values confirm that the core, random and triple microstructures have similar behavior and shows that the percolate microstructure has a more narrow distribution of the $\dot{\epsilon}_{33}$ component than the other microstructures, indicating a more homogeneous deformation environment. Other simulation efforts done by Zhao and Tryon (2004) show that while grain orientation has a large effect on the evolution of the stresses at the local grain scale, grain size and shape have little effect on this micro-stress distributions. These findings could explain the similarities between the core, random and triple microstructure $\dot{\epsilon}_{33}$.

The probability density function (PDF) of the 33 component of the strain rate is calculated for different types of voxels in order to exhibit differences in the distribution of the strain rate along the compression direction of voxels that are at grain boundaries compared to those in the interior of grains. Plots of the PDF of the $\dot{\epsilon}_{33}$ values for six different types of voxels are shown in Figure 3.7. The types of voxels are labeled with two numerical values. In the first position is the phase of the voxel in question and in the second position it is the number 0 if none of the first neighbors of the voxel are of a different grain, the number 1 if at least one of the first neighbors of the voxel in question is of a different grain of phase 1 and a number 2 if one of its first neighbors is in a different grain of phase 2. Following this labeling scheme, 11 voxels are voxels of phase 1 at grain boundaries with another grain of phase 1 (the percolate structure does not have these type of voxels by construction), 12 voxels are voxels of phase 1 at grain boundaries with a grain of phase 2 and 10 voxels are voxels of phase 1 that are at the interior of the grains. Similarly for phase 2, 20 voxels are voxels of phase 2 in grain interiors (percolate does not have this type of voxel by construction), 22 voxels are voxels of phase 2 that are at grain boundaries with phase 2 and 21 voxels are voxels of phase 2 that are at grain boundaries with phase 1. Voxels are labeled using a script

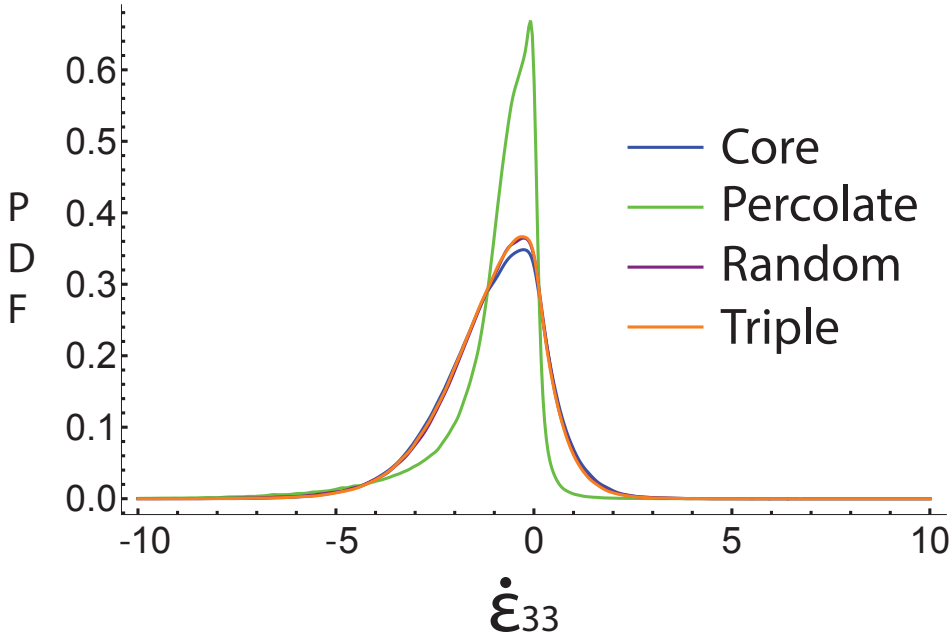

Figure 3.6: *The probability density function (PDF) of the $\dot{\epsilon}_{33}$ component of the strain rate tensor for all voxels is calculated and compared. The x-axis shows values of the 33 component of the strain rate tensor, and the y-axis is the PDF value as calculated after smoothing the discrete strain rate values into a smooth kernel distribution function. PDF values are the same for the core, random and triple microstructures, while the percolate structure shown in green has a more narrow distribution of values, indicating a less heterogeneous deformation environment.*

shown in Appendix B. In Figure 3.7a-d it is observed that the 22 and the 21 voxels, i.e. voxels of phase 2 at grain boundaries, have a wider distribution of $\dot{\epsilon}_{33}$ values. This indicates a more heterogeneous deformation environment in the grain boundaries of phase 2 than anywhere else in the aggregate, including the interior of grains of phase 2. The percolate microstructure shows a larger contrast between distributions of $\dot{\epsilon}_{33}$ values for the 22 and 21 voxels with respect to the other four voxel types.

A comparison of the PDF of the $\dot{\epsilon}_{33}$ values for each voxel type for the four different microstructures shown in Figure 3.8 confirms that the core, percolate and triple junction microstructures have the same behavior at the interior of the grains and grain boundaries of both phase 1 and phase 2. Furthermore, 10 and 12 voxels of the percolate structure have a more narrow distribution than those same type of voxels in the other three microstructures, see Figure 3.8a and c, but voxels of phase 2 at grain boundaries (22 and 21 voxels) have the same distribution in the percolate microstructure than in the other three, see Figure 3.8e and f.

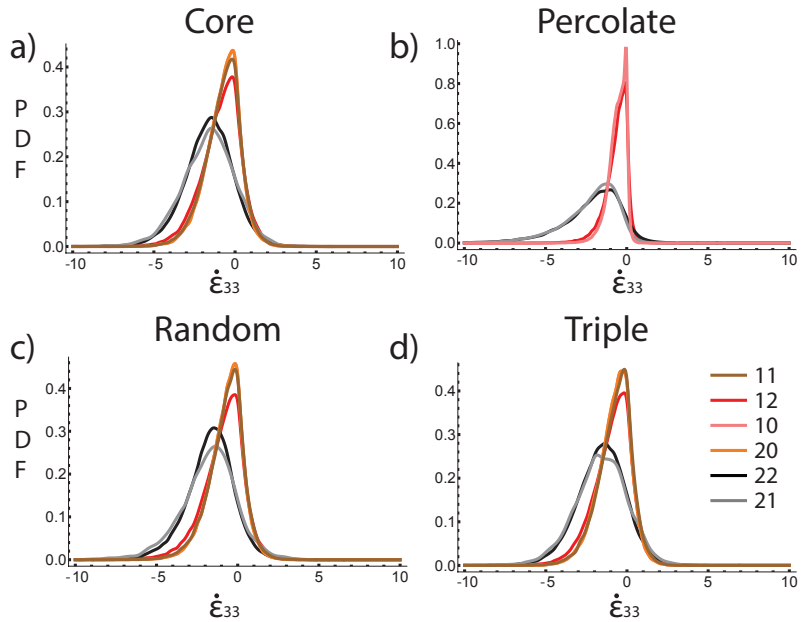

Figure 3.7: *Voxels at grain boundaries are separated from interior voxels and PDF of $\dot{\epsilon}_{33}$ is calculated for the different types. The 11 voxel type corresponds to voxels of phase 1 that are at grain boundaries with another grain of phase 1, 12 voxels are voxels of a grain of phase 1 that are at grain boundaries with grains of phase 2 and the 10 voxels are voxels of phase 1 grains that are not at a grain boundary. As for voxels from grains of phase 2, the same labeling scheme is applied. 20 voxels are voxels of phase 2 grains that are in the interior of the grain (the percolate microstructure does not have this type of voxel by construction), 22 voxels are voxels of grains of phase 2 that are at grain boundaries with a grain of phase 2 and the 21 voxels are at grain boundaries with phase 1. PDF are compared for the different voxel types for each microstructure, a) core microstructure, b) percolate microstructure, c) random microstructure and d) triple microstructure. Legend shows colors of PDF curve to each voxel type using the labels described above. Notice that the general trend is the same for all microstructures, 22 and 21 voxels have a wider distribution than all the other voxels, including the 20 voxel type. Voxels labeled using script in Appendix B.*

Single Phase Deformation

Single phase simulations were performed for comparison with the two phase simulations. In particular, it is of interest to discern the origin of heterogeneities in the strain rate of different material points in the aggregate, the spread of orientations of voxels within a single grain, and the effect of these heterogeneities in the bulk texture. Two single phase simulations were carried out using the same random microstructure as for the two phase case. One with all the grains pertaining to the bridgmanite phase and another simulation with only periclase grains. The aggregates were deformed up to 30% strain using the same

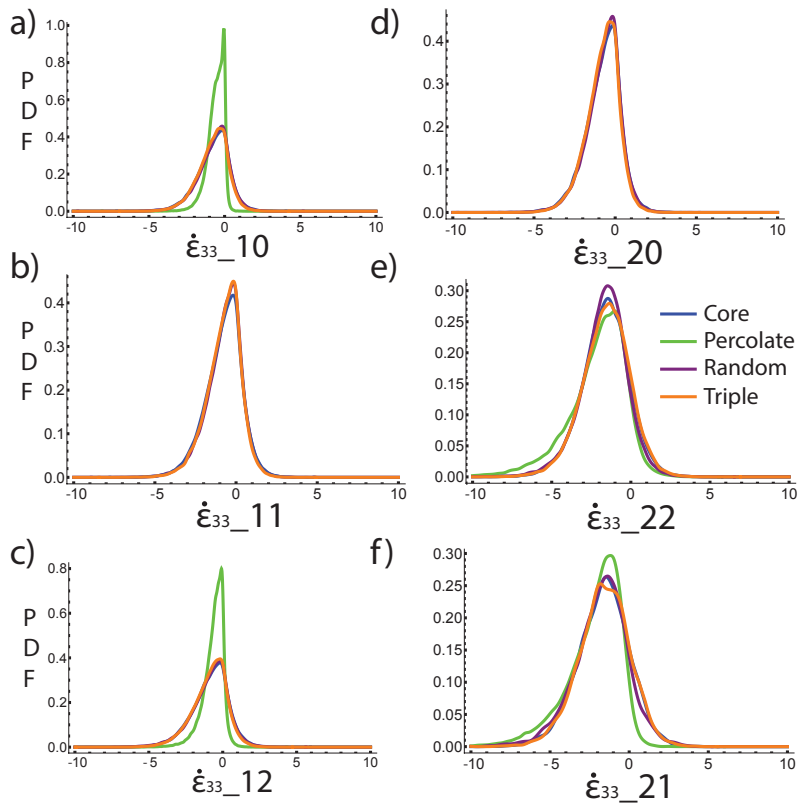

Figure 3.8: *PDF of $\dot{\epsilon}_{33}$ for each voxel type are compared across the different microstructures to display differences in the behavior of grain boundary and interior voxels. a) Compares interior voxels of phase 1 (10), b) compares voxels of grains of phase 1 at grain boundaries with other grains of phase 1 (11), c) plots voxels of phase 1 at grain boundaries with phase 2 (12). Similar voxels of phase two are plotted alongside their phase 1 counterparts for comparison. d) Plots 20 voxels, e) plots 22 voxels and f) shows the 21 voxel comparison.*

deformation conditions as the two phase counterparts. Slip systems and relative CRSS values are chosen to be the same as in the two phase case, see Table 3.2.

Inverse pole figures of the compression direction are calculated for the single phase bridgmanite (Figure 3.9a) and the single phase periclase (Figure 3.9b) simulations. The bridgmanite phase shows a slightly sharper texture than when deformed in the two phase aggregate, as does the periclase single phase run. The periclase inverse pole figure shows a stronger $\{1\,1\,0\}$ texture than in the two phase simulations, in this case most of the slip activity is carried by the $\{1\,1\,0\}$ $\langle\bar{1}\,1\,0\rangle$ system that is selected to be the softest, but is not the most active in the two phase simulations. Then follows activity in the $\{1\,0\,0\}$¡011¿ system and the least active is the $\{1\,1\,1\}\langle 0\,1\,\bar{1}\rangle$. This is in agreement with experimental and numerical studies (e.g. Amodeo and Cordier, 2012; Carrez et al., 2009; Merkel et al., 2002),

Bridgmanite Single Phase Aggregate								
n	$(1\,0\,0)$	$(1\,0\,0)$	$(0\,1\,0)$	$(0\,1\,0)$	$(0\,0\,1)$	$(0\,0\,1)$	$(0\,0\,1)$	$\{1\,1\,1\}$
b	$[0\,1\,0]$	$\langle 0\,1\,1\rangle$	$[1\,0\,0]$	$\langle 1\,0\,1\rangle$	$[1\,0\,0]$	$[0\,1\,0]$	$\langle 1\,1\,0\rangle$	$\langle 0\,1\,\bar{1}\rangle$
CRSS	3	3	3	3	3	3	1.5	250
Slip Activity								
	0.113	0.128	0.113	0.117	0.034	0.029	0.435	0.031
Periclase Single Phase Aggregate								
n	$\{1\,1\,1\}$	$\{1\,1\,0\}$	$\{1\,0\,0\}$					
b	$\langle 0\,1\,\bar{1}\rangle$	$\langle \bar{1}\,1\,0\rangle$	$\langle 0\,1\,1\rangle$					
CRSS	1	0.5	1					
Slip Activity								
	0.265	0.420	0.315					

Table 3.2: *Slip systems, slip system CRSS values and activity are shown in this table for single phase simulations done using the random microstructure.*

that find the $\{1\,1\,0\}\langle\bar{1}\,1\,0\rangle$ to be the most active slip system, and that the $\{1\,1\,1\}\langle 0\,1\,\bar{1}\rangle$ is not active in periclase. The relative activities for the bridgmanite single phase simulation are comparable to those in the two phase simulations.

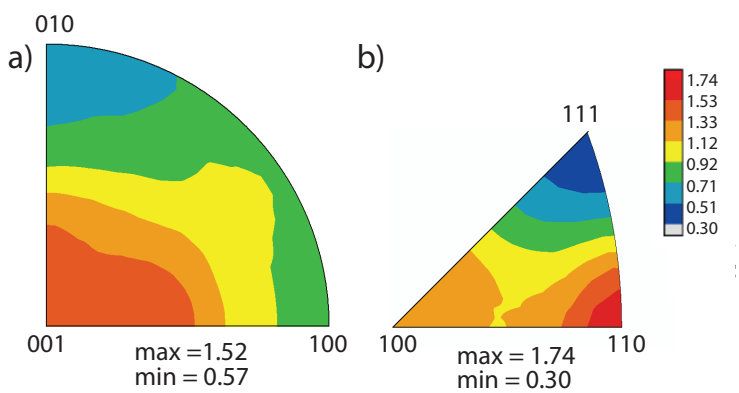

Figure 3.9: *Inverse pole figures (IPF) of the compression direction for a) single phase bridgmanite simulation using the random microstructure and b) single phase periclase simulation with the same random microstructure. Texture maximum is higher in the single phase simulations than in the two phase simulations, and the periclase single phase run develops the sharpest texture at 1.74 m.r.d., IPF's plotted using the same scale.*

Figure 3.10 displays probability density functions of the component of the strain tensor in the compression direction ($\dot{\epsilon}_{33}$) plotted for all voxels of the single phase bridgmanite run in magenta, the single phase periclase simulation in cyan and the two phase random microstructure run in purple. The single phase bridgmanite run presents very little difference with respect to the two phase case, and the single phase periclase simulation presents a very

sharp distribution, indicating a more homogenous deformation environment. Separating voxels into ones at grain boundaries(11 and 22) and at the interior of grains (10 and 20), a different behavior is observed in the PDF of the $\dot{\epsilon}_{33}$ values than what is observed in the two phase simulations (Figure 3.11. In these single phase simulations the voxels at the interior of grains and at grain boundaries deform statistically the same, as opposed to the two phase case where the voxels of phase 2 at grain boundaries have a more heterogenous distribution of the strain rate values in the compression direction. Furthermore, when the particular voxels of the single phase runs are compared to the two phase random microstructure case in Figure 3.12, it is found that both the grain boundary (11) and the interior (10) voxels (Figure 3.12a and b) have a wider distribution of $\dot{\epsilon}_{33}$ values in the single phase case than in the two phase simulation. Suggesting that the periclase phase absorbs enough deformation in the two phase case to result in less heterogenous deformation conditions of the bridgmanite phase.

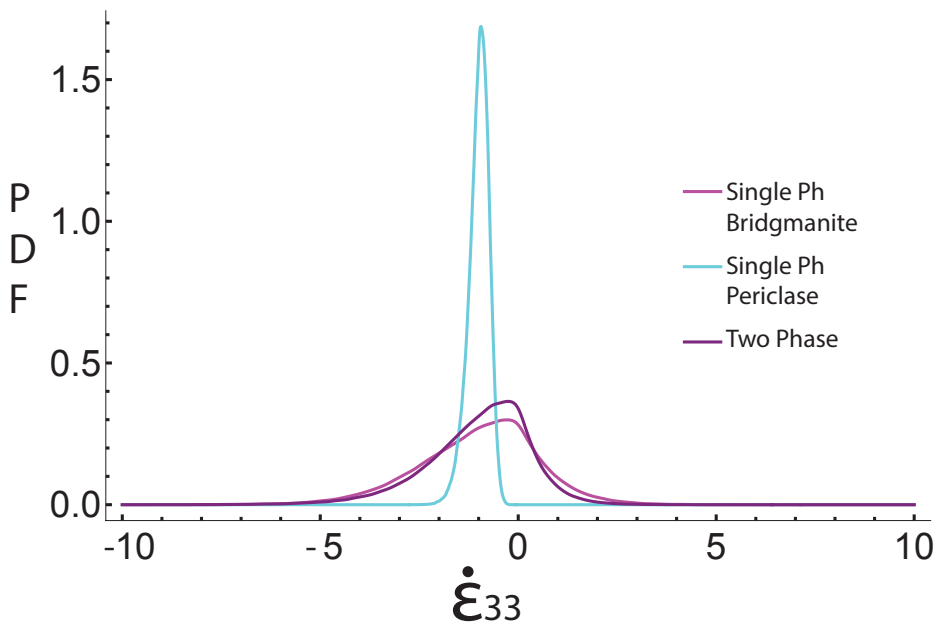

Figure 3.10: *Probability density functions of $\dot{\epsilon}_{33}$ for all voxels of the single phase bridgmanite run in magenta, single phase periclase run in cyan and two phase run in purple. Single phase simulations are done using the same random microstructure as the random microstructure in the two phase case.*

3.4 Discussion

Two phase simulation results for four different microstructures show that, except for the periclase microstructure, there is no microstructure dependence of the texture and the

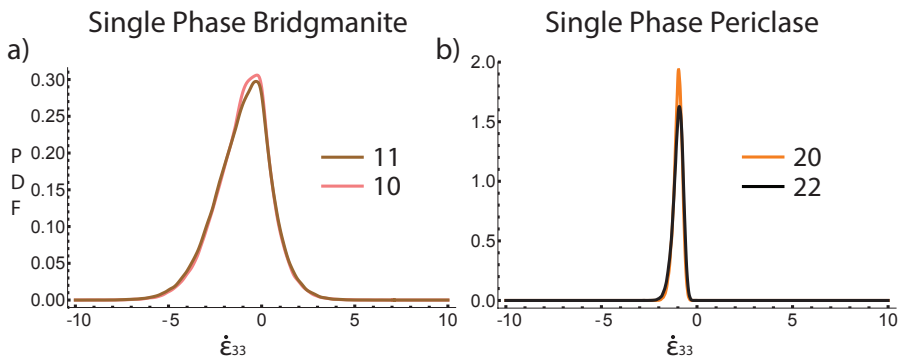

Figure 3.11: *PDF of the $\dot{\epsilon}_{33}$ values separated by grain boundary (11 and 22) and interior voxels for a) the single phase bridgmanite run and b) the single phase periclase run.*

slip system activity in these polycrystalline aggregates after 30% strain under compression (Figure 3.5 and Table 3.1). The large difference in texture of the percolate microstructure should be further investigated to make conclusive interpretations. Although it is possible that the low number of grains in this phase could make an artificially sharp texture, with respect to the other microstructures that have more grains of the bridgmanite phase, it is unclear whether that is the only explanation to this particularly textured aggregate. Probability density distributions of the $\dot{\sigma}_{33}$ component of the strain rate tensor plotted in Figure 3.7 show that, in the percolate microstructure, the voxels of phase 2 that are at grain boundaries have the same distribution as those same voxels for the other microstructures (Figure 3.7e and f). It also shows that it is the voxels of phase 1 that present a sharper distribution of $\dot{\sigma}_{33}$ values with respect to the other microstructures. It is important to point out that the there are less than 100 periclase grains in the percolate structure, but they present similar deformation conditions than the other microstructures. It develops a texture that is comparable to the other microstructures, supporting the notion that it is not only the small number of grains that are responsible for the sharp texture in the bridgmanite phase of this percolate microstructure, but that there is probably a microstructure dependance. It is possible that because the bridgmanite grains are not in contact with each other, they have lower stress at the grain boundaries that allows them to rotate more freely. This should be investigated further by doing a simulation with the percolate microstructure that has a larger number of grains.

Texture in the two phase simulations are in agreement with previous radial diamond anvil cell experiments that show a very weak texture development in bridgmanite when deformed together with periclase (Miyagi and Wenk, 2016; Kaercher et al., 2016). Single phase bridgmanite deformation experiments with radial diamond anvil cell done by Merkel et al. (2003) show no texture development, which is in agreement with the very weak texture observed in the single phase bridgmanite simulations. However, strong texture have been found in bridgmanite when deformed as a single phase and also in the two phase system

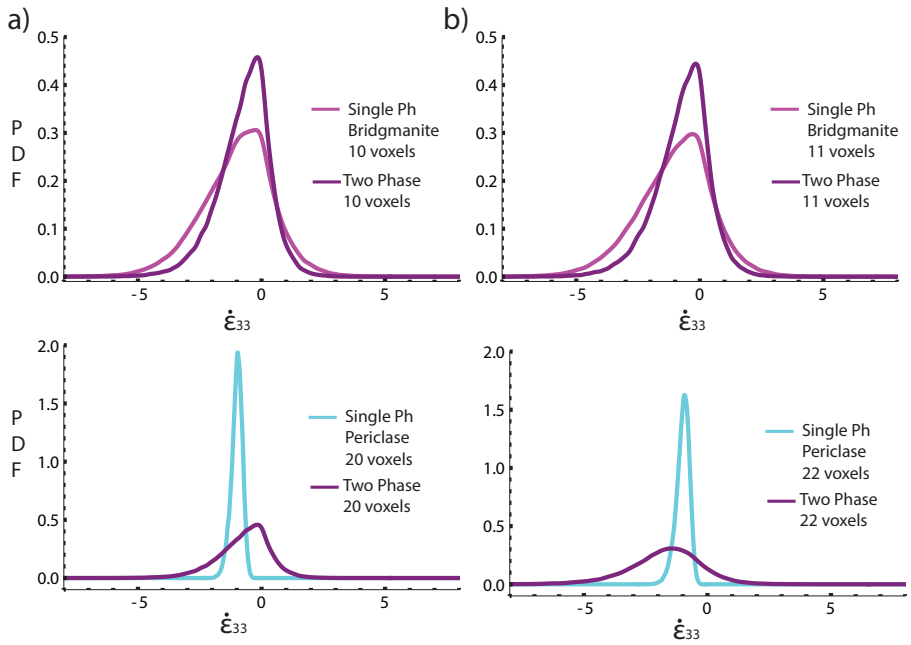

Figure 3.12: *Comparison of the PDF of the $\dot{\epsilon}_{33}$ values of the single phase runs with the two phase random microstructure run. PDF's are calculated for the different voxel types. a) Comparison of the 10 interior grain voxels of the single phase perovskite run with 10 voxels of the two phase random microstructure run, b) compares grain boundary voxels (11). c) Compares grain interior voxels (20) for the single phase periclase run with the two phase random microstructure 20 voxels and d) compares 22 grain boundary voxels.*

with periclase (Miyagi and Wenk, 2016; Wenk et al., 2006, 2004). A strong texture has also been observed in compression experiments on bridgmanite analogs (Kaercher et al., 2016). These discrepancies in the texture development of bridgmanite could be due to different microstructures that arise by using different starting materials, and/or orientation relationships with parent phases that affect subsequent texture development. It is also very likely that there are other plastic deformation mechanisms present in experiments, like grain boundary sliding, that are not taken into account in this model. Weak texture development in periclase when deformed together with bridgmanite is in agreement experimental results presented in Miyagi and Wenk (2016). Deformation experiments on bridgmanite/periclase analog materials also show a weak texture in the periclase analog material NaCl when deformed together with $NaMgF_3$, which is the bridgmanite analog (Kaercher et al., 2016). Shear deformation experiments find that periclase largely accommodates strain (Girard et al., 2016), this leads to a low stress that possibly does not reach the CRSS for slip to occur in periclase, thus little grain rotation is expected and a weak texture would develop, these findings are also in agreement with simulation results presented in this study. Single phase periclase deformation simulation results remain controversial. Radial diamond anvil cell

experiments up to 35GPa find a very strong texture in periclase when deformed as a single phase (Merkel et al., 2002), but a weak texture is observed in radial diamond anvil cell studies presented in Wenk et al. (2004).

Calculated probability density functions of the $\dot{\epsilon}_{33}$ component of the strain tensor also show that the core, random and triple junction microstructures have very similar deformation conditions (Figure 3.6), confirming the lack o microstructure dependence observed in the inverse pole figures of the compression direction (Figure 3.5). As a general trend across all four microstructures for the two phase simulations is the wider distribution of the $\dot{\epsilon}_{33}$ component in the voxels of phase 2 that are at grain boundaries (Figure 3.7. This implies that the softer periclase phase will largely accommodate deformation in certain regions of the aggregate. Lower stresses in the periclase phase make it hard to activate slip system activity in this phase, and explains the higher slip system activity found in the bridgmanite phase (Table 3.1). Furthermore, if $\dot{\epsilon}_{33}$ is separated into categories of voxels at grain boundaries or at the interior of grains (Figure 3.7), the distribution for the six different types of voxels is almost identical for the core, random and triple junction microstructures, showing that these microstructures behave similarly not only on a bulk average scale but on the local grain scale. The percolate microstructure presents a more narrow distribution of values of the $\dot{\epsilon}_{33}$ component (Figure 3.6), which is an indication of the accumulation of higher stresses that are more likely to activate slip systems, especially in the harder bridgmanite phase. It is the voxels of the bridgmanite phase that have the sharper distribution in the percolate case, with respect to the other microstructures as seen in Figure 3.7a and c. Voxels in phase two of the percolate microstructure have the same distribution as the other microstructures. This explains the sharper texture developed by the bridgmanite phase in this percolate structure.

Comparison of $\dot{\epsilon}_{33}$ distributions of grain boundary voxels and grain interior voxels for single phase simulations (Figure 3.11) with the two phase counterparts (Figure 3.7) exhibits that the larger strain rate distributions found in grain boundaries arise from the introduction of the second phase. It is deformation in the softer periclase phase that is most affected by this more heterogenous deformation environment introduced by having a two phase aggregate. Although some differences exist, deformation in the bridgmanite phase appears to have little susceptibility to the presence of the periclase phase at a 25% volume fraction. The relative slip system activity does not change significantly from the two phase simulations (Table 3.1) to the single phase simulations (Table 3.2), and the texture is also very similar (Figure 3.5 and Figure 3.9a). If the PDF of the $\dot{\epsilon}_{33}$ components for all voxels are compared between the two phase random microstructure and the single phase bridgmanite random microstructure simulations, it is found that they are very similar as well. However, the distribution of the 33 component of the strain rate tensor is sharper in the single phase case, for bridgmanite, than in the two phase case, suggesting that the presence of periclase, that largely accommodates the strain, promotes more homogeneous conditions for the harder bridgmanite phase than when it is deformed on its own. The periclase phase presents a considerably different behavior when deformed as a single phase. Although it develops a similarly weak texture in both cases (Figure 3.5 and Figure 3.9a), the maxima has a stronger

component in the $\{1\,1\,0\}$ planes and the relative slip system activity switches from the two phase to the single phase simulations (Table 3.1 and Table 3.2). Single periclase phase simulations present a very narrow distribution the $\dot{\epsilon}_{33}$ component of the strain rate tensor, indicating a more homogeneous deformation environment than in the two phase case where the periclase phase, in particular at grain boundaries, presents the widest distribution of $\dot{\epsilon}_{33}$ of the two phases.

Pole figures of a few selected grains are plotted to aid in the interpretation of simulation results presented in this study (Figure 3.13). The 100 poles of all the voxels for the selected grains are plotted for the two phase random microstructure simulation in Figure 3.13a, the single bridgmanite phase random microstructure simulation in Figure 3.13b, single periclase phase random microstructure simulation in Figure 3.13c, the compression direction is in the center of the pole figures. To elucidate the contrasting results of the percolate two phase simulation, four grains were also selected for this run and 100 pole figures shown in Figure 3.13d. In the two phase simulation shown in Figure 3.13a, grain number 220 (top row) is a grain of the bridgmanite phase that is mostly surrounded by periclase grains, and grain 179 is mostly surrounded by grains of the same bridgmanite phase. For the periclase phase, grain 882 is consecutive to grain 220 of perovskite and grain 1359 is mostly surrounded by other periclase grains. A few general trends stand out, there are large dispersions of the orientation of the 100 poles of the voxels of a single grain, in particular of the bridgmanite phase in both the two phase random simulation (Figure 3.13a) and the single phase bridgmanite simulation (Figure 3.13b). This large spread in orientation can explain the lack of texture found in bridgmanite since, by the stress field plots in Figure 3.4, high enough stresses are expected to accumulate in this phase to activate slip. The periclase phase has a more variable behavior. In the two phase random microstructure simulation, grain 882 that is consecutive to bridgmanite phase grain shows a large spread in the 100 poles of the voxels that compose the grain, but as you move to grain 1359, that is mostly surrounded by grains of the same phase, there is considerably less spread in the orientation of the 100 poles of the voxels of the grain. This is in agreement with what is found in the plotted strain rate distributions, where voxels of phase 2 at grain boundaries deform more heterogeneously than when the periclase phase is deformed as a single phase. It is also observed, by comparing Figure 3.13a and Figure 3.13b, that the response of the bridgmanite phase does not change considerably from the two phase case to the single phase case, in agreement with what is exhibited in Figure 3.10. The single phase periclase simulation shows a small spread in the 100 poles of the voxels of the four selected grains, which is in agreement with the narrow distribution of the strain rate values shown in Figure 3.10. In the two phase percolate microstructure simulation shown in Figure 3.10, 35 is a grain of the bridgmanite phase and is consecutive to grain 60 of the periclase phase, similarly bridgmanite grain 41 is consecutive to periclase grain 125. In this case the periclase grains develop very large dispersion of the 100 poles and the perovskite grains develop a comparable spread to the other simulations.

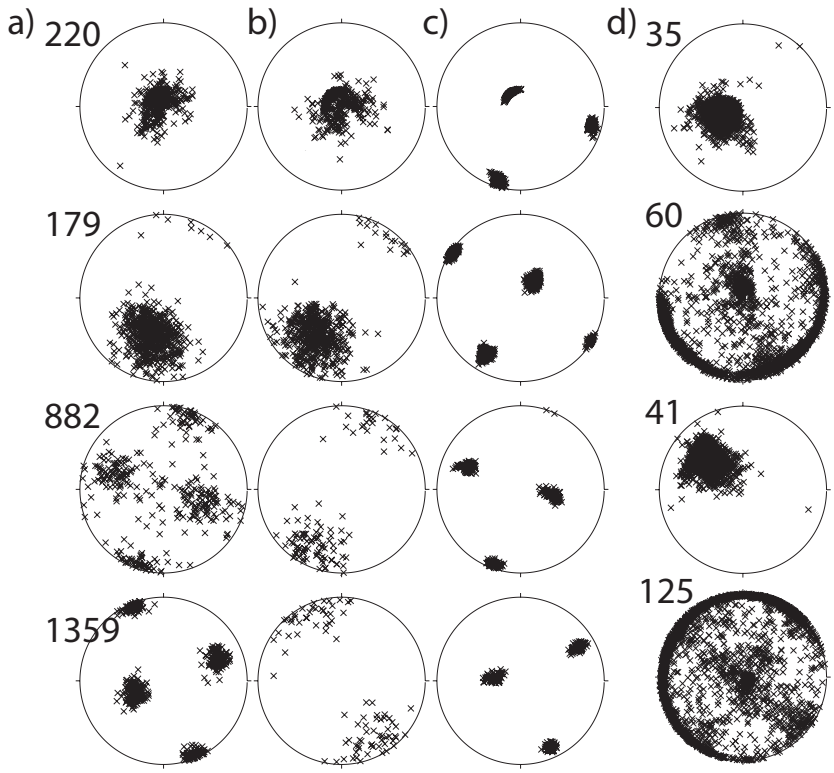

Figure 3.13: *100 pole figures for the voxels of selected grains in the a) two phase random microstructure run, b) single phase bridgmanite run, c) single phase periclase run and d) the two phase percolate microstructure run. Grain 220 and 882 are consecutive grains in the random microstructure. In the two phase simulation shown in a) grain 220 is mostly surrounded by grains of the periclase phase, grain 179 is mostly surrounded by grains of the bridgmanite phase, grain 882 is consecutive to grain 220 and grain 1359 is mostly surrounded by grains of the periclase phase. In c) grain 35 of the bridgmanite phase is consecutive to grain 60 of the percolate phase, and bridgmanite grain 41 is consecutive to periclase grain 125. Grain orientations selected using script presented in Appendix B.*

3.5 Conclusion

Plastic deformation due to dislocation glide in 75% bridgmanite + 25% periclase two phase aggregates has been studied using the VPFFT code. This system is selected due to its relevance to understanding plastic deformation in the lower mantle of the Earth. A suite of four different microstructures have been systematically studied to explore the influence of microstructure in texture development due to slip in these polycrystalline aggregates. It is found that, for this case study, texture development has no microstructure dependance when random, core and triple junction microstructures are considered, and it is found to

have a large microstructure dependence for a percolate microstructure. Slip system activity follows the same trend, it is the same for the random, core, triple junction and percolate microstructures, and suffers a switch in the most active slip system for the single phase periclase simulations using the random microstructure. In general, the periclase phase accumulates low stresses and is possibly the reason for the weak texture development, due to very little activation of slip systems in this phase. The weak texture in bridgmanite can be attributed to large intra granular misorientation due to the highly anisotropic single crystal yield surface of this low symmetry phase, but further investigation of misorientation distributions are needed. It is found that deformation of the periclase phase changes drastically when deformed as a single phase or in a two phase scenario as the minority phase. When it is deformed with bridgmanite, regions at grain boundaries of grains of the periclase phase develop a largely heterogenous distribution of the strain rate compared to regions in the interior of grains of the periclase phase and to grains of the bridgmanite phase. Good agreement is found with other simulation and experimental efforts in the two phase simulation presented in this study, but single phase simulations remain unclear. A study where a larger variety of microstructures is suggested, in particular to understand the role of grain boundaries in grain rotations in VPFFT. It is possible that are more physically realistic grain boundary scenario must be implemented to allow grains to rotate more freely and model single phase deformation behavior more accurately.

References

Ahrens, J., Geveci, B., and Law, C. (2005). Paraview: An end-user tool for large data visualization, visualization handbook. Elsevier. ISBN-13: 978-0123875822.

Amodeo, J. and Cordier, P. (2012). Modeling the effect of the pressure on the critical shear stress of MgO single crystals. *Philosophical Magazine*, 92:1523–1541.

Barton, N. R. and Dawson, P. R. (2001). On the spatial arrangement of lattice orientations in hot-rolled multiphase titanium. *Modeling Simulation in Materials Science and Engineering*, 9:433–463.

Brechet, Y. and Dawson, P. (1996). Effects of interactions among crystals on the inhomogeneous deformations of polycrystals. *Acta Materialia*, 44:1937–1953.

Canova, G., Wenk, H.-R., and Molinari, A. (1992). Deformation modeling of multi-phase polycrystals: Case of a quartz-mica aggregate. *Acta Metallurgica et Materialia*, 40:1519–1530.

Carrez, P., Ferre, D., and Cordier, P. (2009). Peierls-nabarro modeling of dislocations in MgO form ambient pressure to 100GPa. *Modeling and Simulation in Materials Science and Engineering*, 17:035010.

Chen, L., Chen, J., Lebensohn, R., Ji, Y., Heo, T., Bhattacharyya, S., Chang, K., Mathaudhu, S., Liu, Z., and Chen, L.-Q. (2015). An integrated fast fourier transform-based phase-field and crystal plasticity approach to model recrystallization of three dimensional polycrystals. *Computer methods in applied mechanics and engineering*, 285:829–848.

Childs, H., Brugger, E., Whitlock, B., Meredith, J., Ahern, S., Pugmire, D., Biagas, K., Miller, M., Harrison, C., Weber, G. H., Krishnan, H., Fogal, T., Sanderson, A., Garth, C., Bethel, E. W., Camp, D., Rübel, O., Durant, M., Favre, J. M., and Navrátil, P. (2012). VisIt: An End-User Tool For Visualizing and Analyzing Very Large Data. In *High Performance Visualization–Enabling Extreme-Scale Scientific Insight*, pages 357–372.

Cordier, P. (2002). Dislocations and slip systems of mantle minerals. *In: Karato S.I., Wenk H.-R. (eds) Plastic deformation of minerals and rocks. Mineralogical Society of America*, 2:137–179.

Cordier, P., Amodeo, J., and Carrez, P. (2012). Modeling the rheology of MgO under earth's mantle pressure, temperature and strain rates. *Nature*, 481:177–180.

Dawson, P., Needleman, A., and Suresh, S. (1994). Issues in the finite element modeling of polyphase plasticity. *Materials Science and Engineering A*, 175:43–48.

Dey, S., Suwas, S., Fundenberger, J.-J., and Ray, R. (2009). Evolution of crystallographic texture and microstructure in the orthorhombic phase of a two-phase alloy Ti-22Al-25Nb. *Intermetallics*, 17:622–633.

Girard, J., Amulele, G., Farla, R., Mohiuddin, A., and Karato, S.-i. (2016). Shear deformation of bridgmanite and magnesiowustite aggregates at lower mantle conditions. *Science*, 351:144–147.

Gottstein, G., Ma, Y., and Shvindlerman, L. (2005). Triple junction motion and grain microstructure evolution. *Acta Materialia*, 53:1535–1544.

Gouriet, K., Carrez, P., and Cordier, P. (2014). Modeling [100] and [010] screw dislocations in $MgSiO_3$ perovskite based on peierls-nabarro-galerkin model. *Materials Science and Engineering*, 22:025020.

Kaercher, P., Miyagi, L., Kanitpanyacharoen, W., Zepeda-Alarcon, E., Wang, Y., Parkinson, D., Lebensohn, R., De Carlo, F., and Wenk, H.-R. (2016). Two phase deformation of lower mantle mineral analogs. *Earth and Planetary Science Letters*, 456:134–145.

Kasemer, M., Quey, R., and Dawson, P. (2017). The influence of mechanical constraints introduced by β annealed microstructures on the yield strength and ductility of Ti-6Al-4V. *Journal of the Mechanics and Physics of Solids*, 103:179–198.

Kumar, S., Kurtz, S., and Agarwala, V. (1996). Micro-stress distribution within polycrystalline aggregate. *Acta Mechanica*, 114:203–216.

Lebensohn, R. (2001). N-site modeling of a 3d viscoplastic polycrystal using fast Fourier transform. *Acta Materialia*, 49:2723–2737.

Lebensohn, R. and Tome, C. (1993). A self-consistent anisotropic approach for the simulation of plastic deformation and texture development of polycrystals: application to zirconium alloys. *Acta Metallurgica Materialia*, 41:2611–2624.

Lebensohn, R. and Tome, C. (1994). A self-consistent viscoplastic model: prediction of rolling textures of anisotropic polycrystals. *Materials Science and Engineering A*, 175:71–82.

Lebensohn, R., Turner, P., Signorelli, J., Canova, G., and Tome, C. (1998). Calculations of intragranular stresses based on a large-strain viscoplastic self-consistent polycrystal model. *Modeling and Simulation in Materials Science and Engineering*, 6:447–465.

Mello, A., Nicolas, A., Lebensohn, R., and Sangid, M. (2016). Effect of microstructure on strain localization in a 7050 aluminum alloy: Comparison of experiments and modeling for various textures. *Materials Science and Engineering A*, 661:187–197.

Merkel, S., Wenk, H.-R., Badro, J., Montagnac, G., Gillet, P., Mao, H.-k., and Hemley, R. (2003). Deformation of $(Mg_{0.9},Fe_{0.1})SiO_3$ perovskite aggregates up to 32GPa. *Earth and Planetary Science Letters*, 209:351–360.

Merkel, S., Wenk, H.-R., Shu, J., Shen, G., Gillet, P., Mao, H.-k., and Hemley, R. (2002). Deformation of polycrystalline MgO at pressures of the lower mantle. *Journal of Geophysical Research*, 107:3–1–3–17.

Miyagi, L. and Wenk, H.-R. (2016). Texture development and slip systems in bridgmanite and bridgmanite + ferropericlase aggregates. *Physics and Chemistry of Minerals*, 43:597–613.

Miyajima, N., Yagi, T., and Ichihara, M. (2009). Dislocation microstructures of $MgSiO_3$ perovskite at a high pressure and temperature condition. *Physics of the Earth and Planetary Interiors*, 174:153–158.

Moulinec, H. and Suquet, P. (1998). A numerical method for computing the overall response of nonlinear composites with complex microstructure. *Computer Methods in applied mechanics and engineering*, 157:69–94.

Quey, R., Driver, J., and Dawson, P. (2015). Intra-grain orientation distributions in hot-deformed aluminium: Orientation dependence and relation to deformation mechanisms. *Journal of the Mechanics and Physics of Solids*, 84:506–527.

Roatta, A., Turner, P., Bertinetti, M., and Bolmaro, R. (1997). An iterative approach to mechanical properties of MMCs at the onset of plastic deformation. *Materials Science and Engineering A*, 229:203–218.

Tullis, J. and Wenk, H.-R. (1994). Effect of muscovite on the strength and lattice preferred orientation of experimentally deformed quartz aggregates. *Materials Science and Engineering A*, 175:209–220.

Upadhyay, M., Capolungo, L., Taupin, V., Fressengeas, C., and Lebensohn, R. (2016a). A higher order elasto-viscoplastic model using fast fourier transforms: Effects of lattice curvatures on mechanical response of nanocrystalline metals. *International Journal of Plasticity*, 83:126–152.

Upadhyay, M., Van Petegem, S., Panzner, T., Lebensohn, R., and Van Swygenhoven, H. (2016b). Study of lattice strain evolution during biaxial deformation of stainless steel using a finite element and fast fourier transform based multi-scale approach. *Acta Materialia*, 118:28–43.

Vigano, N., Tanguy, A., Hallais, S., Dimanov, A., Bornert, M., Batenburg, K., and Ludwig, W. (2016). Three-dimensional full-field x-ray orientation microscopy. *Scientific Reports*, 6:20618.

Wang, Y., Hilairet, N., Nishiyama, N., Yahata, N., Tsuchiya, T., Morard, G., and Fiquet, G. (2013). High-pressure, high-temperature deformation of $CaGeO_3$(perovskite) $\pm$ MgO aggregates: Implications for multiphase rheology of the lower mantle. *Geochemistry Geophysics Geosystems*, 14:3389–3408.

Wenk, H.-R., Lonardelli, I., Merkel, S., Miyagi, L., Pehl, J., Speziale, S., and Tommaseo, C. (2006). Deformation textures produced in diamond anvil experiments, analyzed in radial diffraction geometry. *Journal of Physics: Condensed Matter*, 18:S933–S947.

Wenk, H.-R., Lonardelli, I., Pehl, J., Devine, J., Prakapenka, V., Shen, G., and Mao, H.-K. (2004). In situ observation of texture development in olivine, ringwoodite, magnesiowustite and silicate perovskite at high pressure. *Earth and Planetary Science Letters*, 226:507–519.

Wenk, H.-R., Matthies, S., Donovan, J., and Chateigner, D. (1998). Beartex: a windows-based program system for quantitative texture analysis. *Journal of Applied Crystallography*, 31:262–269.

Zhang, B., Nagasekhar, A., Sivarupan, T., and Caceres, C. (2013). Deformation behavior of the percolating intermetallic microstructure of high pressure die cast az91 alloy. *Advanced Engineering Materials*, 15:1059–1067.

Zhao, Y. and Tryon, R. (2004). Automatic 3-D simulation and micro-stress distribution of polycrystalline metallic materials. *Computer methods in applied mechanics and engineering*, 193:3919–3934.

Chapter 4

Multigrain Crystallography

4.1 Introduction

The physical and mechanical properties of polycrystalline materials are largely governed by their structure. Polycrystalline materials in the Earth undergo significant deformation due to its dynamic nature. Hence, a complete understanding of structural evolution during deformation is of utmost importance. The different length scales at which these processes occur makes structural dynamics hard to make comprehensive models. In general, most modeling and experimental characterization efforts describe the atomic and the macroscopic scales best, using molecular dynamics and atomic scale probes, and using continuum mechanics and macroscopic scale loading apparatus combined with imaging techniques, respectively. The description at the mesoscale is typically phenomenological, where the effects of local heterogeneities are not well understood. In addition, microstructures of polycrystals in the Earth and a great number of engineering applications are three dimensional, and in a number of cases, three dimensional results have shown that two dimensional characterization might be incomplete (Schmidt et al., 2004). A widely used three dimensional characterization technique is the focused ion beam (FIB) in a scanning electron microscope (SEM) (Volkert and Minor, 2007). The FIB has access to length scales from a few nanometers to hundreds of micrometers, and has a wide variety of applications for surface characterization and 3D tomographic experiments (Uchic et al., 2007). Unfortunately this technique is not applicable to *in situ* studies of structural dynamics since it is a destructive technique. Furthermore, there are material compositions that are not accessible to the FIB due to charging problems with the electron beam (Volkert and Minor, 2007). High energy X-rays (typically in the 50-100 keV energy range) generated in synchrotron sources can penetrate deeply into materials, and provide a singular opportunity for nondestructive characterization of microstructures in three dimensions (Juul Jensen et al., 2006).

Due to the growing need for three dimensional characterization techniques and the highly destructive nature of electron based techniques, the 3D synchrotron X-ray diffraction

(3DXRD) technique has undergone a rapid growth. Advantages of the 3DXRD technique are the non destructive high penetration power at bulk and on a micron scale, it provides contrast between individual elements of the structure so they can be completely characterized with respect to their position, morphology, phase, crystallographic orientation and strain (both plastic and elastic). It has a probing volume large enough to be statistically representative of the bulk of the material, and can provide the adequate time resolution for *in situ* deformation studies (Poulsen, 2004).

Texture models are typically tested at a macroscopic scale, where the underlying structural dynamics at the grain and subgrain level are unknown. Margulies et al. (2001) use the 3DXRD technique to study grain rotations at the grain and sub grain level in tensile deformation of pure aluminum. They find that observed grain rotations are inconsistent with the classical Taylor (Taylor, 1938) and Sachs (Sachs, 1928) models. Poulsen et al. (2003) measure average lattice rotation of individual grains, and orientation spread *in situ* during 6% elongation of aluminum. They conclude that rotation paths have a strong dependence on initial orientation but that the influence of grain interaction is relatively small when grains deform plastically. Furthermore, Winther et al. (2004) track lattice rotations of 95 individual grains, and analyzed correlations between initial orientation and rotation behavior. They find that the Taylor model predicts overall rotations reasonably well in some regions, but they find large discrepancies for certain texture components. They also compare self consistent models and they find that they predict large variations in some texture components but they fail to predict rotation directions. More recent studies couple 3DXRD measurements with synthetic diffraction patterns that are projected on a virtual polycrystal deformed using a finite element framework (Obstalecki et al., 2014). They track four grains using this high energy diffraction technique and they find that significant spatial heterogeneity of orientation, stress and plastic strain rate distributions are necessary in the model to explain measured results. Another publication from this author couples 3DXRD experiments with crystal plasticity modeling to understand orientation spread in grains as a function slip system activity (Oddershede et al., 2015). In the study they conclude that variations in the relative slip system activities explain the different measured rotation paths, and that variations in the relative activity of the systems with highest Schmidt factors are responsible for most of the orientation within the tracked grains.

For studies of minerals of the Earth's interior, it is of interest to apply the 3DXRD method to high pressure synchrotron X-ray experiments. Due to limitations in rotation angle that are inherent to the diamond anvil cell, a polychromatic beam approach was initially suggested. Scanning the sample in energy as opposed to spatially rotating enables ultra fast data collection and provides the ability to collect diffraction data without rotating the sample (Ice et al., 2005). The more traditional 3DXRD technique, where the sample is rotated, has been used to track grains in a $MgGe_3$ post-perovskite polycrystalline sample plastically deformed in a diamond anvil cell, where they determined their orientation, positions and strain tensors (Nisr et al., 2012). The study then performs an X-ray profile analysis to characterize dislocations in the crystal structure of grains, and determine the most probable

active slips systems. Their findings are consistent with seismic anisotropy observations in the D" region of the Earth's mantle. It has been shown by deforming SiO_2 stishovite samples that the 3DXRD technique is suitable for diamond anvil cell experiments with heterogeneous grain sizes (Nisr et al., 2014) and to perform *in situ* monitoring of phase transformation microstructures (Rosa et al., 2015, 2016). First principles calculations and high pressure experiments using the 3DXRD technique have identified a pyrite structured iron oxide FeO_2 at 76 GPa and 1800 Kelvin (Hu et al., 2016). The authors of this study show that the mineral goethite decomposes to FeO_2 releasing H_2 in the deep lower mantle and predict that it could create FeO_2 patches that can provide an alternative interpretation to seismic and geochemical anomalies.

In the following chapter an application of the 3DXRD technique to high pressure diamond anvil cell deformation experiments is presented. In particular that of the multigrain approach implemented in the software HEXRD (Bernier et al., 2011). The software HEXRD addresses the problem of a polycrystalline volume illuminated with x-ray radiation, the volume averaged lattice orientations, lattice strain tensors and center of mass coordinates can be determined, and if the single crystal elastic moduli are known the mean stress tensors can be calculated from the full lattice strain tensors obtained from the diffraction data. The software was developed from a close collaboration with the Advanced Photon Source and Lawrence Livermore National Laboratory (Hansen et al., 2010) and it has been applied to the study of slip system activity and strength evolution in deformed polycrystalline aggregates (Bernier et al., 2010; Pagan et al., 2017). First a brief explanation of the experimental setup and procedure of high pressure diamond anvil cell experiments on olivine Mg_2SiO_4 transformed to bridgmanite $MgSiO_3$ + periclase MgO performed at beamline 12.2.2 of the Advanced Light Source of Lawrence Berkeley National Laboratory is given. Then a description of the code is in order due to the lack of documentation of HEXRD, paying specific attention to the particular application in question. Preliminary results are presented and particular issues with the low orthorhombic symmetry of bridgmanite and the scarce amount of periclase, adding to the weak diffraction inherent to their low Z number are discussed.

4.2 Experimental Methods

The experimental procedure followed in this study is outlined. The application of the multigrain data and analysis technique to high pressure diamond anvil cell studies requires special considerations due to a reduced opening angle of the DAC, which limits the rotation range of the sample and the Bragg conditions that are satisfied. If texture studies are required, it is important to do an appropriate sample preparation to ensure that stress is transmitted to the sample, due to the lack of a hydrostatic pressure medium. Traditionally texture studies in the diamond anvil cell are done in the radial geometry, where the the X-ray beam is perpendicular to the uniaxial compression axis of the diamond anvils, so that Debye rings record a whole range of orientations (Wenk et al., 2006). In the case of the multigrain

technique samples are rotated with a rotation axis perpendicular to the beam, accessing a large range of orientations. Due to this particular data collection technique it is not necessary to add the extra complexity of performing experiments in the radial geometry. Experiments presented here were performed at beamline 12.2.2 of the Advanced Light Source (ALS) at Lawrence Berkeley National Laboratory. A detailed explanation of the sample preparation and experimental parameters and procedure is presented in the following sections.

Considerations for Sample Preparation

A few considerations for sample preparation suited for the multigrain data acquisition technique will be presented in this section. In the case where differential stress is desired in the diamond anvil cell(DAC) it is important to ensure that there is enough confining pressure for the sample to be deformed. The goal in the multigrain data acquisition technique is to obtain sharp diffraction spots from a collection of grains (from one to about a couple thousand), this often implies that the grains are fairly large compared to the size of the sample chamber, and it is common to have a spaces in the chamber that are not filled with sample which will result in a poor stress state of the sample grains, leading to very slow pressure increases, low differential stress and potentially no grain rotations leading to poor texture development. This will also make phase transformations hard to achieve.

When a collection of a few grains up to the couple thousands is desired to use in the experiment, it is recommended to use a boron epoxy gasket (Merkel and Yagi, 2005). The sample chamber must be filled and packed as much as possible manually but with large grains it is inevitable for void spaces to remain, as the DAC is closed the boron epoxy gasket becomes soft and will close into the sample removing most of the void spaces in the sample chamber and packing it tighter than what can be achieved manually. If a single crystal is desired for the experiment, the optimum sample preparation would be one where the single crystal can be the size of the sample chamber to ensure that stress can be transmitted to the sample. If this is not possible, it is recommended to use a pressure medium that solidifies at low pressures, so it provides a matrix in which the stress can be transmitted to the sample. This would also be the recommendation if a metal gasket is wished to be used.

If there is a need to laser heat the sample to induce a phase transformation or for high temperature studies, it is important to consider the sample composition to ensure coupling with the laser. If the sample contains very light elements exclusively, and particularly if the sample is transparent, it is highly likely that the sample will not couple with the laser and the use of platinum black powder (a very fine grained black platinum powder with hight purity) mixed in the sample. Caution must be taken when adding platinum powder so the sample signal is not overpowered by the stronger diffracting platinum and buried in the noise. Fortunately platinum black has a very small grain size and has a weak diffraction signal, but it can still be overpowering when using very light samples like SiO_2, especially when doing powder diffraction. The multigrain data acquisition technique is forgiving in terms of the amount of platinum that can be used since the diffraction spots from large sample grains

have a considerably high intensity. A rule of thumb is that if a coarse powder is being used, mix platinum black powder until the sample looks grain by eye. If larger grains are used these can be rolled in the platinum black powder and loaded into the sample chamber with what gets stuck on their surface. In this case it is also recommendable to load one or two clusters of pure platinum black powder grains. It is important to point out that platinum black is not a very good pressure calibrant. It has a very wide diffraction peaks due to its poor crystallinity.

Experimental Parameters

Coarse grained olivine crystals selected from a peridotite from Hawaii were carefully placed into a 80μm sample chamber of a boron epoxy gasket. Boron epoxy gaskets where prepared following the procedure presented in Merkel and Yagi (2005) and sample chambers were drilled using the laser drilling machine at the sample preparation lab of beamline 1.2.2 of the ALS (Figure 4.1.

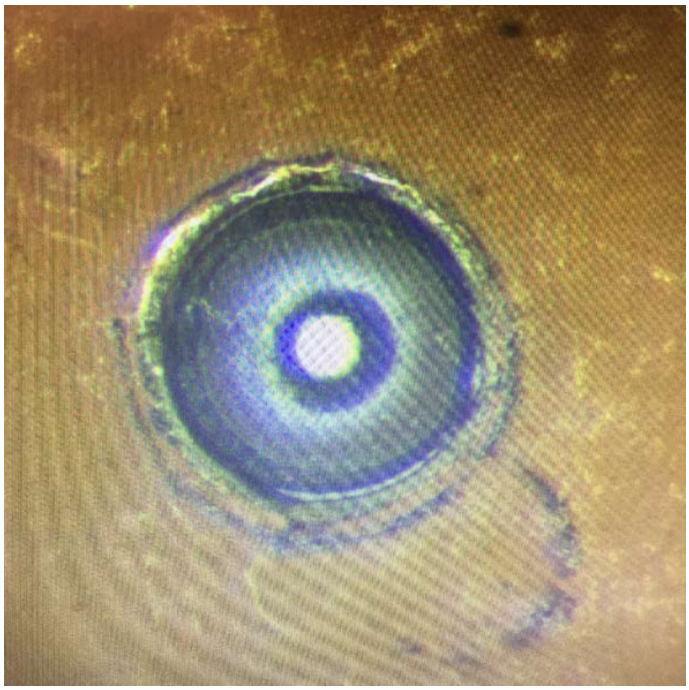

Figure 4.1: *Boron epoxy gasket (dark brown) with empty sample chamber drilled with Oxford Scientific laser mill in the sample preparation room of beamline 12.2.2 at the ALS. Surrounding orange material is kapton, used as a sleeve for easier manipulation of the gasket (Merkel and Yagi, 2005).*

The gasket was positioned on 300μm flat culet diamonds that are glued with epoxy to cubic boron nitride (BN) backing plates and aligned perfectly parallel to each other in a

BX90 diamond anvil cell (Kantor et al., 2012). Figure 4.2 shows diamonds glued to backing plates with black epoxy (Lakeshore cryogenics Stycast epoxy), and mounted on the BX90 diamond anvil cell. The cell is closed using screws with belleville washers to provide a spring force.

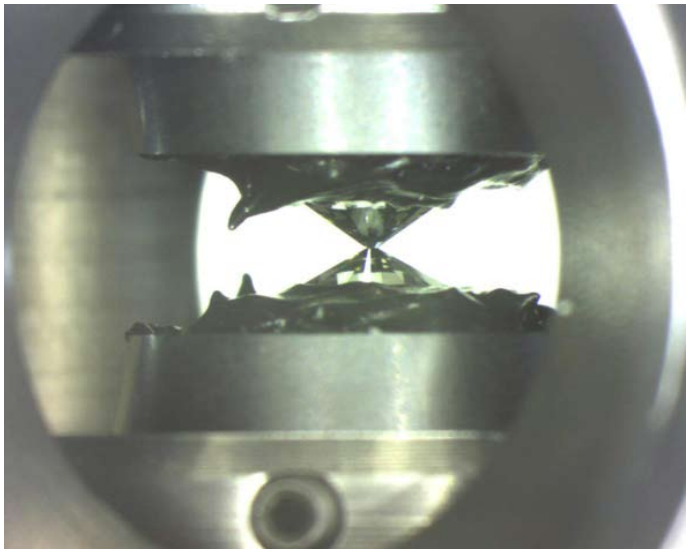

Figure 4.2: *300 μm culet diamonds glued with Stycast epoxy (black) to boron nitride plates and mounted onto a BX90. Picture is looking through the radial opening of the cell.*

Letoullec et al. (1988) developed a system where the DAC is compressed by a metal membrane inflated by a gas. This membrane system enables a finer control on pressure increments in the diamond anvil cell, and is a great device to use in experiments that are largely sensitive to the sample to detector position. In addition, the pressure can be controlled form outside the experimental X-ray hutch and saves precious time for measurements. It is of great advantage to use this membrane system when boron epoxy gaskets are used, especially with low Z materials, since it is a poor X-ray absorber and presents little absorption contrast with the sample. This makes sample centering difficult, and sometimes impossible if a very low energy (10KeV) or other optical methods are not used. Unfortunately the use of this membrane system reduces the accessible angular range, and subsequent problems for data analysis.

I this experiment a pressure membrane system designed by beamline 12.2.2 staff engineer Andrew Doran was used, and the pressure controlled from outside the hutch by a GE Druck pressure control unit. The system was mounted on a series of stages that can translate in the X, Y and Z directions, and also rotate around an axis perpendicular to the X-ray beam. The Perkin Elmer CMOS 2D X-ray detector was used for its fast data acquisition capabilities, with a 75μm pixel size and 200 x 200 pixel 2D dimensions. A picture of the BX90 cell, in

the pressure membrane can connected to the Druck pressure control unit (not in picture), mounted on the kinematic stages and the Perkin Elmer detector is shown in Figure 4.3.

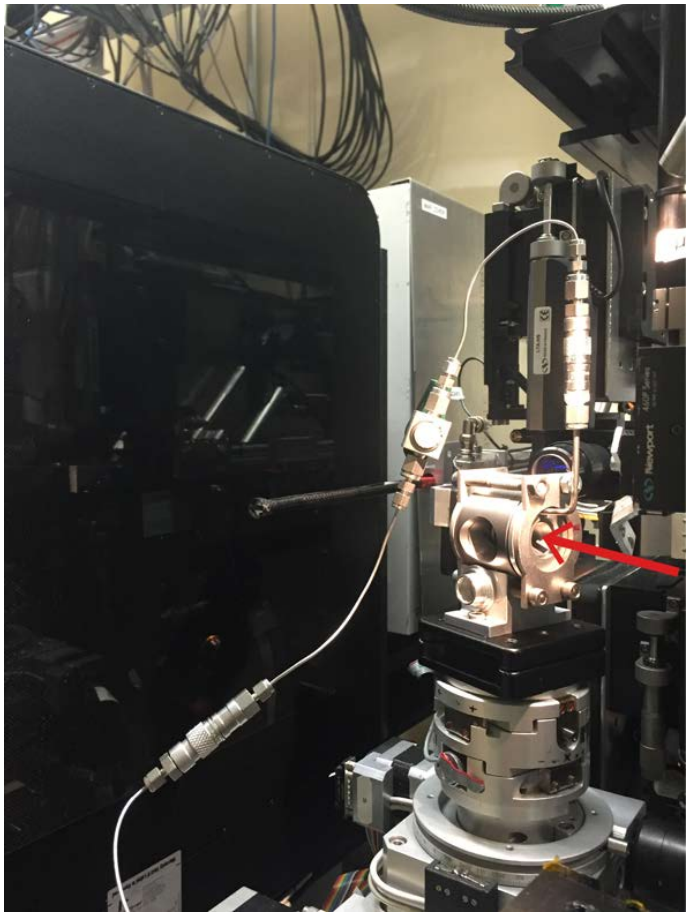

Figure 4.3: *Picture of BX90 DAC inside pressure membrane can, mounted on kinematic stages in beamline 12.2.2 of the ALS. Red arrow indicates*

Data Collection

The two most important steps for a successful experiment is to take a good calibration, and to carefully align both the calibrants and the sample to the axis of rotation of the stage they are mounted in. X-rays are focused into this point, and all the calibration parameters will be with respect to this position. For the multigrain analysis technique it is important to calibrate the detector with both a CeO_2 powder diffraction pattern, to calibrate in 2D, and with a single crystal ruby sphere standard to calibrate in 3D. The single crystal ruby sphere calibration is also used to determine whether the selected analysis parameters are correct, in particular the flip mode. Once the CeO_2 pattern is taken, an initial calibration can be

done in HEXRD, it is recommended to do this at the beamline to detect any problems at an early stage of the experiment. The user must input a good initial guess of the sample to detector distance and the X,Y center of the diffraction pattern. The initial guess can be refined by selecting *show rings* in the Graphic canvas section of the gui, changing the parameters in the detector tab and overlapping the calculated rings with the data. Once a good initial guess is obtained a fit can be ran using the first five HKL's. After convergence of the first refinement a second one can be done using all the available rings in the diffraction image. A larger number of azimuthal bins can be selected in this second iteration to achieve a more refined calibration. Single crystal ruby spheres (SRM 1990) have been certified by the National Institute of Science and Technology (NIST) as a Standard Reference Material for single crystal diffractometer alignment (Wong-Ng et al., 2001). For the multigrain analysis approach it is important to take the largest angular range possible, and to use the same step size as will be used for the samples of interest. The ruby sphere is aligned to the center of rotation by viewing it optically with a CCD camera (Figure 4.4), rotating it in different directions, and adjusting sample X and sample Z until it shows no precession. For a reference to the beamline coordinates see Figure 4.6.

After taking a CeO_2 pattern for an initial calibration of the detector, a ruby single crystal sphere rotation series is taken to use as a standard for checking that analysis parameters are correct. It is important in this step that the diffraction image is not saturated for a proper analysis of the ruby single crystal (see Figure 4.5), and a full 360 degree rotation series should be take if possible.

Data was collected between an angular range of -22 to 22 degrees in omega, see Figure 4.6. Each frame was taken at every 0.25 degree steps, and is the sum of 4 exposures of 0.5 seconds each. It is recommended to take short exposures and take the sum of them to avoid saturation in the Perkin Elmer Detector. Beamline 12.2.2 counts with automated data collection routines where the sample is rotated and exposures of the detector are synchronized.

HEXRD expects that the first position in the data array corresponds to the intensity of the first pixel in the top left corner of the detector if seen from the direction where the X-rays are propagating. For proper data analysis it is crucial to know if the images are rotated or any if any other operation is applied to them in the post processing or even the raw output of the detector. This is what is named the *flip mode* in HEXRD. Typically there is a shadow casted by the beamstop used to block the direct incident X-rays from saturating the detector; since the position of the beamstop with respect to the detector is known, the shadow recorded in the diffraction image can be used to determine the *flip mode* (Figure 4.6).

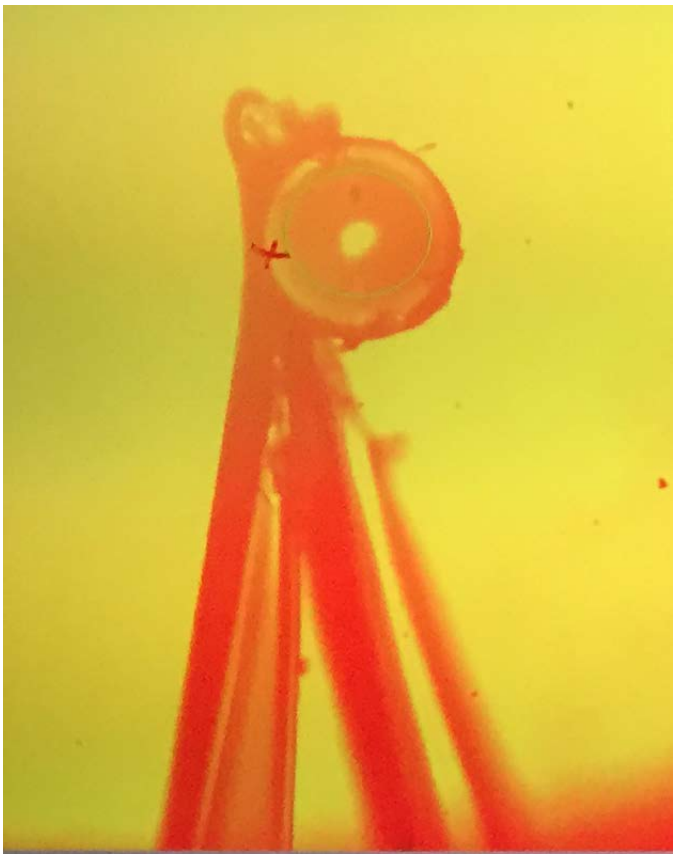

Figure 4.4: *Image of ruby single crystal sphere that is glued onto a needle point and mounted on a kinematic mount.*

4.3 The HEXRD Multigrain Analysis Software

With HEXRD it is possible to index diffraction spots and find the different grains that these originate from. It performs a detector calibration with either a powder standard or a single crystal standard, or both if available. After the detector is properly calibrated, the diffraction spots of a single crystal or multiple single crystals sample can be indexed according to the appropriate material information and the calibration parameters. Once the diffraction image is indexed, HEXRD can find the different grains that are in the beam path by looking for clusters in orientation space.

To collect data that is suitable for analysis with the HEXRD software, it is necessary to rotate the sample in an axis perpendicular to the beam and take diffraction patterns in small angle steps of about 0.25 degrees. This procedure is what we will call a rotation series hence forth. It is also very important to have a good calibration of the instrument parameters, for this it is recommended to take both a diffraction image of a powder calibration standard like CeO_2 and of a single crystal standard as well, single crystal ruby being a very common choice.

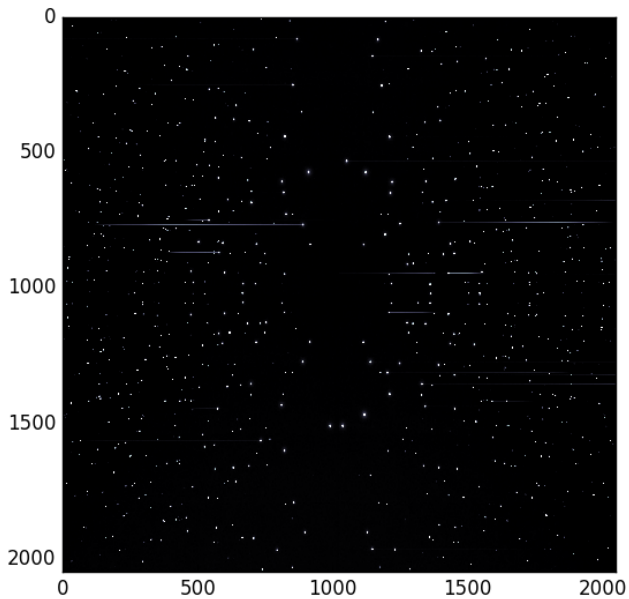

Figure 4.5: *Maximum intensity of all the frames of the rotation series taken on the ruby single crystal sphere NIST standard. Lines indicate saturated spots that should be avoided.*

While for the powder pattern it is not necessary to take a rotation series of the sample, it is necessary in the case of the single crystal calibration standard and it is recommended to make the same angle steps and exposure than what you are using for your sample. It is possible to perform an analysis with only one of the calibration standards, the powder pattern provides a good first guess and with the single crystal standard rotation series you can achieve a more detailed analysis and refine distortion parameters.

In order to go through the analysis procedure you will use a combination of: 1) a graphical user interface where you can perform a detector calibration with a powder pattern, load single image and rotation series, and create a materials and detector configuration file, 2) a .yml configuration file for indexing and finding grains, and 3) command line arguments that open the gui, and run indexing and grain finding routines.

A very straight forward installation procedure can be done if Anaconda python is installed. After this package is obtained, HEXRD can be installed by typing the following command in a terminal window:

```
conda install hexrd=0.3 -c joelvbernier
```

Once the program is installed, type HEXRD in the command line, a list of positional arguments and optional arguments should display in the console like shown in Figure 4.7.

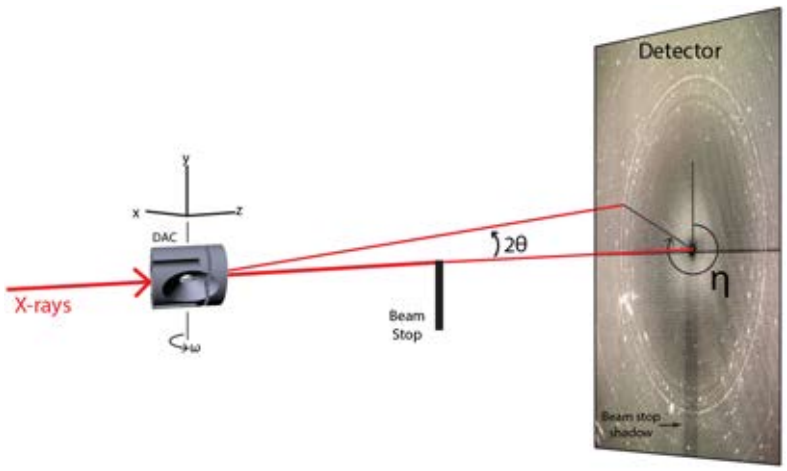

Figure 4.6: *Experimental layout at beamline 12.2.2 of the ALS. Synchrotron X-rays are focused in the rotation axis of ω, and sample is also aligned in z to this rotation axis. As X-rays diffract on the crystal structure they form a diffraction cone with a 2θ angle that is particular to each HKL. The sample is rotated in ω to satisfy a larger number of brag conditions for each grain in the illuminated volume. The angle η is the azimuth angle on the plane of the detector. A beamstop is used to protect the detector from the direct incident beam. It is also useful to determine the* flip mode *in the data.*

You will mainly use the positional arguments to either open the gui typing `gui`, indexing of diffractions spots with `find-orientations` and finding grains using the `fit-grains` argument. Use the `cache-frames` positional argument to cache frames for faster access.

```
eloisas-mbp:Hexrd_Manual Loet$ hexrd
usage: hexrd [-h] [-V] [--debug] [--inst-profile INST_PROFILE] command ...

High energy diffraction data analysis

positional arguments:
  command
    help                Displays a list of available conda commands and their
                        help strings.
    documentation       Launches the hexrd documentation in a web browser
    gui                 Launches the hexrd graphical user interface
    find-orientations   Process diffraction data to find grain orientations
    fit-grains          Extracts G vectors, grain position and strain
    cache-frames        Caches detector frames in npz format
    test                runs the hexrd test suite

optional arguments:
  -h, --help            show this help message and exit
  -V, --version         show program's version number and exit
  --debug               verbose reporting
  --inst-profile INST_PROFILE
                        use the following files as source for functions to
                        instrument
```

Figure 4.7: *Options to the command HEXRD. Positional arguments are used to open gui, and perform indexing and grain fit routines. Run the 'test' positional argument to test installation and cache frames to save cache in npz format.*

The first step is to calibrate the instrument parameters like sample to detector distance, xy center, tilt and distortion parameters. For this it is necessary to open the gui, load the calibration material information, together with the wavelength of your experiment, load powder image and perform fit to powder pattern to refine detector parameters using the gui. Once your detector is calibrated you can index single crystal or multigrain patterns and run the find grain routine. For indexing and finding grains you must prepare a .yml file that will be described in Section 4.3, and write the .yml file name as positional arguments of the `find-orientations` and `fit-grains` commands in your terminal.

The GUI

Open the gui by typing in your terminal the following command:

```
hexrd gui
```

Python will open an interactive graphical user interface (gui) like shown in Figure 4.8. The gui has two general sections, the left half has multiple tabs where the materials information is inputed, image files are loaded and detector calibration is performed, and on the right half there is the visualization panel where loaded image files are displayed.

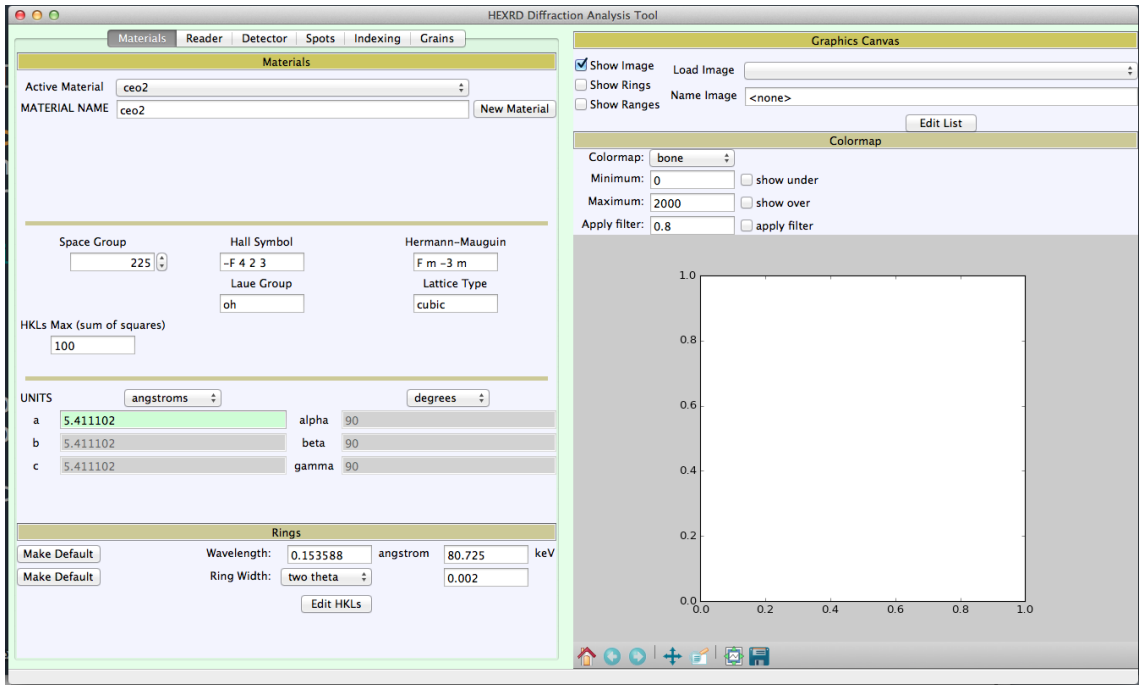

Figure 4.8: *Graphical user interface window opened by typing the command* **`hexrd gui`** *in your terminal. On the left half we have tabs where your sample and data collection information can be inputed, and diffraction images loaded. On the right half there is the visualization panel where diffraction images are visualized live on your screen.*

Materials

In this tab you will input your material information. There are a few calibrants that are commonly used pre loaded. You can also create a new material by assigning a new name, space group and lattice parameters. It is important in this tab to input the wavelength of your particular experiment. Refer to Figure 4.9 in this section.

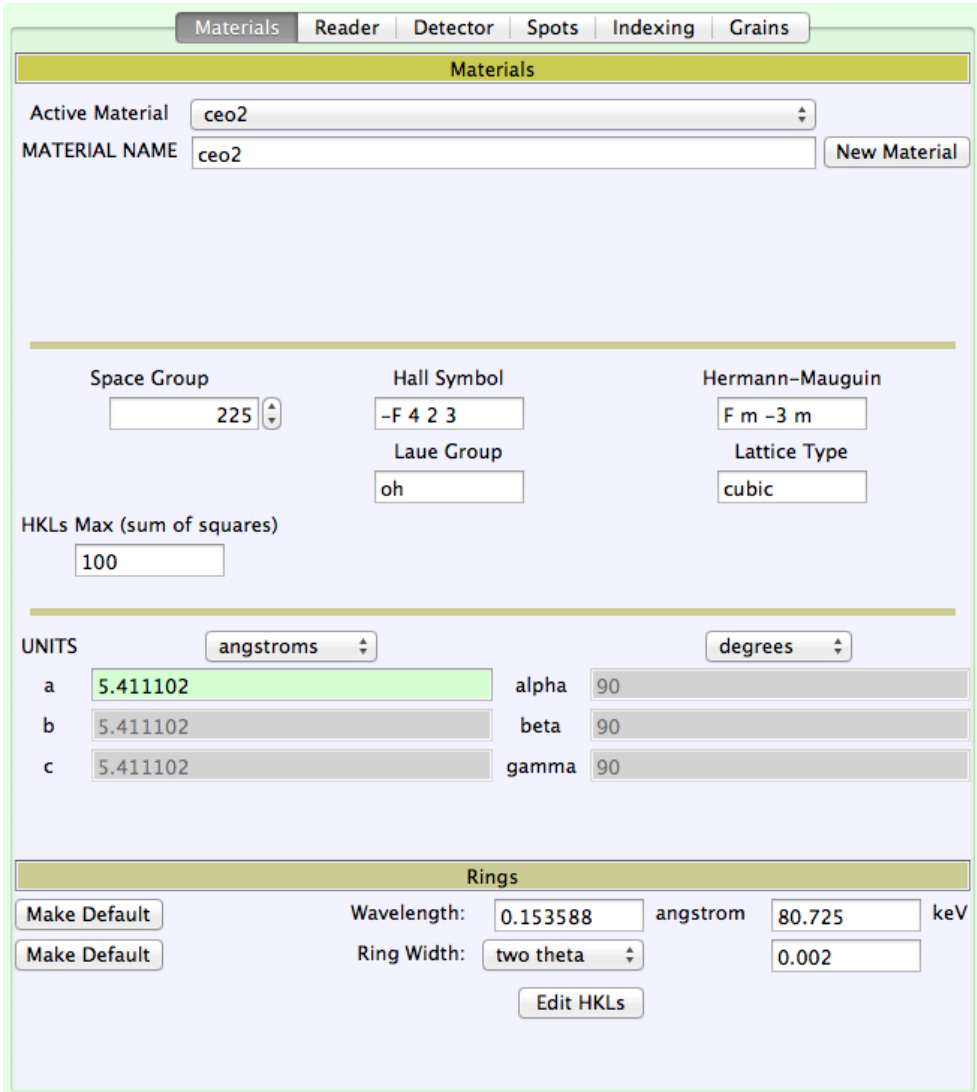

Figure 4.9: *Graphical window opened by typing the command* `hexrd gui` *in your terminal. On the left half we have tabs where your sample and data collection information can be inputed, and diffraction images loaded. On the right half there is the visualization window where diffraction images are visualized live on your screen.*

Materials

Active Material Drop down menu with some pre loaded materials that are commonly used. Select one if your material is in the list. You can make a new material in the next box if your material is not in the drop down menu.

MATERIAL NAME You can create a new material by first clicking on the *New Material* button and then changing the name in the text box. You must press enter in this text box for the change to take effect. It is important to point out that you must click the New Material button before typing your materials name, if you fail to do so the current material selected in *Active Material* will be renamed.

Space Group If you have selected a pre loaded material from the *Active Material* drop down menu the space group will be automatically updated. When creating a new material you must select the appropriate space group by using the up and down arrows, you can type in your space group number but you must toggle the arrows for the changes to take effect. The *Hall Symbol*, *Herman-Maugin*, *Laue Group* and *Lattice Type* are updated automatically when the space group is selected.

HKLs Max (sum of squares) This is related to how many HKL crystallographic planes can be used in the analysis. For a high symmetry material 100 is enough. For a lower symmetry material with an orthorhombic lattice a sum of squares of 200 is more suitable.

UNITS Angstroms and degrees are the only available units for input of crystallographic parameters.

a, b, c, alpha, beta, gamma If the material you have used is not in the *Active Material* drop down menu you will have to input the particular crystallographic parameters a, b and c of your material. The angles alpha, beta and gamma are automatically updated when the space group is selected. You must press after typing crystallographic parameters for changes to take effect.

Rings

Wavelength, angstrom The wavelength used in your experiment is different for the particular beamline and synchrotron that is used, it is important to make sure that you input the correct wavelength in this section. Input wavelength in angstroms or energy in KeV, press enter so changes take effect (if you input a wavelength it will calculate energy and vice versa).

Ring Width Plus minus tolerance, in two theta or strain, of the position of the diffraction ring.

Edit HKLs Click here to open HKL list. HKL's in white will be used in calculations and shown in the *Colormap* visualization panel, shaded HKL's are not used or shown. You can modify the list by highlighting desired HKL's and clicking **OK**. You must click **OK** for changes to take effect of **Cancel**. Especially for lower than cubic symmetry materials, it is important to check the structure of your particular material to select the best HKL's to use in the refinement, the ones with higher multiplicity are best. Every time the list of HKL's is changed you must save the materials.cpl file to record changes.

Saving Materials list Once you have finished inputing all your materials information, you can save your material by selecting the *Materials* menu in your main python toolbar, and selecting *Save material list*. Save the materials list with a .cpl extension since it is a cpickle file.

Reader

The reader tab is for reading diffraction image frames, dark image, set proper image orientation and define rotation angle range and step. You can also choose to browse frame by frame in the visualization panel or add all frames into one image. It is possible to have multiple readers, i.e. data sets, loaded at the same time. Refer to Figure 4.10 in this section.

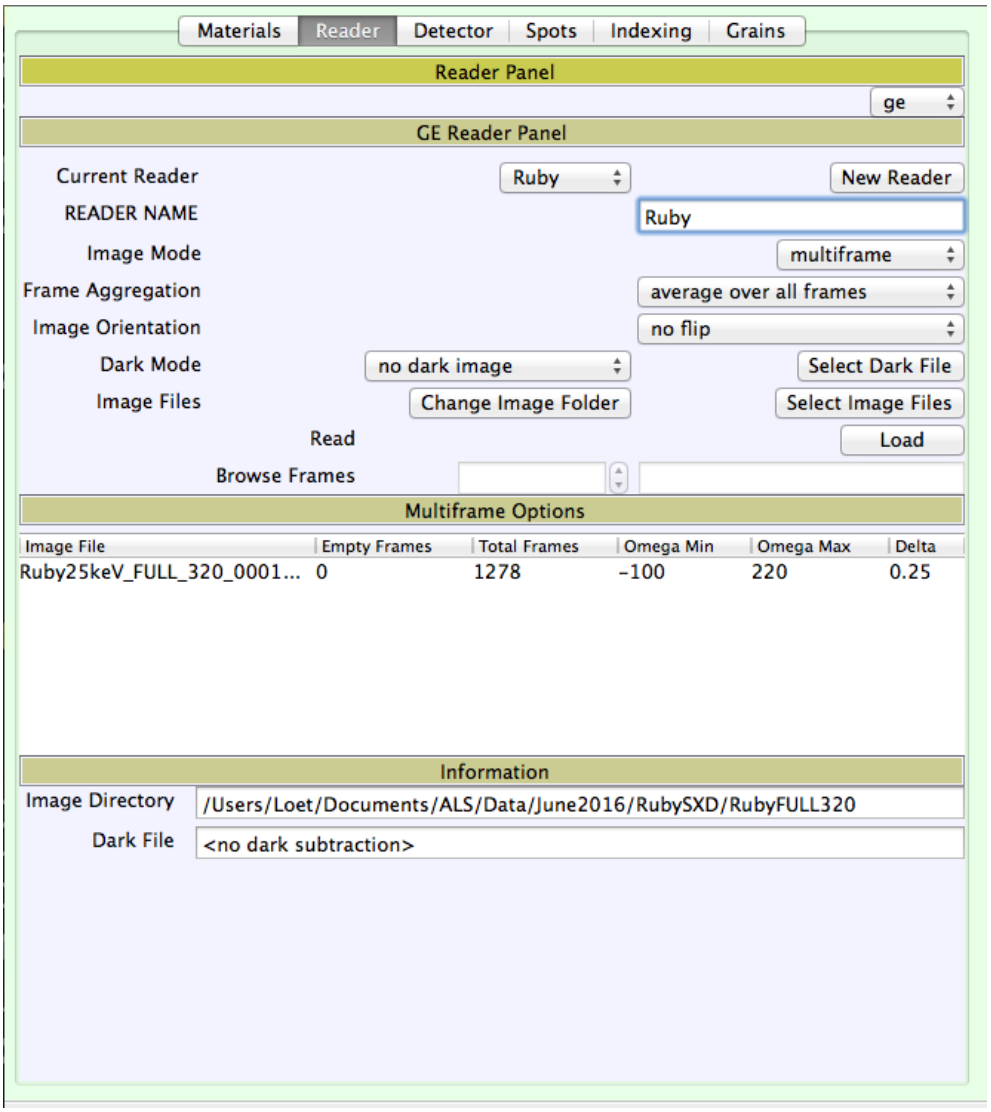

Figure 4.10: *Reader tab.*

Reader panel Select input file type selected from drop down menu.The .ge file is the only file type that is currently supported.

GE Reader Panel

Current Reader Drop down menu shows the list of readers, i.e. loaded datasets. Click *New Reader* if you would like to load a new dataset, if you do not create a new reader, the information you input in the following sections will overwrite what ever the current reader has. If you are starting a new analysis there will be a default empty reader named *reader*.

READER NAME Select name for your new reader and press enter for changes to take effect.

Image Mode Select single frame or multiframe depending on the type of your data. If you have taken a single diffraction image of a powder pattern you will select *single frame* form the drop down menu, select *multiframe* if you have a rotation series with multiple images in a particular angular range and steps. In the .ge file type you have multiple frames in one single file, so you will select the *multiframe* option from the drop down menu so the rotation series information can be inputted in the following sections.

Frame Aggregation Provides different options for viewing loaded frames in visualization panel. Frames can be viewed as *SINGLE FRAMES*, where each frame is shown individually and you can scroll through each image, if you only have one frame this would be the option to select. The *average over all frames* option provides a single image with the average value at every pixel, and the *max/min over all frames* provides a single image with either the maximum or minimum intensity at each pixel. In the *multiframe* case it is recommended to use the *max over all frames* since it is useful for setting a good background threshold and for identifying saturated diffraction spots that may hinder the analysis process.

Image Orientation If your detector or pre processing software introduces rotations to your images, you must select the proper rotation to bring your image back to "detector" coordinates. Hexrd anticipates that the top right corner of your image corresponds to the top right corner of the detector if you are looking at it from the photons perspective, i.e. looking at the front of the detector. The known position of a beamstop in your experiment is usually a good indicator of what rotation you have, since there is usually a shadow of the beamstop casted on the images. If this needs to be figured out, load your image and look for your beamstop or any kind of marker, select the rotation you think is appropriate and click load again to see the changes. Lower maximum in Color Map section to see finer changes in intensity.

Dark Mode Load a dark image if you have one. There are cases where the dark image is already subtracted in the diffraction image.

Image Files Select file you wish to load by clicking on the *Select Image Files* button. You can load more than one file if you have taken images at different sample rotations, this is useful if you have taken rotation series at different angle ranges of a sample sample, or if you have taken more than one powder calibrant image at 180 degrees from each other to compensate for errors in rotation center position with respect to your sample. Select file and click load to see in the Color Map panel.

Read Click the *Load* button to read the selected image file.

Browse Frames This option is active only when the multiframe image mode is selected. The box on the right displays the total frames and on the left you may view each individual frame in the Colormap panel by using the up and down arrows.

Single Frame/Multiframe Options Depending on you selection in *Image Mode*, this panel will show information for your single frame or multiframe image(s) and you must input the rotation series angular range and steps information in the multiframe case. When making changes in this panel, you must hit the **TAB** button on your keyboard for changes to take effect.

Image File The image file name is automatically loaded when image file is selected in the GE Reader Panel.

Empty Frames Some experimental and data collection circumstances introduce empty frames at the beginning of each scan. If this is the case of your experiment input the number of empty frames here and press **TAB** for changes to take effect. This option appears in the multiframe image mode only.

Total Frames For the multiframe image mode, the number of total frames is automatically loaded here when the image file is selected.

Omega Min This is the starting angular position of the rotation series. The start omega is arbitrary but it is recommended to use the same one as your experiment for clarity. Input your omega min and press **TAB** for changes to take effect.

Omega Max Enter the ending angular position here and press **TAB**.

Delta Enter angle between each frame in your experiment and press **TAB**.

Information Displays diffraction and dark image directory path.

Image Directory Selected image directory path.

Dark File Dark image directory path.

Visualization Panel

Graphics Canvas Here you can select a few options for the Colormap panel that shows loaded images. The only functioning setting in this panel are the three check boxes that allow you to show loaded image, plot calculated diffraction rings according to material, wavelength and detector parameters, and shows two theta range for each HKL ring. Refer to Figure 4.11 in this section.

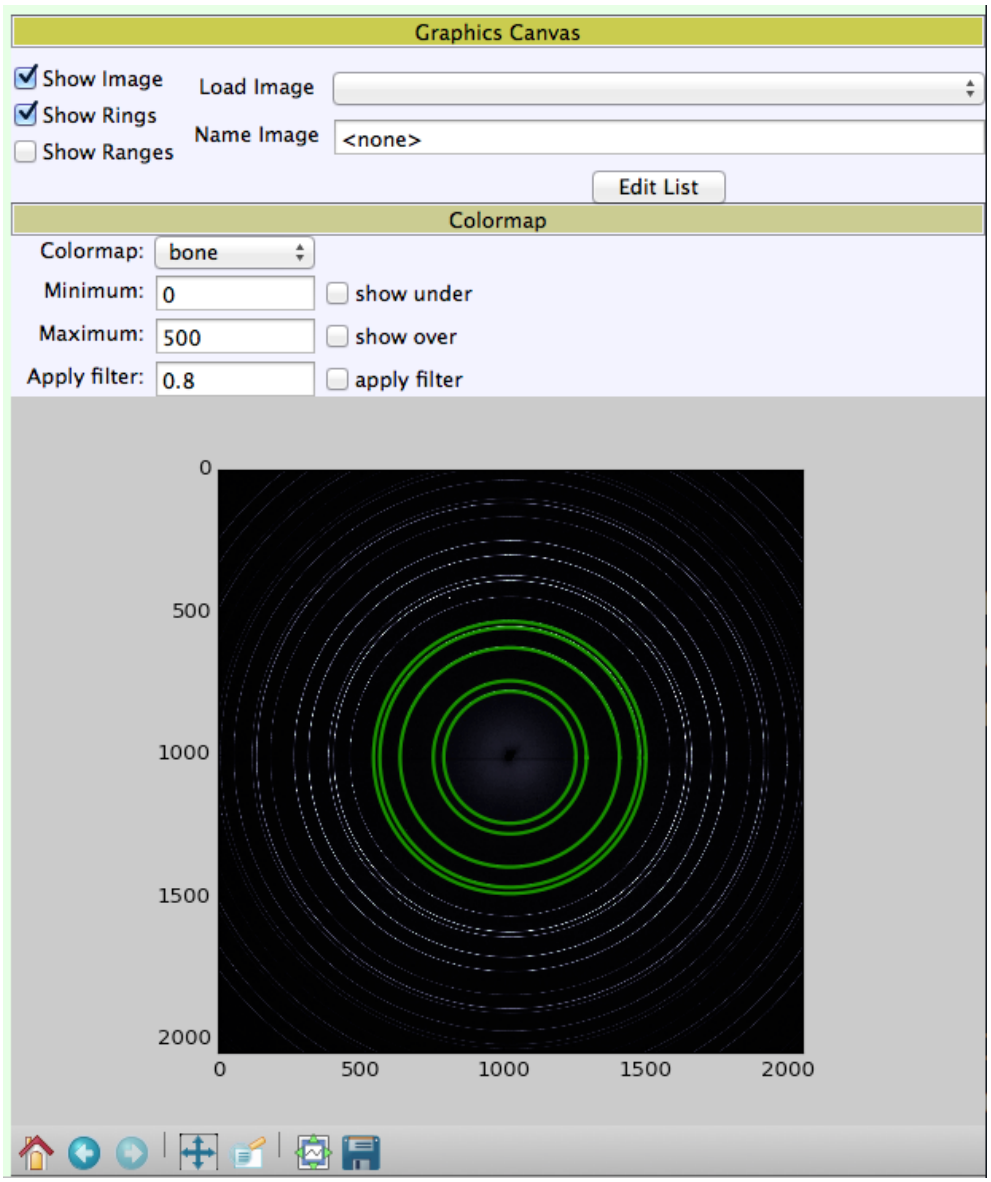

Figure 4.11: *Visualization panel.*

Show Image Toggle between showing or hiding image. Image must be loaded in the reader tab for image to show.

Show Rings Shows diffraction rings in green according to the particular material you have selected or created in the Materials tab, the image or multiple images you have loaded in the reader tab, and the detector parameters in the detector tab. If something looks odd when you *Show Rings*, check that your wavelength and correct material are selected.

Show Ranges By having this box checked the range in two theta (or strain) for each HKL ring is shown in the Colormap. The range is determined by the *Ring Width* option in the Materials tab. You can also change the range in the Detector tab by changing the *Ring Width* option.

Load Image Option unavailable a this time.

Name Image Option unavailable a this time.

Edit List Option unavailable a this time.

Colormap In this panel you can visualize the loaded diffraction images, change the colormap and maximum/minimum intensity, as well as apply filters. The toolbar on the bottom left of the panel enables you to zoom in and move the image around, as well as save the loaded image.

Colormap The drop down menu has 19 different color maps pre loaded. Select color map that better suits your data.

Minimum Sets the minimum threshold for pixel intensity. Note that when you scroll your mouse around the loaded diffraction image, the pixel values for that specific mouse location are shown in the bottom toolbar of the gui. To set a good minimum threshold it is recommended to scroll through the background with your mouse and take note of the values of intensity in a few pixel locations by reading the *int* value in the toolbar. The checkbox on the right of the minimum intensity is very useful for setting a minimum threshold, if you check the box `hexrd` will color in blue all the pixels that are under the minimum value, your aim is to select a value that provides a predominantly homogeneous background, i.e. everything you consider background in blue when the *show under* box is checked. You must press enter for changes to take effect when you change the minimum intensity value. The minimum threshold is very important for further calculations since it determines the difference between signal and noise.

Maximum Set threshold for maximum intensity at any pixel. It is useful to lower this value to see weak diffraction spots and to reduce the visual effects of saturated spots. You can check the *show over* box to check that you are not removing valuable data. This maximum threshold is only for the purpose of visualization and printing the image to file.

Apply filter I don't see what this does.

Home Click the home button to bring the displayed image to its original position, and un zoomed state.

Left right arrows Toggle between images when you have multiple frames loaded with the *SINGLE FRAMES* frame aggregation mode. Arrows will be shaded if there are no more images available.

Displace image Click to activate mode and then click and drag image to displace in viewing window. Press the home button to return to original position.

Zoom In Press button to activate mode and then click and drag rectangle on image to select region you wish to zoom in to. You may zoom in multiple times. Press the home button to return to original state.

Configure Subplots Opens a window where changes to configuration of plot region can be made. Change sliders on the variable you wish to change. Press reset to return to default settings. You can also press home button after closing the configure subplots window and the plot will return to default settings.

Save Press to save image to desired image format.

Detector

In this section an initial guess of detector parameters is done by the user by overlapping the calibrant powder rings or single crystal spots with calculated rings using detector parameters and materials data plotted in the Colormap. After initial guess is done the program can run a least squares fit of the detector parameters using the calibrant diffraction pattern. This is live with the Color Map section, when you make a changes in Detector Parameters for your initial guess, press enter so the changes are reflected in the Colormap. It is also possible to move things live with the arrow buttons. Refer to Figure 4.12 in this section.

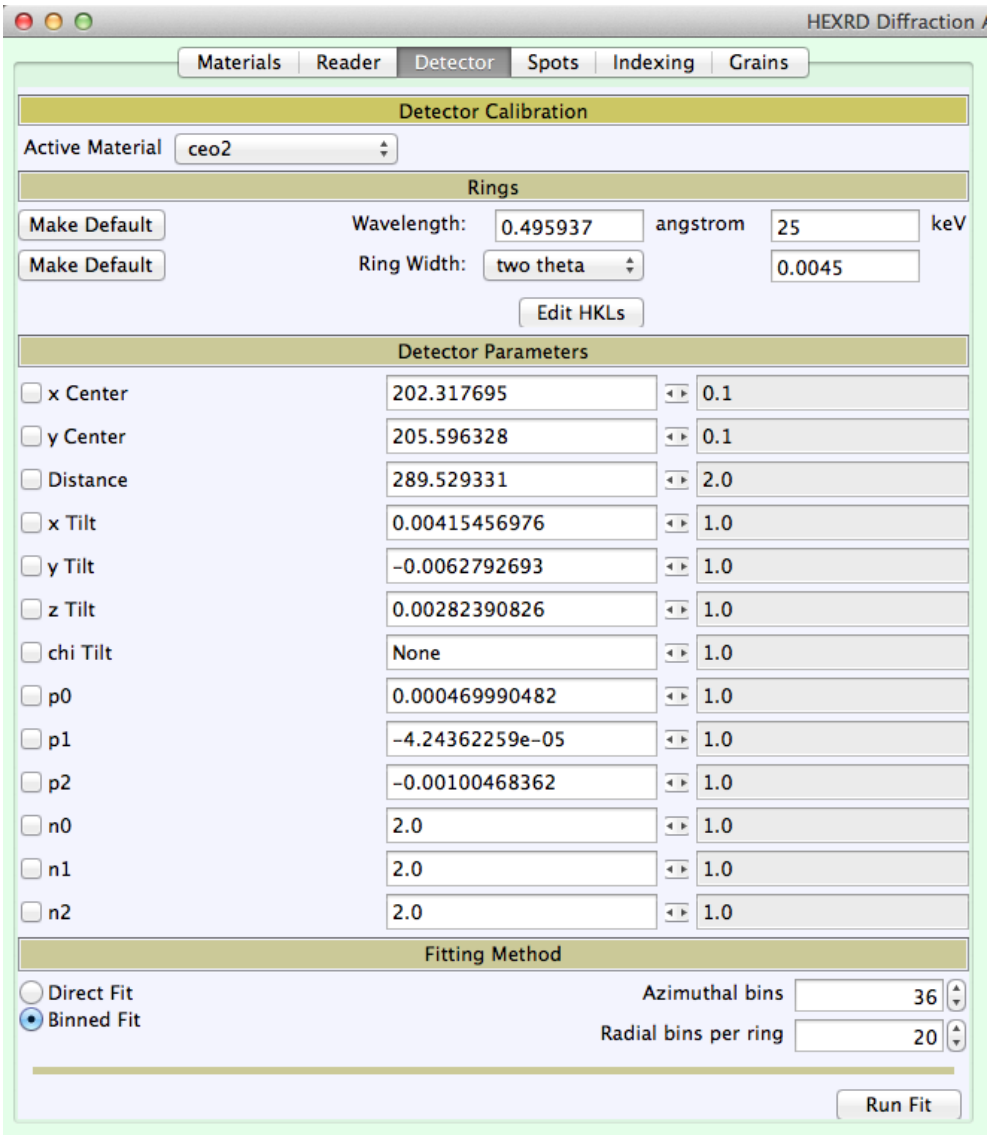

Figure 4.12: *Detector tab.*

Detector Calibration

Active Material Select active material that corresponds to your calibrant material.

Rings

Wavelength This value is read from the Materials tab but it is important to check it is correct. Either wavelength in Angstrom of energy in keV can be changed, press enter

for changes to take effect. It is possible to make a certain wavelength the default value by pressing the *Make Default* button.

Ring Width This is the range in which the intensity of the rings must be within. Units can be two theta or strain. A certain default range can be set by pressing the *Make Default* button.

Edit HKL's List of HKL's for material are shown. The HKL's that are not shaded will be the ones shown when the "Show Rings" box is checked and then ones used for the detector calibration when *Run Fit* is selected. If the list of HKL's is changed the materials.cpl file must be saved again to record changes.

Detector Parameters Check boxes on the left of parameter to refine. Numerical values are entered by selecting text box and hitting enter when value has been inputted by the user. Un and down arrows with custom step size may be used as well.

x , y Center Manually change so calculated rings in green are centered with the powder or single crystal calibrant diffraction pattern.

Distance Manually change so HKL's have correct 2theta angle and overlap with raw data.

x , y Tilt These parameters can be refined with a powder patter in the initial parameter fit from manually inputted detector parameters.

z Tilt This parameter cannot be refined with a powder pattern.

chi Tilt This can be read if the information exists from a different source. Cannot be refined with powder pattern.

p0, p1, p2 Distortion parameters. With the few rings used in an initial fit there is not much information to fit these parameters at that stage.

n0, n1, n2 Distortion parameters. Do not refine in initial fit.

Fitting Method Fit methods and resolution of the fit are selected here.

Direct Fit

Binned Fit Sums information in selected azimuthal bins. This method is good for generating initial guess. If resolution is increased, a good detector calibration can be achieved by this method.

Azimuthal bins Number of bins that the 360 azimuthal plane is divided in. Type value and press enter for changes to take effect.

Radial bins per ring

Run Fit Press button to run fit. Progress of fit can be tracked in the console as standard output.

Polar Rebinning

Polar rebinning is used to generate eta-omega maps that will be used for indexing diffraction spots in the data. It is a re-mapping of the data by plotting for each active HKL the intensity along the azimuth angle eta in the horizontal axis and the intensity along the omega channel which corresponds to the different frames taken in the rotation series in the vertical axis. Each pixel in the vertical axis corresponds to one angular step in the rotation series, and the pixel size in the eta horizontal axis corresponds to the pixel size of the detector. These maps are saved and used in the find-orientations routine. The polar rebinning routine is accessed through the python menu bar by clicking the Detector menu and selecting Polar Rebinning, a window will pop up like shown in Figure 4.13. Once the polar rebin button is clicked the maps are generated and saved after inspection and selecting a threshold.

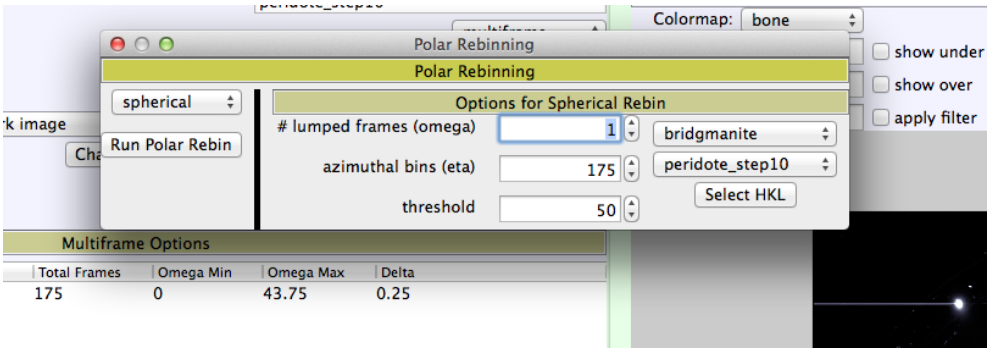

Figure 4.13: *Polar rebinning popup window. By clicking on the polar rebin button the eta-omega maps are generated..*

Options for Spherical Rebin

 # lumped frames (omega) This section is if it is needed to sum adjacent frames of the rotation series together. Typically this is not desired and the value is set to 1. Hit tab to enter values. (Joel: what would this do if you do lump frames?).

Azimuthal Bins (eta) The azimuthal bins on the eta channel are typically selected to be equal to the number of frames in the rotation series. Hit tab to enter values.

Threshold This is the threshold that is manually selected in the colormap section by using show under and ensuring a homogeneous background that does not remove data points. Hit tab to enter values.

Top right corner drop down menu Select active material.

Second drop down menu Select desired reader.

Select HKL button Active HKL's that will be plotted in the eta-omega space can be changed here. If they are not changed the values selected previously will be used.

Spherical Select spherical rebin.

Run Polar Rebin Press this button to create eta-omega plots given the selected parameters.

Rebin Canvas

Omega-Eta Plots

HKL drop down menu Select each HKL to examine plots and look for saturated spots. The find-orientation routine should be seeded with HKL's that have the least saturated spots.

Raw, Quick Render, Full Render Select data rendering type. Raw is the most common selection.

Export Press export button to save Eta-Omega plots. Select threshold value before exporting.

Label Spots Press to label calculated diffraction spots in Eta-Omega plots for each HKL.

Colormap

Colormap Select different colormap that better suits your data set.

Minimum Input a minimum value and press the show under check box to show pixels that fall under this minimum intensity in blue. It is important to select minimum intensity value that provides a smooth background and that does not remove any relevant intensities.

Maximum Change maximum to modify contrast and remove saturated spots to select an appropriate background intensity. Use show over check box if needed.

Filter Apply filter if a large amount of saturated spots exist?

The .yml File

This file is used in the `find-orientations` and the `fit-grains` routines in `hexrd` as a configuration file containing run information, the path to the raw data and calibration files, and parameters for indexing and finding grains. An example of a .yml file is shown bellow:

```
analysis name: RUBY 25KeV 320deg # defaults to analysis

# working directory defaults to current working directory
# all relative paths specified herein are assumed to be in the working_dir
# any files not in working_dir should be specified with an absolute path
# working_dir:

multiprocessing: all # "all", or "half", or -1 means all but one, defaults to -1

material:
  definitions: material.cpl
  active: ruby

image_series:
  file:
    stem: Ruby25keVFULL320 \%04d.ge # can include relative or absolute path
    ids: [1,] # or can use globs: ["*2[4-9]"]
  images:
    start: 0
  omega:
```

```
    start: 0.0
    step: 0.25
    stop: 319.75
  #dark: RUBY4537medianDark
  flip: ccw90 # ~, v, h, hv, vh, cw, ccw

instrument:
  parameters: ruby_calibration.yml
  detector: # this section is only needed to convert old files to the new spec
    parameters_old: detector.cpl  # the old detector spec, produced by the GUI
    pixels: # this section required to convert from old detector spec
      rows: 2048
      columns: 2048
      size: [0.200, 0.200] # [row height, col width] mm

find_orientations:
  orientation_maps:
    # A file name must be specified. If it doesn't exist, one will be created
    file: Ruby25KeVFULL3200001etaomega.cpl

    threshold: 30
    #bin_frames: 1 # defaults to 1

    # "all", or a list of hkl orders used to find orientations
    # defaults to all orders listed in the material definition
    # active_hkls: [0,1,2,3,4]

  # either search full quaternion grid, or seed search based on sparse
  # orientation maps
  # use_quaternion_grid: some/file/name # defaults to seeded search
  seed_search: # this section is ignored if use_quaternion_grid is defined
    hkl_seeds: [0,2,3] # hkls ids to use, must be defined for seeded search
    fiber_step: 1.0 # degrees, defaults to ome tolerance

  threshold: 15 # defaults to 1. Threshold in polar rebinning

  omega:
    tolerance: 1.0 # in degrees, defaults to 2x ome step

    # specify the branch cut, in degrees. The range must be 360 degrees.
    # defaults to ["image_series:omega:start", "image_series:omega:start"+-360]
```

```
    # depending on sign of "image_series:omega:step"
    # period: [-180, 180] # in degrees, defaults to full 360 starting at "ome start"

  eta:
    tolerance: 1.0 # in degrees, defaults to 2x ome step
    mask: 5 # degrees, mask angles close to ome rotation axis, defaults to 5

  clustering:
    radius: 1.0
    completeness: 0.51 # completeness threshold
   #algorithm: fclusterdata # defaults to dbscan

fit_grains:
  do_fit: true # if false, extracts grains but doesn't fit. defaults to true

  estimate: RUBY_SWEEP_0/grains.out # defaults to None

  npdiv: 2 # number of polar pixel grid subdivisions, defaults to 2

  panel_buffer: 10 # don't fit spots within this many pixels from edge

  threshold: 25

  tolerance:
    tth: [0.25, 0.2]  # tolerance lists must be identical length
    eta: [2.0, 1.0]   # total width of window
    omega: [1.0, 0.5] #plus minus tolerance

  tth_max: 43.
```

- **analysis name** Select analysis name. Fitting routines will save output files in a folder with this name. This variable defaults to *analysis*.
- **working dir** Working directory can be selected to be different to the current working directory. If working directory is commented out, the program will default to the current working directory.
- **multiprocessing** Allows to select how many processing units the code uses.
- **material**
  - **definitions** Input the material pickle (.cpl) file name here (relative path)

  - **active** Enter name of active material as is stated in the material pickle file

- **image series**
  - **file**
    - **stem** Write file name stem for rotation series or name of single image. Relative or absolute path can be included. Standard c formatting is used for file numbering.
    - **ids** Enter list or range of file numbers to be written into file name stem.
  - **images**
    - **start** Enter the start frame number. This value is different from zero when empty frames are introduced in the rotation series by construction of the particular instrument used.
  - **omega**
    - **start** Enter start omega of the rotation series. Start and stop omegas are arbitrary but must match the range and step size of the experiment.
    - **step** Angular step size between diffraction images.
    - **stop** Enter end omega of rotation series.
  - **dark** Enter dark image file name if there is one, this can be with relative or absolute path. If there is no dark image comment out with hashtag.
  - **flip** Images must be aligned with the orientation that hexrd is expecting. The flip mode is described in the Reader tab section. If there is no flip this can be commented out.

- **instrument** Input detector calibration file name and detector pixel size, this is used to convert instrument parameter file type from the one produced in the gui to the one used in analysis scripts
  - **parameters** Name of the .yml file that will be created using the detector .cpl file created in the gui.
  - **detector**
    - **parameters old** File name of the instrument parameter file created in the gui.
    - **pixels**
      - **rows** Number of rows of pixels in the detector
      - **columns** Number of columns of pixels in the detector
      - **size** Pixel size in mm, [row height, column width].

- **find orientations** Information in this section is used in the find-orientations routine of hexrd.
  - **orientation maps** Refers to eta and omega orientation maps, these can be created manually or automatically using information in this section.
    - **file** File name of the orientation maps, if they were done manually in gui use file name from export, if not the program will make a orientation maps file with the name selected here.
    - **threshold** Threshold that was found in the raw data under the Colormap section.
    - **bin frames** Frames can be binned for faster calculations, this option is rarely needed and should typically be commented out.
    - **active hkl** HKL's used for indexing can be set here. This option can be commented out if the materials.cpl file from the gui is saved, in this case the HKL's selected in the GUI will be used.
  - **use quaternion grid** When there are a lot of grains, on the order of a few hundreds, a file with a grid in orientation space can be provided to search for orientations using this grid. For a single crystal or just a few grains, it is better to use the seeded search.
  - **seed search**
    - **hkl seeds** Select two or three HKL's here to generate the search in orientation space with these particular HKL's. Look at eta and omega plots in polar rebinning in the gui to select orientation plots that have less saturated spots.
    - **fiber step** Distance in between the point along an orientation fiber that is calculated from each point in the omega-eta maps that are used to test for predicted orientations. For a single crystal or just a few grains in the sample this can be done in large steps, 1 degree for a ruby calibrant is reasonable.
  - **threshold** This is the threshold found in the eta-omega plots from polar rebinning routine.
  - **omega**
    - **tolerance** This tolerance defines how many pixels along the omega direction does the find-orientations routine look for intensity in the omega-eta maps around a test orientation. Select a tolerance equal to the fiber step size is good practice, never smaller.
  - **eta**
    - **tolerance** Defines how many pixels along the eta direction does the find-orientations routine look for around a tested orientation position.

    * **mask** This is used to exclude orientations that are too close to 90 and -90 degrees which is the position of the rotation axes of the sample, these orientation are typically streaked because they move slowly through the brag condition and are best to be excluded. Defaults to 5 degrees.

  - **clustering** Looks for orientation clusters that define grains.
    * **radius** Should not be smaller than the fiber steps. Selecting a radius equal to the fiber step is a good practice.
    * **completeness** Ratio of tested orientations within the omega-eta tolerances that have intensities above the omega-eta plots background intensity threshold with tested orientations that are not found, i.e. have no intensity above background. A low completeness of about 0.5 allows for small grains that have a lot of missing or very weak reflections to be found and accounted for.
    * **algorithm** Different clustering algorithms can be selected.

- **fit grains**
  - **do fit** True or false, defaults to true. If false is selected the routine calculates grains using tolerances inputted bellow, but does not perform a fit.
  - **estimate** Path to file that contains estimate of grains, this can be a previous fit that the routine can start with. If there is no initial estimate this can be commented out, variable defaults to none. When no initial estimate is selected the routine uses the .dat file that contains indexed orientations from find-orientations routine.
  - **npdiv** A regular grid in two-theta, eta and omega space is set around each predicted reflection. Npdiv enables you to choose the size of the angular pixel size used in the fit-grains routine with respect to the cartesian pixel size. If 1 is selected the angular pixel size will be roughly the same size as the cartesian pixel size. If you select 2, the angular pixel size will be half of the cartesian pixel size, which produces an oversampling that is generally recommended to extract intensities. Npdiv defaults to 2.
  - **panel buffer** Number of pixels from the edge of the detector that are ignored to avoid reading out of the edge of the detector and getting nan's in the intensity array.
  - **threshold** Background threshold selected in the two-theta, eta plots.
  - **tolerance** Two item lists must be inputed in tolerance arguments. The routine will start with a coarse fit using tolerances in the first item of the list and will proceed with a finer fit using second tolerance on list.
    * **tth** Two-theta tolerance in absolute value (not plus minus tolerance). It is recommended to see stacked image in the Colormap of the gui to select an

appropriate two-theta tolerance, zoom into a typical spot and see what range it covers in two theta by putting mouse over min and max two theta and reading coordinates in bottom information bar.

  * **eta** Tolerance in eta channel, absolute value. This can be determined with the colormap in the gui as the two-theta is.
  * **omega** Plus minus tolerance in the omega channel. Omega tolerance is discretized by the angular step size between each frame. Usually the width of diffraction spots in eta and omega are equivalent so the same tolerance found in eta can be used for omega. It is also possible to scroll through individual frames and find omega threshold by finding the typically width of diffraction spots in omega.

- **tth max** True, false or non negative value arguments. Sets the maximum two-theta value. If false or commented out, the variable defaults to the maximum two-theta defined by the last HKL ring that is stored in the materials.cpl file. Setting this value to true will give the maximum two-theta that has a complete HKL ring. It is recommended to use as many HKL's as possible, in particular for a single crystal, to perform a reliable fit. For this purpose find the maximum two-theta in raw data and input value here.

4.4 Preliminary Results

Preliminary results of synchrotron x-ray high pressure diamond anvil cell experiments on olivine transformed to bridgmanite + periclase using the multigrain data acquisition and analysis technique are presented in this section. Special attention is given to identify ways that this technique can be more readily available to the high pressure diamond anvil cell community, in particular when such weakly diffracting materials are used. It is of interest to apply this technique to study texture evolution in coarse grained polycrystalline materials deformed at high pressure, and to explore orientation relationships of phase transformations at high pressure. Nonetheless, it has been just recently considered to be applied for DAC data analysis, and there is still experimental and software development to be done to achieve this goal. In this study we have taken the first steps in to achieving the application of this technique to the diamond anvil cell. Experiments were performed at beamline 12.2.2 of the Advanced Light Source at Lawrence Berkeley National Laboratory.

A coarse grained San Carlos olivine was deformed up to 33GPa and then transformed using brief laser heating to a bridgmanite + periclase aggregate. A boron epoxy gasket (Merkel and Yagi, 2005) was used to provide a more ductile confining medium that can apply pressure on the large grains compared to the sample chamber size. At 33GPa the olivine sample was laser heated to induce the phase transformation to the bridgmanite + periclase two phase system. Once the transformation has occurred, the sample was further deformed up to about 53GPa. The sample is compressed in the diamond anvil cell under

uniaxial compression. No hydrostatic pressure medium is used, so considerable elastic and plastic deformation occurs. Elastic deformation warps Debye rings into ellipses and plastic deformation streaks diffraction spots that originate from highly deformed grains. A raw diffraction image of bridgmanite + periclase at about 44GPa is shown in Figure 4.14. Here the intensity of all the frames in the rotation series are summed into one image, frames at the edges of the rotation series are excluded due to strong diffraction rings coming from the DAC and frames that have strong diamond reflections are also excluded. Also, some strong diffraction spots from highly plastically deformed grains are masked.

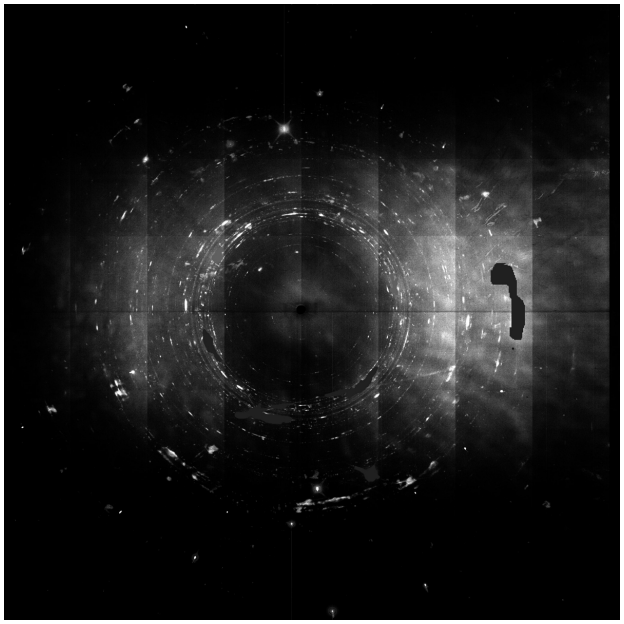

Figure 4.14: *Sum of maximum intensities over selected frames taken of bridgmanite + periclase at about 44GPa. Frames at edges of the rotation series are removed due to strong DAC diffraction rings. Additionally, frames with strong diamond reflections were also removed.*

The two phases must be analyzed separately using HEXRD. First the bridgmanite phase analysis is presented. A key step in a successful analysis using HEXRD is to know the correct lattice parameters for the particular pressure that the sample is at, and to identify the Debye rings for the different hkl planes that correspond to each phase in the rotation series collapsed image. This provides a good first guess for the HEXRD code to search for diffraction spots for each HKL plane. Due to the lack of many diffraction spots, two different methods were used to identify two-theta values for the HKL planes of the two phases in question. First, the software *Dioptas* was used at the beamline to determine the pressure at which the image was taken (Prescher and Prakapenka, 2015). This is done by taking a simple still image of the sample, loading it to *Dioptas* that is previously calibrated using a

CeO_2 powder diffraction pattern, and integrating the pattern along the azimuth angle which runs parallel to the plane of the image. *Dioptas* reads equation of state information from the Joint Committee on Powder Diffraction Standards (JCPDS) database and calculates pressure using peak positions for each phase. Once this approximate pressure is established, it is recommended to load a summed of all frames image to a more sophisticated analysis software to determine the positions of the different HKL planes in the two-theta range of the diffraction image. In the case of this study the software MAUD was used for this purpose (Lutterotti et al., 2014). Figure 4.15 shows labels for a few HKL planes identified in the image. A zoom in to low two-theta values is shown for clarity. Smooth portions of rings that are off center from the main pattern are secondary diffraction rings that originate form strong diamond reflections. Straight lines indicate highly saturated spots. In MAUD it was discovered that there are some lingering olivine peaks, this is quite common since laser heating tends to be very inhomogeneous.

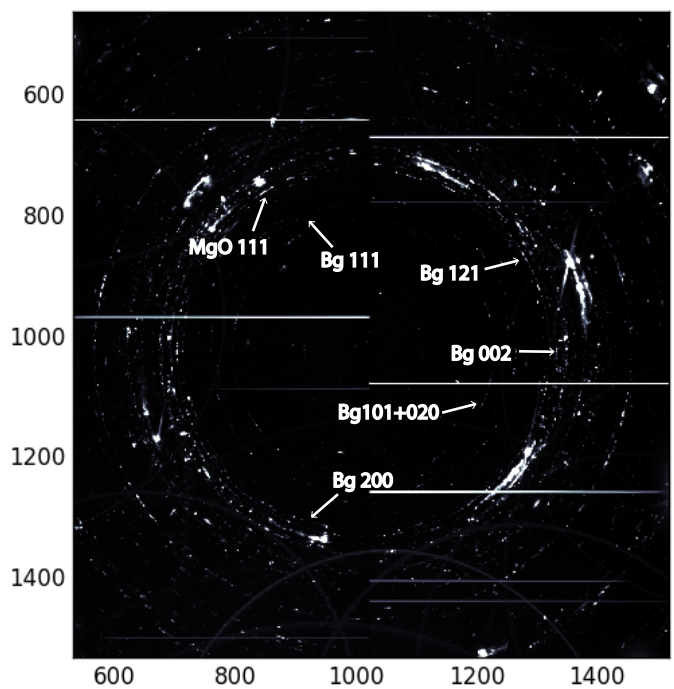

Figure 4.15: *Max over all frames image of bridgmanite + periclase aggregate at about 44GPa. A few hkl planes for each phase are labeled. Secondary diffraction rings originate from strong diamond reflections, and straight lines from highly saturated spots.*

Once the two-theta positions for the different HKL planes in the data are identified, the appropriate lattice parameters are selected in HEXRD so that the predicted rings match with the data. The predicted ring positions and two-theta range must be carefully selected. The range must be selected large enough so that the search algorithm can find spots that

might be in slightly different two-theta values due to elastic deformation, but that pertain to the same HKL, but narrow enough so that the ranges for the different active HKL's used do not overlap. Another important consideration is that it si recommended to select HKL's that have high structure factors, to improve the chances of having a successful analysis. In these low symmetry, highly plastically deformed minerals, it is also recommended to avoid using HKL's that are close enough together where peak intensity overlap could happen.

The 200, 121, 111 and 002 planes (in the Pnma setting) were selected as the active HKL's for the bridgmanite phase and eta-omega plots were calculated using the polar rebinning option in HEXRD (Figure 4.16). The eta angle axis of rotation comes out of the plane of the diffraction image, and omega is the rotation angle at each step in the data acquisition rotation series procedure, see Figure 4.6 for a complete schematic of the experimental setup. Strong plastic deformation spreading diffraction spots in eta and especially in omega immediately stands out in Figure 4.16. Plastic deformation is the strongest in the 002 HKL plane (Figure 4.16b). Streaking of these spots present challenges to HEXRD.

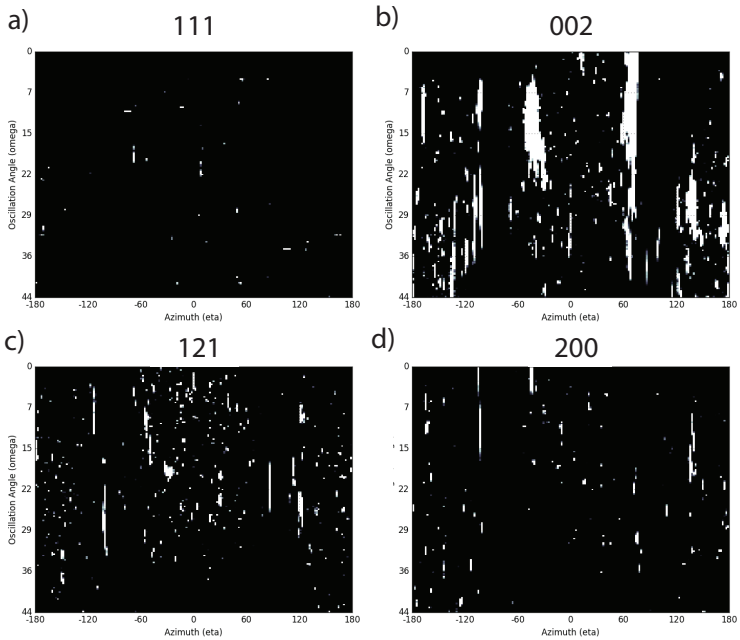

Figure 4.16: *Eta-omega plots of the four active HKL's selected for the bridgmanite phase. The eta angle axis of rotation comes out of the plane of the diffraction image, and omega is the rotation angle at each step in the data acquisition rotation series procedure. a) shows eta-omega plots of the 111 plane, b) the 002, c) the 121 and d) the 200. These planes are in the Pbnm setting and they are arranged from low to high two-theta.*

Due to the large streaks in the 002 HKL plane eta-omega plot (Figure 4.16), the 111, 121 and 200 planes were selected as seeds to generate the search in orientation space done

by the fit-orientations routine in HEXRD. In this rotation series at 44 GPa, 499 orientations were indexed for the bridgmanite phase.

The periclase phase was also identified in the data. Two-theta values were found for the visible HKL's in the diffraction images and lattice parameters were adjusted in HEXRD accordingly. Eta-omega plots are shown in Figure 4.17. Although at a smaller degree, diffraction spots are found to also have a large spread in the omega channel. In this case 83 orientation clusters were indexed by HEXRD.

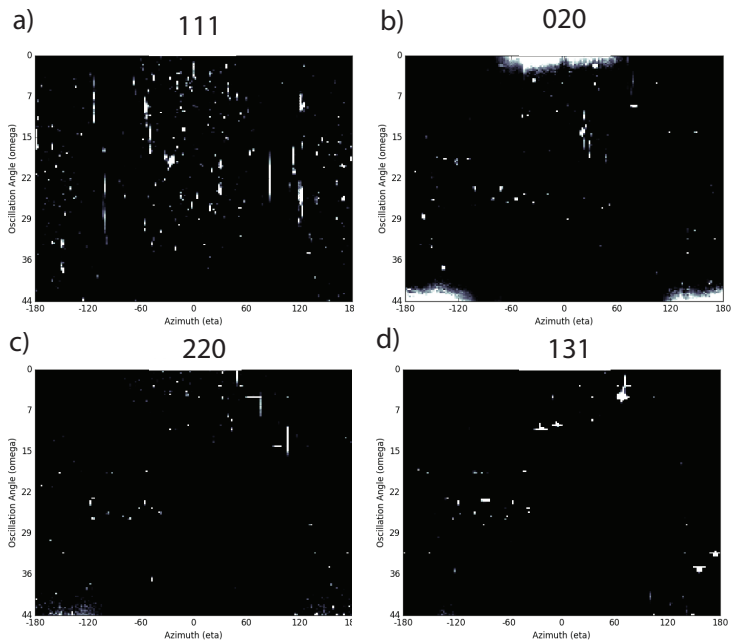

Figure 4.17: *Eta-omega plots of the four active HKL's selected for the periclase phase. The eta angle axis of rotation comes out of the plane of the diffraction image, and omega is the rotation angle at each step in the data acquisition rotation series procedure. a) shows eta-omega plots of the 111 plane, b) the 020, c) the 220 and d) the 131. These planes are in the Pbnm setting.*

4.5 Discussion and Conclusions

The application of the multigrain data acquisition and analysis technique for texture studies in the diamond anvil cell has been considered. Preliminary results show successful indexing of spots for the bridgmanite and periclase phases but further experimental development is required to access a larger range of orientations and get a more complete map in orientation space of the grains in the sample. For this it is suggested to use a very simple cell holder, and compress the diamond anvil cell by tightening the screws on the cell instead of using

a pressure membrane set up. This would enable to flip the cell 180 degrees and do a rotation series on both sides of the opening to obtain a more complete orientation map of the sample. The BX90 diamond anvil cell is an excellent candidate for these experiments due to the 90 degree angle opening in the axial direction. It is also recommended to start with a less complex system to isolate the problem with streaking due to plastic deformation. Certain thresholds and algorithms will have to be applied in the software to deal with this type of data. The low orthorhombic symmetry of bridgmanite and the scarce amount of periclase adding to the weak diffraction inherent to their low Z number present considerable challenges to the technique. A diamond anvil cell study presented by Langrand et al. (2017) and performed on orthorhombic polycrystals of $MgSiO_3$ post-perovskite show that for this system the resolution typically used in multigrain studies is not sufficient for *in situ* analysis of spatial relationships in this material, but that grain orientations are resolved to enable tracking of phase transformations and plastic deformation processes.

The multigrain technique is a powerful tool for analyzing high pressure diffraction data. it provides access to a larger range of grain sizes than the traditional Rietveld and single crystal analysis techniques. It is perfectly suited for texture studies since a very large number of orientations satisfy the brag condition because of the image rotation series taken of the sample and the underlying mechanisms that produce texture can be quantified. However, considerable advances must be made in order to reach these goals for the low symmetry systems of interest to this study.

References

Bernier, J., N.R., B., Brandes, M., Lienert, M., Miller, M., and Mills, M. (2010). Exploring crystal plasticity via far-field 3DXRD. *31st International Symposium on Materials Science: Challenges in materials science and possibilities in 3D and 4D characterization techniques.*

Bernier, J., N.R., B., Lienert, U., and Miller, M. (2011). Far-field high-energy diffraction microscopy: a tool for intragranular orientation and strain analysis. *Journal of Strain Analysis*, 46:527–547.

Hansen, N., Juul Jensen, D., Nielsen, S., Poulsen, H., and Ralph, B., editors (2010). *3DXRD at the Advanced Photon Source: Orientation Mapping and Deformation Studies*, volume 59. Risoe 2010 Symposium.

Hu, Q., Kim, D., Yang, W., Yang, L., Meng, Y., Zhang, L., and Mao, H.-k. (2016). FeO_2 and FeOOH under deep lower-mantle conditions and Earth's oxygen-hydrogen cycles. *Nature*, 534:241–24.

Ice, G., Dera, P., Liu, W., and Mao, H.-k. (2005). Adapting polychromatic X-ray microdiffraction techniques to high-pressure research: energy scan approach. *Journal of Synchrotron Radiation*, 12(5):608–617.

Juul Jensen, D., Lauridsen, E., Margulies, L., Poulsen, H., Schmidt, S., Sorensen, H., and Vaughan, G. (2006). X-ray microscopy in four dimensions. *Materials Today*, 9(1):18 – 25.

Kantor, I., Prakapenka, V., Kantor, A., Dera, P., Kurnosov, A., Sinogeikin, S., Dubrovinskaia, N., and Dubrovinsky, L. (2012). BX90: A new diamond anvil cell design for x-ray diffraction and optical measurements. *Review of Scientific Instruments*, 83(12):125102.

Langrand, C., Hilairet, N., Nisr, C., Roskosz, M., Ribárik, G., Vaughan, G., and Merkel, S. (2017). Reliability of multigrain indexing for orthorhombic polycrystals above 1Mbar: application to $MgSiO_3$ post-perovskite. *Journal of Applied Crystallography*, 50(1):120–130.

Letoullec, R., Pinceaux, J., and Loubeyre, P. (1988). The membrane diamond anvil cell: A new device for generating continuous pressure and temperature variations. *High Pressure Research*, 1:77–90.

Lutterotti, L., Vasin, R., and Wenk, H.-R. (2014). Rietveld texture analysis from synchrotron diffraction images. i calibration and basic analysis. *Powder Diffraction*, 29:76–84.

Margulies, L., Winther, G., and Poulsen, H. F. (2001). In situ measurement of grain rotation during deformation of polycrystals. *Science*, 291(5512):2392–2394.

Merkel, S. and Yagi, T. (2005). X-ray transparent gasket for diamond anvil cell high pressure experiments. *Review of Scientific Instruments*, 76:046109.

Nisr, C., Ribarik, G., Ungar, T., Vaughan, G., Cordier, P., and Merkel, S. (2012). High resolution three-dimensional X-ray diffraction study of dislocations in grains of $MgGeO_3$ post-perovskite at 90 GPa. *Journal of Geophysical Research: Solid Earth*, 117(B3).

Nisr, C., Ribarik, G., Ungar, T., Vaughan, G., and Merkel, S. (2014). Three-dimensional X-ray diffraction in the diamond anvil cell: application to stishovite. *High Pressure Research*, 34(2):158–166.

Obstalecki, M., Wong, S., Dawson, P., and Miller, M. (2014). Quantitative analysis of crystal scale deformation heterogeneity during cyclic plasticity using high-energy x-ray diffraction and finite-element simulation. *Acta Materialia*, 75:259 – 272.

Oddershede, J., Wright, J., Beaudoin, A., and Winther, G. (2015). Deformation-induced orientation spread in individual bulk grains of an interstitial-free steel. *Acta Materialia*, 85:301 – 313.

Pagan, D., Shade, P., Barton, N., Park, J.-S., Kenesei, P., Menasche, D., and Bernier, J. (2017). Modeling slip system strength evolution in Ti-7Al informed by in-situ grain stress measurements. *Acta Materialia*, 128:406 – 417.

Poulsen, H. (2004). *Three-Dimensional X-Ray Diffraction Microscopy*, volume 205 of *0081-3869*. Springer Berlin Heidelberg.

Poulsen, H., Margulies, L., Schmidt, S., and Winther, G. (2003). Lattice rotations of individual bulk grains. *Acta Materialia*, 51(13):3821 – 3830.

Prescher, C. and Prakapenka, V. (2015). DIOPTAS: a program for reduction of two-dimensional x-ray diffraction data and data exploration. *High Pressure Research*, 35:223–230.

Rosa, A., Hilairet, N., Ghosh, S., Perrillat, J.-P., Garbarino, G., and Merkel, S. (2016). Evolution of grain sizes and orientations during phase transitions in hydrous Mg_2SiO_4. *Journal of Geophysical Research: Solid Earth*, 121(10):7161–7176. 2016JB013360.

Rosa, A. D., Hilairet, N., Ghosh, S., Garbarino, G., Jacobs, J., Perrillat, J.-P., Vaughan, G., and Merkel, S. (2015). In situ monitoring of phase transformation microstructures at Earth's mantle pressure and temperature using multi-grain XRD. *Journal of Applied Crystallography*, 48(5):1346–1354.

Sachs, G. (1928). Zur Ableitung einer Fliessbedingung. *Z. Verein Deut. Ing.*, 72:734–736.

Schmidt, S., Nielsen, S. F., Gundlach, C., Margulies, L., Huang, X., and Jensen, D. J. (2004). Watching the growth of bulk grains during recrystallization of deformed metals. *Science*, 305(5681):229–232.

Taylor, G. (1938). Plastic strain in metals. *Journal of the Institute of Metals*, 62:307.

Uchic, M., Holzer, L., Inkson, B., Principe, E., and Munroe, P. (2007). Three-dimensional microstructural characterization using focused ion beam tomography. *MRS Bulletin*, 32(5):408416.

Volkert, C. A. and Minor, A. M. (2007). Focused ion beam microscopy and micromachining. *MRS Bulletin*, 32(5):389399.

Wenk, H.-R., Lonardelli, I., Merkel, S., Miyagi, L., Pehl, J., Speziale, S., and Tommaseo, C. (2006). Deformation textures produced in diamond anvil experiments, analyzed in radial diffraction geometry. *Journal of Physics: Condensed Matter*, 18:S933–S947.

Winther, G., Margulies, L., Schmidt, S., and Poulsen, H. (2004). Lattice rotations of individual bulk grains part ii: correlation with initial orientation and model comparison. *Acta Materialia*, 52(10):2863 – 2872.

Wong-Ng, W., Siegrist, T., DeTitta, G., Finger, L., Evans Jr., H., Gabe, E., Enright, G., Armstrong, J., Levenson, M., Cook, L., and Hubbard, C. (2001). Standard reference material (SRM 1990) for single crystal diffractometer alignment. *Journal of Research of the National Institute of Standards and Technology*, 106:1071–1094.

Chapter 5

Concluding Remarks

Plastic deformation due to dislocation glide and subsequent texture development in two-phase polycrystalline aggregates has been studied by means of computer simulations using finite element and fast Fourier transform formulations, and also experimentally at high pressure in the diamond anvil cell. In particular, the bridgmanite + periclase mixture, at 75% and 25% volume fractions respectively, is studied due to to its relevance to understanding plastic deformation, and possible texture development, in the lower mantle of the Earth. Large scale convection currents, subducting slabs and mantle plumes are expected to introduce high strains in mantle rocks, providing conditions that are favorable for plastic deformation by dislocation creep. Studying the effects of dislocation movement and its effects on bulk aggregate properties becomes a crucial part of painting a big picture of the dynamics of the interior of the Earth, in particular of the lower mantle with the bridgmanite + periclase two phase aggregates. Furthermore, the use and implementation of a variety of different techniques to study this two phase aggregate provides insight into the strengths and weaknesses of each one, providing an important framework for further investigation of these polyphase polycrystalline systems.

The finite element framework implemented in the FEpX code was adapted to work with the lower orthorhombic symmetry of bridgmanite (Chapter 2). Slip systems for the cubic periclase phase that has a FCC structure but does not deform in the typical FCC slip system was also implemented. Furthermore, post processing scripts were developed to explore texture and misorientation development as the aggregate is deformed under compression. Plastic deformation rate and misorientation distributions were analyzed to capture heterogeneities that develop at a local grain scale. Two polycrystalline phase simulations were compared with single phase simulations using the same microstructure be able to understand the effects of having a two phases with contrasting mechanical properties on texture and the development of local heterogeneities in the aggregate. It is also important to discern between heterogeneities introduced by anisotropy of the single crystal mechanical properties of the mineral phases in question, and heterogeneities introduced by the contrasting rheologies. With this same objective, two different two phase simulations were carried out:

one where both phases have the same yield strength, and another where the bridgmanite phase has a yield strength 8 times higher than the softer periclase phase. It was found that although yield strength contrast between the two phases plays an important role in the development of local grain heterogeneities, especially of the soft periclase phase, the large anisotropy in the single crystal mechanical properties of the lower symmetry orthorhombic bridgmanite phase also plays a key role. It is found that when the yield strength contrast is large, the softer periclase phase absorbs most of the deformation. It develops strong heterogeneities in the plastic deformation rate, and presents higher intragranular misorientations than the harder bridgmanite phase. Moreover, the bridgmanite phase shows little change when the yield strength contrast is increased and heterogeneities are actually lessened with the introduction of the softer periclase in this 25% volume fraction. Indicating that the source of heterogeneities in the bridgmanite phase is the large anisotropy introduced by its low symmetry and few slip systems. Further investigation into the influence of microstructure is prescribed. Creating different virtual polycrystals with varying spatial arrangement and volume fractions would provide more insight into the deformation behavior of anisotropic polyphase polycrystalline aggregates with this finite element approach.

A viscoplastic fast Fourier transform formulation was also employed to model plastic deformation by dislocation glide in 75% bridgmanite + 25% periclase polycrystalline aggregates, and results are presented in Chapter 3. Using the VPFFT code, the influence of microstructure in texture and local grain heterogeneity development was studied. Four different microstructures were proposed: one with periclase grains in the cores of bridgmanite grains, a second where periclase grains percolate around bridgmanite grains (and bridgmanite grains are never in contact with one another), a third where the locations of grains of the periclase phase are selected at random, and a fourth where periclase grains are in the triple junctions of bridgmanite grains. Texture after 30% compressive strain was recorded and individual orientations of the voxels that compose a few selected grains were analyzed and compared. Distributions of the strain rate component along the compression direction were calculated and also bined according to wether they are at grain boundaries or in the interior of grains, to exhibit statistical differences between the two cases. It is found that there is no microstructure dependence of the texture, slip system activity and strain rate distributions for the core, random and triple microstructure. Regions along the grain boundaries of periclase grains show a more heterogeneous distribution of the strain rate, and the interiors of grains of the periclase phase and the bulk of the grains of the bridgmanite phase have very similar distributions of this quantity. This indicates that local heterogeneities are concentrated at grain boundaries of grains of the softer periclase phase. In the case of these VPFFT simulations, most of the slip system activity is carried by the bridgmanite phase, which is in disagreement with finite element results from Chapter 2. A strong microstructure dependence in the percolate microstructure was found. Texture in the bridgmanite is about 4 times stronger than in the other microstructures, and although texture strength in periclase is comparable to the other microstructures, the slip system activity is considerably different. Furthermore, strain rate distributions in the grains boundaries of the periclase phase in

the percolate microstructure have similar distributions than these same regions in the other three microstructures, but the bridgmanite phase presents a more narrow distribution of the strain rate values, indicating a more homogeneous deformation environment. This explains the sharper texture that develops in bridgmanite deforming in this percolate microstructure. Further investigation into the influence of yield strength contrast in texture and local heterogeneity development using this FFT formulation is required. This technique can use experimental microstructural data as input to the viscoplastic code, doing would provide valuable information that more directly relates with physical systems.

General trends in deformation behavior of the bridgmanite + periclase polycrystalline aggregates are captured by both models. Except in the case of the percolate microstructure simulation with VPFFT, bridgmanite and periclase develop very weak textures in both two phase simulations and single phase simulations. The periclase phase develops strong heterogeneities in the plastic deformation rate in FEpX and the strain rate distributions in VPFFT when deformed in a two phase mixture with bridgmanite, and deformation is very homogenous when deformed on its own. Also, intragranular misorientation of the periclase phase is larger when deformed in a two phase aggregate and it does not change considerably in the bridgmanite phase. Bridgmanite has more narrow strain rate distributions when deformed together with periclase than as a single phase. This indicates that the source of heterogeneities in bridgmanite are the anisotropy in the single crystal properties. Although further investigation is necessary, FEpX and VPFFT results suggest that weak textures in bridgmanite are due to large intragranular misorientations that develop due to anisotropy introduced by the low symmetry of the phase. Moreover, weak textures in periclase can be explained by large intragranular misorientation in the FEpX model, and low stresses that are not enough to activate periclase slip systems are the culprit in the VPFFT model. These two models are in strong disagreement when it comes to slip system activity; in FEpX simulations it is the softer periclase phase that carries most of the slip system activity, whereas in VPFFT bridgmanite has the majority. A systematic comparison of these two models is required to explain this contrasting behavior. Percolate microstructure VPFFT results hints towards a microstructure dependence of texture development, but further investigation is necessary.

High pressure diamond anvil cell experiments using synchrotron radiation at 25 KeV were performed at beamline 12.2.2 of the Advanced Light Source of Lawrence Berkeley National Laboratory on bridgmanite + periclase aggregates to characterize texture development at high pressure in nonhydrostatic conditions in a diamond anvil cell. Traditional Rietveld refinement techniques used to analyze resulting 2D diffraction patterns limits samples to small grain sizes to achieve smooth intensity variations along Debye rings. A multigrain indexing analysis technique has recently been adopted by the high pressure diamond anvil cell community to overcome these limitations of the Rietveld analysis technique. The implementation of this data collection method and analysis technique using the software HEXRD is discussed in Chapter 4 for the bridgmanite + periclase two phase system transformed at high pressure and temperature from the mineral olivine. It was successfully used to analyze diffraction spots from different grains, which enables larger grains sizes that were previously

accessible for the Rietveld technique. While the technique is still under development, it will enable characterization of texture development in a wider variety of grain sizes, and will play a crucial role in understanding orientation relationships of high pressure transformations in polycrystalline aggregates.

x

Appendix A

FEpX Postprocessing Scripts

Scripts presented here are MATLAB functions.

Make Two-Phase Random Microstructure

A random microstructure is created and meshed using the software Neper, but Neper can only assign a single phase to the whole aggregate. The MakeRandomTwoPhAggregate Matlab script takes the Neper generated microstructure and reassigns phase numbers to random generated grains in order to make them of phase 2. The user selects the volume fraction as input.

```
function [] = MakeRandomTwoPhAggregate(fname, vf) %
% MATLAB SCRIPT THAT GENERATES A TWO PHASE RANDOM MICROSTRUCTURE FROM
%NEPER .GRAINS FILE OUTPUT %
% Load grain and phase information tomatrix f
f = load([fname,'.grain']);
%
% Extract number of elements and number of grains and make a row vector for later
nelem=f(1,1);
ngrain=f(1,2);
row1=[nelem,ngrain]
%
% Specify volume fraction of phase 2 and calculate number of grains that it will
be assigned
n2=round(ngrain*vf);
%
% Generate random (no repeat) integers to define what grain numbers are phase
2
ngr2 = randperm(ngrain,n2);
```

```
%
% For each grain number of phase 2, find its row in .grains file and save a logical
array with the positions
g(1:nelem,1)=0;
for i=1:n2
g1=g;
z=[f(2:nelem+1)==ngr2(i)]';
g=g1+z;
end
%
% Assign a number 2 to each row of phase 2 and a number 1 for each grain of phase
1
g2=g*2;
g2(g2==0)=1;
%
% Make matrix with new grain assignments, add file header and print to file
grph=[f(2:nelem+1,1),g2];
grph2=[row1;grph];
dlmwrite([fname,'.grain'],grph2,'delimiter','t', 'precision', '%7d')
%
```

Export Orientations to BEARTEX Format

FepxtoBeartexCPT Matlab function reads orientation angles for each element in the virtual polycrystal, transforms them to the bunge convention and writes them to a CPT file format that is later processed in the software BEARTEX. The function assigns the grain number to each element and prints CPT files for the desired deformation step.

```
function FepxtoBeartexCPT(fname,d,ns,ph)
% FUNCTION THAT WRITES CPT FILE FROM FEpX RUN OUTPUT.
  % INPUTS
  % fname = job name
  % d = matlab array from ReadFepxData
  % ns = printed displacement step you want to print cpt for
  % ph = phase number you would like to print
%
% Read .grain file to get number of elements and grain and phase information
  nel=load([fname,'.grain']);
  nelem=nel(1,1);
%
```

```
% Remove header from .grains data
  nel(1,:)=[];
%
% Create rows array for selected phase (ph) by user.
% There must be one cpt file for each phase
  rows=find(nel(:,2)==ph);
%
% Change angle convention from Kocks to Bunge and transpose
  Bangs=BungeOfKocks(d.angs(:,:,:),'degrees');
%
% Calculate start and end rows for desired displacement step
% and make array with selected step
  selangB=Bangs(:,:,ns)';
%
% Print ones and ceros and element number column
  one(1:nelem)=1;
  ones=one';
  cero(1:nelem)=0;
  ceros=cero';
 el=(1:nelem);
 elems=el';
 sstp(1:nelem)=ns;
 strstp=sstp';
%
% Put it all together in one single array
  array=[selangB strstp nel ceros ones ceros ones elems];
%
% Select rows corresponding to selected phase.
% There will be on .cpt for each phase
  array=array(rows,:);
%
% Write in file. You can have an initial file called tex1.cpt
% with he appropriate header on, or you can add the header manually after
filename = sprintf('tex%d-stp%d.cpt',ph,ns);
texcpt = fopen(filename,'a');
formcpt = '%8.2f%8.2f%8.2f%6.0f%6.0f%6.0f%6.0f%6.0f%6.0f%6.0fn';
fprintf(texcpt,formcpt,array');
fclose(texcpt);
%
```

Export Starting Orientations to BEARTEX

Due to the finite sampling size, it is important to plot the starting texture in order to make sure that it is reasonably random. This can also prove useful if one wishes simulate plastic deformation in an aggregate with a starting texture. The StartOritoBeartexCPT function reads the initial orientations of the aggregate and prints them in CPT format to be read in BEARTEX.

```
function StartOritoBeartexCPT(fname,ngrains)
%
kocks=load([fname,'-2.kocks']);
kocks=kocks';
% Change angle convention from Kocks to Bunge and transpose
Bangs=BungeOfKocks(kocks,'degrees');
angB=Bangs';
%
% Print ones and ceros and element number column
one(1:ngrains)=1;
ones=one';
cero(1:ngrains)=0;
ceros=cero';
el=(1:ngrains);
elems=el';
nel=(1:ngrains);
nel=nel';
sstp(1:ngrains)=0;
strstp=sstp';
%
%
% Put it all together in one single array
array=[angB strstp nel ceros ones ceros ones elems];
%
% Write in file. You can have an initial file called tex0.cpt with he appropriate
header on, or you can add the header manually after
tex0cpt=fopen('tex0.cpt','a');
formcpt='%8.2f%8.2f%8.2f%6.0f%6.0f%6.0f%6.0f%6.0f%6.0f%6.0fn';
fprintf(tex0cpt,formcpt,array');
%
```

Export Orientations of a Single Grain to PTXX

The FepxtoBeartexPTXX matlab function selects orientations of a single grain of the users choice at a range of deformation steps, also selected by the user. It prints orientations for all the voxels of the selected grain, together with strain, grain information and the element number.

```
function FepxtoBeartexPTXX(fname,d,ns,nf,nint,graino)
% FUNCTION THAT WRITES CPT FILE FROM SINGLE PHASE FEpX RUN OUTPUT
% INPUTS
% fname = job name
% nprocs = number of processors used in the job
% nsteps = number of load steps. OJO!! NOT NUMBER OF ITERATIONS
% ns = displacement step START you want to print
% nf = displacement step END you want to print
% nint = displacement step intervals you want to print
%
%
% Read FEpX data and concatenate different processor files (and also all disp
steps)
%d=ReadFepxData(nprocs,nsteps);
%
% Read .grain file to get number of elements and grain and phase information
grph=load([fname,'.grain']);
nelem=grph(1,1);
%
% Calculate number of steps to print
nstp=((nf-ns)/nint)+1;
%
% Remove header from .grains data and repeat for all strain steps
grph(1,:)=[];
% Repeat grain and phase data to fill all rows
grph=repmat(grph,nstp,1);
% size(grph);
%
grow=(grph(:,1)==graino);
gsize=size(grow);
%
% Change angle convention from Kocks to Bunge and traspose
angB=BungeOfKocks(d.angs(:,:,:),'degrees');
%
```

```
% Calculate start and end rows for all desired displacement steps
% and make orientation array
angs=[];
for i=1:nstp
 ni=ns+nint*(i-1);
 angles=angB(:,:,ni);
 angles=angles';
 angs=[angs;angles];
end
nrow=size(angs,1);
%size(angs)
%
% rows=[];
%for i=ns:nint:nf
%si=i*nelem-nelem+1;
%fi=si+nelem-1;
                %rowsi=[si:1:fi];
                %rows=[rows;rowsi];
                %end
                %rows=rows;
%selangB=angB(rows,:);
                %nrow=size(selangB,1);
                %
                %
% Print ones and ceros
one(1:nrow)=1;
ones=one';
cero(1:nrow)=0;
ceros=cero';
                %
         % Print element number for all strain steps
el=(1:nelem)';
                eles=repmat(el,nstp,1);
elems=eles;
                %
         % Print strain step for each
                str=[];
                count=0;
                for i=1:nstp
                    if i==1
                        ms=1;
```

```
                        mf=nelem;
                        str(ms:mf,1)=ns;
                    else
                        ms=(i-1)*nelem+1;
                        mf=i*nelem;
                        str(ms:mf,1)=ns+nint*(i-1);
                    end
                end
                %
                 %
% Put it all together in one single array
array=[angs str grph ceros ones ceros ones elems];
                %
        % Select information relevant to grain chosen by user
                grarray = array(grow,:);
                %
% Write file.
filename = sprintf('texPTXX-grain%d-stp%d.cpt',graino,nf);
texPTXXcpt=fopen(filename,'a');
formcpt='%8.2f%8.2f%8.2f%6.0f%6.0f%6.0f%6.0f%6.0f%6.0f%6.0fn';
fprintf(texPTXXcpt,formcpt,grarray');
%
```

Export Orientations from a Domain in a Grain to PTXX

The FepxtoBeartexPTXXdomAniso matlab function selects a domain of a grain to plot discrete orientations in the PTXX program of BEARTEX. It prints the selected domain at a range of deformation steps at a defined interval by the user. This script can be used if the orientations of a grains domain wished to be tracked as deformation progresses.

```
function FepxtoBeartexPTXXdomAniso(fname,d,ns,nf,nint,graino,nstrunc,nftrunc)
% FUNCTION THAT WRITES CPT FILE FROM SINGLE PHASE FEpX RUN OUTPUT OF A DOMAIN
IN A GRAIN
% INPUTS
% fname = job name
% nprocs = number of processors used in the job
% nsteps = number of load steps. OJO!! NOT NUMBER OF ITERATIONS
% ns = displacement step START you want to print
% nf = displacement step END you want to print
```

```
            % nint = displacement step intervals you want to print
            %
            %
% Read FEpX data to concatenate different processor files (and also all disp steps)
%d=ReadFepxDataAniso(nprocs,nsteps);
                %
% Read .grain file to get number of elements and grain and phase information
grph=load([fname,'.grain']);
nelem=grph(1,1);
                %
        % Calculate number of steps to print
                nstp=((nf-ns)/nint)+1;
                %
% Remove header from .grains data and repeat for all strain steps
grph(1,:)=[];
        % Repeat grain and phase data to fill all rows
                grph=repmat(grph,nstp,1);
               % size(grph);
                %
                grow=(grph(:,1)==graino);
                ngrow=size(grow,1);
                %
% Change angle convention from Kocks to Bunge and traspose
angB=BungeOfKocks(d.angs(:,:,:),'degrees');
                %
% Calculate start and end rows for all desired displacement steps
% and make orientation array
               angs=[];
               for i=1:nstp
                   ni=ns+nint*(i-1);
                   angles=angB(:,:,ni);
                   angles=angles';
                   angs=[angs;angles];
               end
               nrow=size(angs,1);
               %size(angs)
               %
               % rows=[];
               %for i=ns:nint:nf
%si=i*nelem-nelem+1;
%fi=si+nelem-1;
```

```
                %rowsi=[si:1:fi];
                %rows=[rows;rowsi];
                %end
                %rows=rows;
%selangB=angB(rows,:);
                %nrow=size(selangB,1);
                %
                %
% Print ones and ceros
one(1:nrow)=1;
ones=one';
cero(1:nrow)=0;
ceros=cero';
                %
         % Print element number for all strain steps
el=(1:nelem)';
                eles=repmat(el,nstp,1);
elems=eles;
                %
         % Print strain step for each
                str=[];
                count=0;
                for i=1:nstp
                    if i==1
                        ms=1;
                        mf=nelem;
                        str(ms:mf,1)=ns;
                    else
                        ms=(i-1)*nelem+1;
                        mf=i*nelem;
                        str(ms:mf,1)=ns+nint*(i-1);
                    end
                end
                %
% Put it all together in one single array
array=[angs str grph ceros ones ceros ones elems];
                %
        % Select information relevant to grain chosen by user
                grarray = array(grow,:);
                ngrarray=size(grarray,1);
                %
```

```
        % Build truncated array
                nselgr=ngrarray/nstp;
                trunc(ngrarray,1)=0;
                for i=0:(ngrarray-1)
                    mo=mod(i,nselgr);
                    if (mo>=nstrunc) && (mo<=nftrunc)
                        trunc(i,1)=1;
                    end
                end
                trunc = logical(trunc);
                ntrunc=size(trunc);
                 %
        %Select grain domain selected by the user
                grdomarray=grarray(trunc,:);
 % Write in file. You can have an initial file called tex1.cpt with
 appropriate header on, or you can add the header manually after
tex1cpt=fopen('tex1.cpt','a');
formcpt='%8.2f%8.2f%8.2f%6.0f%6.0f%6.0f%6.0f%6.0f%6.0f%6.0fn';
fprintf(tex1cpt,formcpt,grdomarray');
%
```

Calculate Slip System Activities

It is also of interest to calculate slip system activities for the different slip systems that were implemented in the FEpX code, for both the bridgmanite and the periclase phase. Slip system activity is calculated by considering the slip system shear rates for each element in the aggregate. An average shear rate is calculated for the symmetry equivalent directions that compose a each slip plane, obtaining the average shear rate for the particular slip system at each element. The average shear rate for each system is then averaged over all the elements of the phase in question (bridgmanite or periclase) and is normalized by the number of elements in the phase so the average shear rate is independent of the volume, assuming that all the elements have similar volume. This procedure is done for both phases, once an average shear rate for all the slip systems in phase 1 and phase 2 are obtained for a particular deformation step, the sum of the shear rates of all slip systems of both phases is calculated and used asa normalization constant to obtain the average slip system activity. Where the total activity sums to 1 over both phases. Variations of this script calculates slip system activity for single phase simulations.

```
function data = SlipAct(fname,d,m)
%
```

```
% FUNCTION THAT CALCULATES SLIP SYSTEM ACTIVITY FOR EACH SLIP SYSTEM (INCLUDING
SYMMETRY EQUIVALENT) FOR EACH ELEMENT, GRAIN AND VOLUME PERCENTAGE OVER ALL PHASE
% EVERY DEFORMATION STEP
% INPUTS
% fname : job name
% d : matlab data array created by ReadFepxDataAniso before you run this script.
% m : matlab data array crated by ReadFepxMesh
%
%
% Read number of frames (deformation steps) and number of elements
 nframe = d.nframes;
 nelem = size(m.con,2);
%
%
% Calculate element volume at each frame, reduce to single phase only.
% (NOTE: this only calculates the element volumes at strained states.
% Undeformed element volumes are not calculated.) This is peace of code
% from Matt Kasemer
%elemvol = zeros(nelem,nframes);
%for i = 1:nframes

 %   elemvol(:,i) = CalcElemVolFrame(d.coord(:,:,i),m.con');

%end
%
%
% Group gammadots into symmetry equivalent systems by summing corresponding
% rows. We make a new gammadot array here with size [8,nelem,nframe]. The
% rows we sum depend on what phase the element is in: phase 1 must always
% be the orthorhombic phase (in the BCC place maker in the modified code)
% and has 8 slip systems, MgO must always be phase two (FCC place marker)
% and has only 3 slips systems, the rest of the rows in the array will be
% filled with zeros to avoid asymmetric entries in the array.
%
% Create index for phase 1 and 2
PH1 = m.phases(:)==1;
PH2 = m.phases(:)==2;
%
% Create two separate gammadot arrays for phase 1 and 2.
ph1gammadot = abs(d.gammadot(:,PH1,:));
ph2gammadot = abs(d.gammadot(:,PH2,:));
```

```
%
% Sum gammadots for symmetry equivalent directions to have total shear of
% slip system.
%
% Phase 1
ph1nelem = size(ph1gammadot,2);
slip1ph1 = ph1gammadot(1,:,:);
slip2ph1 = sum(ph1gammadot(2:3,:,:),1);
slip3ph1 = ph1gammadot(4,:,:);
slip4ph1 = sum(ph1gammadot(5:6,:,:),1);
slip5ph1 = ph1gammadot(7,:,:);
slip6ph1 = ph1gammadot(8,:,:);
slip7ph1 = sum(ph1gammadot(9:10,:,:),1);
slip8ph1 = sum(ph1gammadot(11:22,:,:),1);
% Concatenate so we have a list of shear rates per slip systems
data.orthoslip = vertcat(slip1ph1,slip2ph1,slip3ph1,slip4ph1,slip5ph1,
slip6ph1,slip7ph1,slip8ph1);
% Average over all elements in phase 1 to get average shear rate of slip
avorthoslip = sum(data.orthoslip(:,:,:),2)/ph1nelem;
%
%
% Phase 2
ph2nelem = size(ph2gammadot,2);
slip1ph2 = sum(ph2gammadot(1:12,:,:),1);
slip2ph2 = sum(ph2gammadot(13:18,:,:),1);
slip3ph2 = sum(ph2gammadot(19:24,:,:),1);
% Concatenate so we have shear rates per slip system
data.mgoslip = vertcat(slip1ph2,slip2ph2,slip3ph2);
% Average over all elements in phase 2
avmgoslip = sum(data.mgoslip(:,:,:),2)/ph2nelem;
%
%
% Concatenate ortho and mgo average arrays to have a single column with
% average slip in each slip system of both phases.
data.totslip = vertcat(avorthoslip,avmgoslip);
%
% Add rows to find normalization constant
normalc = sum(data.totslip(:,:,:),1);
totnorm = vertcat(normalc,normalc,normalc,normalc,normalc,normalc,
normalc,normalc,normalc,normalc,normalc);
% Normalize
```

```
data.totslipnorm = data.totslip./totnorm;
% Sum of normalized shear rate per phase to compare total slip between 1&2.
data.ph1tot = sum(data.totslipnorm(1:8,:,:));
data.ph2tot = sum(data.totslipnorm(9:11,:,:));
%
% Create array for printing in file
%
strstpcol = 1:nframe;
printarray0 = permute(vertcat(data.totslipnorm, data.ph1tot, data.ph2tot),
[3 1 2]);
data.printarray = horzcat(strstpcol',printarray0);
% Print info in file
% Open file, print header and formating
slipact=fopen('SlipAct.out','a');
fprintf(slipact, 'Average slip system activity for slip systems of phase 1
(Mode 1-8) and phase 2 (Mode 1-3).n');
fprintf(slipact, '       PHASE 1
           PHASE 2  n');
fprintf(slipact, 'StrStp Mode1   Mode2   Mode3   Mode4   Mode5   Mode6   Mode7
  Mode8   Mode1   Mode2  Mode3  TotPh1  TotPh2n');
formt='%3d%8.2f%8.2f%8.2f%8.2f%8.2f%8.2f%8.2f%8.2f%8.2f%8.2f%8.2f%8.2fn';
for m = 1:nframe
    fprintf(slipact,formt,data.printarray(m,:));
%
```

Appendix B

VPFFT Postprocessing Scripts

All scripts presented here are written in FORTRAN.

Orientation File Segregation

Bash script that separates final orientation file in BEARTEX cpt format into a single file per deformation step up to 90% strain.

```
#!/bin/bash

echo "Enter number of points"
read npts
ones=$(expr 7 + 8 \* $npts / 2 + 1)
onef=$(expr 7 + 10 \* $npts / 2)
twos=$(expr 7 + 18 \* $npts / 2 + 1)
twof=$(expr 7 + 20 \* $npts / 2)
threes=$(expr 7 + 28 \* $npts / 2 + 1)
threef=$(expr 7 + 30 \* $npts / 2)
fours=$(expr 7 + 38 \* $npts / 2 + 1)
fourf=$(expr 7 + 40 \* $npts / 2)
fives=$(expr 7 + 48 \* $npts / 2 + 1)
fivef=$(expr 7 + 50 \* $npts / 2)
sixs=$(expr 7 + 58 \* $npts / 2 + 1)
sixf=$(expr 7 + 60 \* $npts / 2)
sevens=$(expr 7 + 68 \* $npts / 2 + 1)
sevenf=$(expr 7 + 70 \* $npts / 2)
eights=$(expr 7 + 78 \* $npts / 2 + 1)
eightf=$(expr 7 + 80 \* $npts / 2)
nines=$(expr 7 + 88 \* $npts / 2 + 1)
```

```
ninef=$(expr 7 + 90 \* $npts / 2)

Sed -n "1,7p" tex1.cpt >> tex1_10.cpt
Sed -n "1,7p" tex1.cpt >> tex1_20.cpt
Sed -n "1,7p" tex1.cpt >> tex1_30.cpt
Sed -n "1,7p" tex1.cpt >> tex1_40.cpt
Sed -n "1,7p" tex1.cpt >> tex1_50.cpt
Sed -n "1,7p" tex1.cpt >> tex1_60.cpt
Sed -n "1,7p" tex1.cpt >> tex1_70.cpt
Sed -n "1,7p" tex1.cpt >> tex1_80.cpt
Sed -n "1,7p" tex1.cpt >> tex1_90.cpt

Sed -n "$ones,$onef"p tex1.cpt >> tex1_10.cpt
Sed -n "$twos,$twof"p tex1.cpt >> tex1_20.cpt
Sed -n "$threes,$threef"p tex1.cpt >> tex1_30.cpt
Sed -n "$fours,$fourf"p tex1.cpt >> tex1_40.cpt
Sed -n "$fives,$fivef"p tex1.cpt >> tex1_50.cpt
Sed -n "$sixs,$sixf"p tex1.cpt >> tex1_60.cpt
Sed -n "$sevens,$sevenf"p tex1.cpt >> tex1_70.cpt
Sed -n "$eights,$eightf"p tex1.cpt >> tex1_80.cpt
Sed -n "$nines,$ninef"p tex1.cpt >> tex1_90.cpt
```

Print Orientation File for Selected Grain

Script selects orientations of all voxels in a selected grain. It can print up to 5 consecutive 10% strain steps. The output of this script is used in the PTXX program in BEARTEX to plot pole figures of discrete orientations of the voxels that compose the selected grain.

```
parameter(iline1=196247,iline2=65897)
dimension jgrain(iline1),kgrain(iline2)

    write(*,*) 'What phase number? '
    read(*,*) iph

write(*,*) 'How many 10% strain steps do you want to plot? (max 5)'
    read(*,*) ifile

write(*,*) 'What grain number do you want to plot?'
    read(*,*) igrain
```

```
if (iph.eq.1) then


if (ifile.eq.1) then

open(1,file='tex1_10.cpt',status='old')
open(11,file='trkgrain1_10.cpt',status='unknown')

        write(11,'(A)')'trkgrain1_10.cpt from FFT'
        write(11,'(A)')'Formatted to plot with Beartex'
        write(11,'(A)')'   3    1'
        write(11,'(A)')'     5.363     7.676     5.503      90.0      90.0   90.0'
        write(11,'(A)')'      0.00      5.00      0.00      1'
        write(11,'(A)')' 300    0'
        write(11,'(A)')'B'

read(1,*)
read(1,*)
read(1,*)
read(1,*)
read(1,*)
read(1,*)
read(1,*)

do k=1,iline1
read(1,*)ph,th,om,one,i0,j0,k0,ione,icero,jgrain(iline1),ione,istr

if (jgrain(iline1).eq.igrain) then
write(11,111)ph,th,om,one,i0,j0,k0,ione,icero,jgrain(iline1),ione,istr
111   format(4f7.2,8i5)
endif

if(jgrain(iline1).eq.igrain) icount=icount+1

enddo

write(*,*)'Number of Fourier points for chosen grain =',icount

endif

if (ifile.eq.2) then
```

```
open(1,file='tex1_10.cpt',status='old')
open(2,file='tex1_20.cpt',status='old')
open(12,file='trkgrain1_20.cpt',status='unknown')

        write(12,'(A)')'trkgrain1_20.cpt from FFT'
        write(12,'(A)')'Formatted to plot with Beartex'
        write(12,'(A)')'   3    1'
        write(12,'(A)')'     5.363     7.676     5.503      90.0      90.0   90.0'
        write(12,'(A)')'      0.00      5.00      0.00      1'
        write(12,'(A)')' 300    0'
        write(12,'(A)')'B'

read(1,*)
read(1,*)
read(1,*)
read(1,*)
read(1,*)
read(1,*)
read(1,*)

do k=1,iline1
read(1,*)ph,th,om,one,i0,j0,k0,ione,icero,jgrain(iline1),ione,istr

if (jgrain(iline1).eq.igrain) then
write(12,111)ph,th,om,one,i0,j0,k0,ione,icero,jgrain(iline1),ione,istr
endif

enddo

read(2,*)
read(2,*)
read(2,*)
read(2,*)
read(2,*)
read(2,*)
read(2,*)

do k=1,iline1
read(2,*)ph,th,om,one,i0,j0,k0,ione,icero,jgrain(iline1),ione,istr
```

```
if (jgrain(iline1).eq.igrain) then
write(12,111)ph,th,om,one,i0,j0,k0,ione,icero,jgrain(iline1),ione,istr
endif

if(jgrain(iline1).eq.igrain) icount=icount+1

enddo

write(*,*)'Number of Fourier points for chosen grain =',icount
endif

if (ifile.eq.3) then

open(1,file='tex1_10.cpt',status='old')
open(2,file='tex1_20.cpt',status='old')
open(3,file='tex1_30.cpt',status='old')
open(13,file='trkgrain1_30.cpt',status='unknown')

         write(13,'(A)')'trkgrain1_30.cpt from FFT'
         write(13,'(A)')'Formatted to plot with Beartex'
         write(13,'(A)')'   3    1'
         write(13,'(A)')'     5.363     7.676     5.503      90.0      90.0
90.0'
         write(13,'(A)')'      0.00      5.00      0.00      1'
         write(13,'(A)')' 300    0'
         write(13,'(A)')'B'

read(1,*)
read(1,*)
read(1,*)
read(1,*)
read(1,*)
read(1,*)
read(1,*)

do k=1,iline1
read(1,*)ph,th,om,one,i0,j0,k0,ione,icero,jgrain(iline1),ione,istr

if (jgrain(iline1).eq.igrain) then
write(13,111)ph,th,om,one,i0,j0,k0,ione,icero,jgrain(iline1),ione,istr
endif
```

```
enddo

read(2,*)
read(2,*)
read(2,*)
read(2,*)
read(2,*)
read(2,*)
read(2,*)

do k=1,iline1
read(2,*)ph,th,om,one,i0,j0,k0,ione,icero,jgrain(iline1),ione,istr

if (jgrain(iline1).eq.igrain) then
write(13,111)ph,th,om,one,i0,j0,k0,ione,icero,jgrain(iline1),ione,istr
endif

enddo


read(3,*)
read(3,*)
read(3,*)
read(3,*)
read(3,*)
read(3,*)
read(3,*)

do k=1,iline1
read(3,*)ph,th,om,one,i0,j0,k0,ione,icero,jgrain(iline1),ione,istr

if (jgrain(iline1).eq.igrain) then
write(13,111)ph,th,om,one,i0,j0,k0,ione,icero,jgrain(iline1),ione,istr
endif

if(jgrain(iline1).eq.igrain) icount=icount+1

enddo

write(*,*)'Number of Fourier points for chosen grain =',icount
```

```
endif

if (ifile.eq.4) then

open(1,file='tex1_10.cpt',status='old')
open(2,file='tex1_20.cpt',status='old')
open(3,file='tex1_30.cpt',status='old')
open(4,file='tex1_40.cpt',status='old')
open(14,file='trkgrain1_40.cpt',status='unknown')

         write(14,'(A)')'trkgrain1_40.cpt from FFT'
         write(14,'(A)')'Formatted to plot with Beartex'
         write(14,'(A)')'   3    1'
         write(14,'(A)')'     5.363     7.676     5.503      90.0      90.0
90.0'
         write(14,'(A)')'      0.00      5.00      0.00      1'
         write(14,'(A)')' 300    0'
         write(14,'(A)')'B'

read(1,*)
read(1,*)
read(1,*)
read(1,*)
read(1,*)
read(1,*)
read(1,*)

do k=1,iline1
read(1,*)ph,th,om,one,i0,j0,k0,ione,icero,jgrain(iline1),ione,istr

if (jgrain(iline1).eq.igrain) then
write(14,111)ph,th,om,one,i0,j0,k0,ione,icero,jgrain(iline1),ione,istr
endif

enddo

read(2,*)
read(2,*)
read(2,*)
read(2,*)
read(2,*)
```

```
read(2,*)
read(2,*)

do k=1,iline1
read(2,*)ph,th,om,one,i0,j0,k0,ione,icero,jgrain(iline1),ione,istr

if (jgrain(iline1).eq.igrain) then
write(14,111)ph,th,om,one,i0,j0,k0,ione,icero,jgrain(iline1),ione,istr
endif

enddo


read(3,*)
read(3,*)
read(3,*)
read(3,*)
read(3,*)
read(3,*)
read(3,*)

do k=1,iline1
read(3,*)ph,th,om,one,i0,j0,k0,ione,icero,jgrain(iline1),ione,istr

if (jgrain(iline1).eq.igrain) then
write(14,111)ph,th,om,one,i0,j0,k0,ione,icero,jgrain(iline1),ione,istr
endif

enddo

read(4,*)
read(4,*)
read(4,*)
read(4,*)
read(4,*)
read(4,*)
read(4,*)

do k=1,iline1
read(4,*)ph,th,om,one,i0,j0,k0,ione,icero,jgrain(iline1),ione,istr
```

```
if (jgrain(iline1).eq.igrain) then
write(14,111)ph,th,om,one,i0,j0,k0,ione,icero,jgrain(iline1),ione,istr
endif

if(jgrain(iline1).eq.igrain) icount=icount+1

enddo

write(*,*)'Number of Fourier points for chosen grain =',icount
endif

if (ifile.eq.5) then

open(1,file='tex1_10.cpt',status='old')
open(2,file='tex1_20.cpt',status='old')
open(3,file='tex1_30.cpt',status='old')
open(4,file='tex1_40.cpt',status='old')
open(5,file='tex1_50.cpt',status='old')
open(15,file='trkgrain1_50.cpt',status='unknown')

         write(15,'(A)')'trkgrain1_50.cpt from FFT'
         write(15,'(A)')'Formatted to plot with Beartex'
         write(15,'(A)')'   3    1'
         write(15,'(A)')'     5.363     7.676     5.503      90.0      90.0
90.0'
         write(15,'(A)')'      0.00      5.00      0.00      1'
         write(15,'(A)')' 300    0'
         write(15,'(A)')'B'

read(1,*)
read(1,*)
read(1,*)
read(1,*)
read(1,*)
read(1,*)
read(1,*)

do k=1,iline1
read(1,*)ph,th,om,one,i0,j0,k0,ione,icero,jgrain(iline1),ione,istr

if (jgrain(iline1).eq.igrain) then
```

```
write(15,111)ph,th,om,one,i0,j0,k0,ione,icero,jgrain(iline1),ione,istr
endif

enddo

read(2,*)
read(2,*)
read(2,*)
read(2,*)
read(2,*)
read(2,*)
read(2,*)

do k=1,iline1
read(2,*)ph,th,om,one,i0,j0,k0,ione,icero,jgrain(iline1),ione,istr

if (jgrain(iline1).eq.igrain) then
write(15,111)ph,th,om,one,i0,j0,k0,ione,icero,jgrain(iline1),ione,istr
endif

enddo


read(3,*)
read(3,*)
read(3,*)
read(3,*)
read(3,*)
read(3,*)
read(3,*)

do k=1,iline1
read(3,*)ph,th,om,one,i0,j0,k0,ione,icero,jgrain(iline1),ione,istr

if (jgrain(iline1).eq.igrain) then
write(15,111)ph,th,om,one,i0,j0,k0,ione,icero,jgrain(iline1),ione,istr
endif

enddo

read(4,*)
```

```
read(4,*)
read(4,*)
read(4,*)
read(4,*)
read(4,*)
read(4,*)

do k=1,iline1
read(4,*)ph,th,om,one,i0,j0,k0,ione,icero,jgrain(iline1),ione,istr

if (jgrain(iline1).eq.igrain) then
write(15,111)ph,th,om,one,i0,j0,k0,ione,icero,jgrain(iline1),ione,istr
endif

enddo


read(5,*)
read(5,*)
read(5,*)
read(5,*)
read(5,*)
read(5,*)
read(5,*)

do k=1,iline1
read(5,*)ph,th,om,one,i0,j0,k0,ione,icero,jgrain(iline1),ione,istr

if (jgrain(iline1).eq.igrain) then
write(15,111)ph,th,om,one,i0,j0,k0,ione,icero,jgrain(iline1),ione,istr
endif

if(jgrain(iline1).eq.igrain) icount=icount+1

enddo

write(*,*)'Number of Fourier points for chosen grain =',icount
endif
endif

if (iph.eq.2) then
```

```
if (ifile.eq.1) then

open(1,file='tex2_10.cpt',status='old')
open(11,file='trkgrain2_10.cpt',status='unknown')

        write(11,'(A,i6)')'trkgrain2_10.cpt from FFT'
        write(11,'(A)')'Formatted to plot with Beartex'
        write(11,'(A)')'   7    1'
        write(11,'(A)')'      1.00      1.00      1.00      90.0      90.0   90.0'
        write(11,'(A)')'      0.00      5.00      0.00      1'
        write(11,'(A)')'1337    0'
        write(11,'(A)')'B'

read(1,*)
read(1,*)
read(1,*)
read(1,*)
read(1,*)
read(1,*)
read(1,*)

do k=1,iline2
read(1,*)ph,th,om,one,i0,j0,k0,ione,icero,jgrain(iline2),ione,istr

if (jgrain(iline2).eq.igrain) then
write(11,111)ph,th,om,one,i0,j0,k0,ione,icero,jgrain(iline2),ione,istr
endif

if(jgrain(iline2).eq.igrain) icount=icount+1

enddo

write(*,*)'Number of Fourier points for chosen grain =',icount

endif

if (ifile.eq.2) then

open(1,file='tex2_10.cpt',status='old')
open(2,file='tex2_20.cpt',status='old')
```

```
open(12,file='trkgrain2_20.cpt',status='unknown')

        write(12,'(A,i6)')'trkgrain2_20.cpt from FFT'
        write(12,'(A)')'Formatted to plot with Beartex'
        write(12,'(A)')'   7    1'
        write(12,'(A)')'      1.00      1.00      1.00      90.0      90.0   90.0'
        write(12,'(A)')'      0.00      5.00      0.00      1'
        write(12,'(A)')'1337    0'
        write(12,'(A)')'B'

read(1,*)
read(1,*)
read(1,*)
read(1,*)
read(1,*)
read(1,*)
read(1,*)

do k=1,iline2
read(1,*)ph,th,om,one,i0,j0,k0,ione,icero,jgrain(iline2),ione,istr

if (jgrain(iline2).eq.igrain) then
write(12,111)ph,th,om,one,i0,j0,k0,ione,icero,jgrain(iline2),ione,istr
endif

enddo

read(2,*)
read(2,*)
read(2,*)
read(2,*)
read(2,*)
read(2,*)
read(2,*)

do k=1,iline2
read(2,*)ph,th,om,one,i0,j0,k0,ione,icero,jgrain(iline2),ione,istr

if (jgrain(iline2).eq.igrain) then
write(12,111)ph,th,om,one,i0,j0,k0,ione,icero,jgrain(iline2),ione,istr
endif
```

```
if(jgrain(iline2).eq.igrain) icount=icount+1

enddo

write(*,*)'Number of Fourier points for chosen grain =',icount
endif

if (ifile.eq.3) then

open(1,file='tex2_10.cpt',status='old')
open(2,file='tex2_20.cpt',status='old')
open(3,file='tex2_30.cpt',status='old')
open(13,file='trkgrain2_30.cpt',status='unknown')

        write(13,'(A,i6)')'trkgrain2_30.cpt from FFT'
        write(13,'(A)')'Formatted to plot with Beartex'
        write(13,'(A)')'   7    1'
        write(13,'(A)')'      1.00      1.00      1.00      90.0      90.0   90.0'
        write(13,'(A)')'      0.00      5.00      0.00      1'
        write(13,'(A)')'1337    0'
        write(13,'(A)')'B'

read(1,*)
read(1,*)
read(1,*)
read(1,*)
read(1,*)
read(1,*)
read(1,*)

do k=1,iline2
read(1,*)ph,th,om,one,i0,j0,k0,ione,icero,jgrain(iline2),ione,istr

if (jgrain(iline2).eq.igrain) then
write(13,111)ph,th,om,one,i0,j0,k0,ione,icero,jgrain(iline2),ione,istr
endif

enddo

read(2,*)
```

```
read(2,*)
read(2,*)
read(2,*)
read(2,*)
read(2,*)
read(2,*)

do k=1,iline2
read(2,*)ph,th,om,one,i0,j0,k0,ione,icero,jgrain(iline2),ione,istr

if (jgrain(iline2).eq.igrain) then
write(13,111)ph,th,om,one,i0,j0,k0,ione,icero,jgrain(iline2),ione,istr
endif

enddo


read(3,*)
read(3,*)
read(3,*)
read(3,*)
read(3,*)
read(3,*)
read(3,*)

do k=1,iline2
read(3,*)ph,th,om,one,i0,j0,k0,ione,icero,jgrain(iline2),ione,istr

if (jgrain(iline2).eq.igrain) then
write(13,111)ph,th,om,one,i0,j0,k0,ione,icero,jgrain(iline2),ione,istr
endif

if(jgrain(iline2).eq.igrain) icount=icount+1

enddo

write(*,*)'Number of Fourier points for chosen grain =',icount
endif

if (ifile.eq.4) then
```

```
open(1,file='tex2_10.cpt',status='old')
open(2,file='tex2_20.cpt',status='old')
open(3,file='tex2_30.cpt',status='old')
open(4,file='tex2_40.cpt',status='old')
open(14,file='trkgrain2_40.cpt',status='unknown')

        write(14,'(A,i6)')'trkgrain2_40.cpt from FFT'
        write(14,'(A)')'Formatted to plot with Beartex'
        write(14,'(A)')'   7    1'
        write(14,'(A)')'      1.00      1.00      1.00      90.0      90.0   90.0'
        write(14,'(A)')'      0.00      5.00      0.00      1'
        write(14,'(A)')'1337    0'
        write(14,'(A)')'B'

read(1,*)
read(1,*)
read(1,*)
read(1,*)
read(1,*)
read(1,*)
read(1,*)

do k=1,iline2
read(1,*)ph,th,om,one,i0,j0,k0,ione,icero,jgrain(iline2),ione,istr

if (jgrain(iline2).eq.igrain) then
write(14,111)ph,th,om,one,i0,j0,k0,ione,icero,jgrain(iline2),ione,istr
endif

enddo

read(2,*)
read(2,*)
read(2,*)
read(2,*)
read(2,*)
read(2,*)
read(2,*)

do k=1,iline2
read(2,*)ph,th,om,one,i0,j0,k0,ione,icero,jgrain(iline2),ione,istr
```

```
if (jgrain(iline2).eq.igrain) then
write(14,111)ph,th,om,one,i0,j0,k0,ione,icero,jgrain(iline2),ione,istr
endif

enddo


read(3,*)
read(3,*)
read(3,*)
read(3,*)
read(3,*)
read(3,*)
read(3,*)

do k=1,iline2
read(3,*)ph,th,om,one,i0,j0,k0,ione,icero,jgrain(iline2),ione,istr

if (jgrain(iline2).eq.igrain) then
write(14,111)ph,th,om,one,i0,j0,k0,ione,icero,jgrain(iline2),ione,istr
endif

enddo

read(4,*)
read(4,*)
read(4,*)
read(4,*)
read(4,*)
read(4,*)
read(4,*)

do k=1,iline2
read(4,*)ph,th,om,one,i0,j0,k0,ione,icero,jgrain(iline2),ione,istr

if (jgrain(iline2).eq.igrain) then
write(14,111)ph,th,om,one,i0,j0,k0,ione,icero,jgrain(iline2),ione,istr
endif

if(jgrain(iline2).eq.igrain) icount=icount+1
```

```
enddo

write(*,*)'Number of Fourier points for chosen grain =',icount
endif

if (ifile.eq.5) then

open(1,file='tex2_10.cpt',status='old')
open(2,file='tex2_20.cpt',status='old')
open(3,file='tex2_30.cpt',status='old')
open(4,file='tex2_40.cpt',status='old')
open(5,file='tex2_50.cpt',status='old')
open(15,file='trkgrain2_50.cpt',status='unknown')

        write(15,'(A,i6)')'trkgrain2_50.cpt from FFT'
        write(15,'(A)')'Formatted to plot with Beartex'
        write(15,'(A)')'   7    1'
        write(15,'(A)')'      1.00      1.00      1.00      90.0      90.0   90.0'
        write(15,'(A)')'      0.00      5.00      0.00      1'
        write(15,'(A)')'1337    0'
        write(15,'(A)')'B'

read(1,*)
read(1,*)
read(1,*)
read(1,*)
read(1,*)
read(1,*)
read(1,*)

do k=1,iline2
read(1,*)ph,th,om,one,i0,j0,k0,ione,icero,jgrain(iline2),ione,istr

if (jgrain(iline2).eq.igrain) then
write(15,111)ph,th,om,one,i0,j0,k0,ione,icero,jgrain(iline2),ione,istr
endif

enddo

read(2,*)
```

```
read(2,*)
read(2,*)
read(2,*)
read(2,*)
read(2,*)
read(2,*)

do k=1,iline2
read(2,*)ph,th,om,one,i0,j0,k0,ione,icero,jgrain(iline2),ione,istr

if (jgrain(iline2).eq.igrain) then
write(15,111)ph,th,om,one,i0,j0,k0,ione,icero,jgrain(iline2),ione,istr
endif

enddo


read(3,*)
read(3,*)
read(3,*)
read(3,*)
read(3,*)
read(3,*)
read(3,*)

do k=1,iline2
read(3,*)ph,th,om,one,i0,j0,k0,ione,icero,jgrain(iline2),ione,istr

if (jgrain(iline2).eq.igrain) then
write(15,111)ph,th,om,one,i0,j0,k0,ione,icero,jgrain(iline2),ione,istr
endif

enddo

read(4,*)
read(4,*)
read(4,*)
read(4,*)
read(4,*)
read(4,*)
read(4,*)
```

```
do k=1,iline2
read(4,*)ph,th,om,one,i0,j0,k0,ione,icero,jgrain(iline2),ione,istr

if (jgrain(iline2).eq.igrain) then
write(15,111)ph,th,om,one,i0,j0,k0,ione,icero,jgrain(iline2),ione,istr
endif

enddo


read(5,*)
read(5,*)
read(5,*)
read(5,*)
read(5,*)
read(5,*)
read(5,*)

do k=1,iline2
read(5,*)ph,th,om,one,i0,j0,k0,ione,icero,jgrain(iline2),ione,istr

if (jgrain(iline2).eq.igrain) then
write(15,111)ph,th,om,one,i0,j0,k0,ione,icero,jgrain(iline2),ione,istr
endif

if(jgrain(iline2).eq.igrain) icount=icount+1

enddo

write(*,*)'Number of Fourier points for chosen grain =',icount
endif
endif


                 END
```

Select a Domain of a Grain for Plotting PTXX Plots

Prints discrete orientations of a selected domain in a grain for plotting pole figures in PTXX. Orientations of the selected domain can be plotted for consecutive strain steps.

```
  parameter(npts1=64,npts2=64,npts3=64,lines1=196247,lines2=65897,
  ipoints1=10,ipoints2=9)
dimension :: ix1(ipoints1),ix2(ipoints2)
dimension :: i1(ipoints1),j1(ipoints1),k1(ipoints1)
dimension :: i2(ipoints2),j2(ipoints2),k2(ipoints2)

! Writes in .cpt file orientations of a certain domain at each deformation step

    write(*,*) 'What phase number? '
    read(*,*) iph

    write(*,*) 'How many strain steps? '
    read(*,*) istrain

if (iph.eq.1) then

open(1,file='tex1.cpt',status='old')
open(2,file='rows1.in',status='old')
open(11,file='ordom_1.cpt',status='unknown')


         write(11,'(A)')'ordom_1.cpt from FFT'
         write(11,'(A)')'Formatted to plot with Beartex'
         write(11,'(A)')'   3    1'
         write(11,'(A)')'     5.363     7.676     5.503      90.0      90.0
90.0'
         write(11,'(A)')'      0.00      5.00      0.00      1'
         write(11,'(A)')' 300    0'
         write(11,'(A)')'B'


do k=1,istrain

REWIND 2

do i=1,ipoints1
```

```
REWIND 1

do iii=1,(7+lines1*(k-1))
read(1,*)
enddo


icount=0

read(2,*)ix1(i)

do kk=1,npts3
do jj=1,npts2
do ii=1,npts1

icount=icount+1

if (icount.eq.(ix1(i)+1)) then
i1(i)=ii
j1(i)=jj
k1(i)=kk
endif

enddo
enddo
enddo

do j=1,lines1

read(1,*)ph,th,om,one,i0,j0,k0,ione,icero,jgrain,ione,istr

if (i0.eq.i1(i)) then
if (j0.eq.j1(i)) then
if (k0.eq.k1(i)) then

write(11,111)ph,th,om,one,i0,j0,k0,ione,icero,jgrain,ione,istr
111   format(4f7.2,8i5)

endif
endif
```

```
endif
enddo

enddo

enddo

else if (iph.eq.2) then

open(3,file='tex2.cpt',status='old')
open(4,file='rows2.in',status='old')
open(12,file='ordom_2.cpt',status='unknown')


        write(12,'(A,i6)')'ordom_2.cpt from FFT'
        write(12,'(A)')'Formatted to plot with Beartex'
        write(12,'(A)')'   7    1'
        write(12,'(A)')'      1.00      1.00      1.00      90.0      90.0   90.0'
        write(12,'(A)')'      0.00      5.00      0.00      1'
        write(12,'(A)')'1337    0'
        write(12,'(A)')'B'


do k=1,istrain

REWIND 4

do i=1,ipoints2

REWIND 3

do iii=1,(7+lines2*(k-1))
read(3,*)
enddo


icount=0

read(4,*)ix2(i)

do kk=1,npts3
```

```
do jj=1,npts2
do ii=1,npts1

icount=icount+1

if (icount.eq.(ix2(i)+1)) then
i2(i)=ii
j2(i)=jj
k2(i)=kk
endif

enddo
enddo
enddo

do j=1,lines2

read(3,*)ph,th,om,one,i0,j0,k0,ione,icero,jgrain,ione,istr

if (i0.eq.i2(i)) then
if (j0.eq.j2(i)) then
if (k0.eq.k2(i)) then

write(12,111)ph,th,om,one,i0,j0,k0,ione,icero,jgrain,ione,istr

endif
endif
endif
enddo

enddo

enddo

endif


END
```

Track Orientation of Individual Voxels

Selects orientations of individual voxels to plot pole figures using in PTXX. The orientation of the selected voxel are printed for a consecutive number of strain steps selected by the user.

```
  parameter(npts1=64,npts2=64,npts3=64,lines1=196247,lines2=65897)

! Creates a file that has orientations of a single voxel at each deformation step

    write(*,*) 'What phase number? '
    read(*,*) iph

    write(*,*) 'Cell number from paraview '
    read(*,*) ix

    write(*,*) 'How many strain steps? '
    read(*,*) istrain

if (iph.eq.1) then

open(1,file='tex1.cpt',status='old')
open(11,file='sinvoxor_1.cpt',status='unknown')

read(1,*)
read(1,*)
read(1,*)
read(1,*)
read(1,*)
read(1,*)
read(1,*)

         write(11,'(A)')'sinvoxor_1.cpt from FFT'
         write(11,'(A)')'Formatted to plot with Beartex'
         write(11,'(A)')'   3    1'
         write(11,'(A)')'     5.363     7.676     5.503      90.0      90.0
90.0'
         write(11,'(A)')'      0.00      5.00      0.00      1'
         write(11,'(A)')' 300    0'
         write(11,'(A)')'B'

do k=1,istrain
```

```
do kk=1,npts3
do jj=1,npts2
do ii=1,npts1

icount=icount+1

if ((ix+1).eq.icount) then
i1=ii
j1=jj
k1=kk
endif

enddo
enddo
enddo

do j=1,lines1
read(1,*)ph,th,om,one,i0,j0,k0,ione,icero,jgrain,ione,istr
if (i0.eq.i1) then
if (j0.eq.j1) then
if (k0.eq.k1) then
write(11,111)ph,th,om,one,i0,j0,k0,ione,icero,jgrain,ione,istr
111   format(4f7.2,8i5)
endif
endif
endif
enddo
enddo


else if (iph.eq.2) then

open(2,file='tex2.cpt',status='old')
open(12,file='sinvoxor_2.cpt',status='unknown')

read(2,*)
read(2,*)
read(2,*)
read(2,*)
read(2,*)
```

```
read(2,*)
read(2,*)

        write(12,'(A,i6)')'sinvoxor_2.cpt from FFT'
        write(12,'(A)')'Formatted to plot with Beartex'
        write(12,'(A)')'   7    1'
        write(12,'(A)')'      1.00      1.00      1.00      90.0      90.0   90.0'
        write(12,'(A)')'      0.00      5.00      0.00      1'
        write(12,'(A)')'1337    0'
        write(12,'(A)')'B'

do k=1,istrain

do kk=1,npts3
do jj=1,npts2
do ii=1,npts1

icount=icount+1

if (icount.eq.(ix+1)) then
i1=ii
j1=jj
k1=kk
endif

enddo
enddo
enddo

do j=1,lines2
read(2,*)ph,th,om,one,i0,j0,k0,ione,icero,jgrain,ione,istr
if (i0.eq.i1) then
if (j0.eq.j1) then
if (k0.eq.k1) then
write(12,111)ph,th,om,one,i0,j0,k0,ione,icero,jgrain,ione,istr
endif
endif
endif
enddo

enddo
```

```
endif

END
```

Classification of Voxels as a Function of their Neighborhood

Prints a file with the values of the stress or strain rate tensor for each Fourier point. A tag is added to each voxel to characterize if they are interior voxels, at grain boundaries with phase 1 or at grain boundaries with phase 2. The output of this script is used by a mathematica notebook to plot strain rate distributions.

```
  parameter(npts1=64,npts2=64,npts3=64)
dimension :: ngr(npts1,npts2,npts3),iph(npts1,npts2,npts3)
dimension :: igba(3,3,3)


write(*,*) 'What do you want to plot?'
write(*,*) '1 : Stress'
write(*,*) '2 : Strain rate'
read(*,*) iplot


if(iplot.eq.1) then

open(1,file='sfield.out',status='old')
open(11,file='sfieldstat.out',status='unknown')
write(11,'(A)') 'x    y    z  ngr   ph   GBt   str11       str22        str33
      str23       str13       str12'

read(1,*)
read(1,*)

do k=1,npts3
do j=1,npts2
do i=1,npts1

read(1,111) i0, j0, k0, ngr(i,j,k), iph(i,j,k), str11, str22, str33, str23, str13,
str12
```

```
111   format(5i5,6f12.5)

enddo
enddo
enddo

REWIND 1

read(1,*)
read(1,*)


do k=1,npts3
do j=1,npts2
do i=1,npts1

do kk=1,3
kkk=k+(kk-2)
do jj=1,3
jjj=j+(jj-2)
do ii=1,3
iii=i+(ii-2)


if(kkk<1) kkk=npts3
if(kkk>npts3) kkk=1
if(jjj<1) jjj=npts3
if(jjj>npts2) jjj=1
if(iii<1) iii=npts3
if(iii>npts3) iii=1


if(ngr(iii,jjj,kkk).eq.ngr(i,j,k)) then
igba(ii,jj,kk)=0

else if (ngr(iii,jjj,kkk).ne.ngr(i,j,k)) then

if(iph(iii,jjj,kkk).eq.1) then
igba(ii,jj,kk)=1

else if (iph(iii,jjj,kkk).eq.2) then
```

```
igba(ii,jj,kk)=2
endif
endif


enddo
enddo
enddo

igbt=MAXVAL(igba)

read(1,111) i0, j0, k0, ngr(i,j,k), iph(i,j,k), str11, str22, str33, str23, str13,
str12

write(11,112) i, j, k, ngr(i,j,k), iph(i,j,k), igbt, str11, str22, str33, str23,
str13, str12
112   format(6i5,6f12.5)

enddo
enddo
enddo

endif


END
```

Calculating and Plotting σ_{33} Strain Rate Distributions

Following *Mathematica* script calculates a smooth kernel distribution of the σ_{33} component of the strain rate tensor and plots the probability density function of this quantity. I uses as input the stressdist.out file that is outputed by the script presented above. The input file contains information of the voxel neighborhood, enabling an analysis of the distributions of different types of voxels for the 6 simulations performed.

```
  Plot Distribution of Stress of Grain Bounadry or Non-Gb Voxels.
  All microstructures
Plot Distibution of Stress of Specific Voxels. Core Structure
import stress field data
```

```
craw=Import["/Users/Loet/Documents/VPFFT/LANL_2014/3_001_110
  _Pv_110_-110MgO_30strain/Core_30strain_001_110_Pv/StrainRateStats
  /dfieldstat.out","Table"];
Length[craw]
262145
Remove header
craw2=Rest[craw];
Length[craw2]
262144
Calculate distribution for all voxels
cd33all = craw2[[All,9]];
Length[cd33all]
262144
cd33alldist=SmoothKernelDistribution[cd33all]
DataDistribution[<<SmoothKernel>>,{262144}]
DataDistribution[<<"SmoothKernel">>,{262144}]

DataDistribution[<<SmoothKernel>>,{262144}]
cp33all=Plot[PDF[cd33alldist,x],{x,-10,10},PlotRange->All,
  PlotStyle->{Blue,Thick},PlotLegends->"edot33_all",AxesOrigin->
  {0,0},LabelStyle->{FontFamily-> "Arial",FontSize->24,FrameLabel->
    {"StrainRate","PDF"}},Frame->{{True,False},{True,False}},Axes->False,
  TicksStyle -> Thickness[0.1]]
Extract all rows that have grain boundaries with phase 2
cgb2=craw2[[Flatten@Position[craw2[[All,6]],2],All]];
Length[cgb2]
128107
Extract voxels from phase 1 that have grain boundaries with phase 2
cgb12=cgb2[[Flatten@Position[cgb2[[All,5]],1],All]];
Length[cgb12]
69601
c1112=cgb12[[All,9]];
Length[c1112]
69601
ListPlot[c1112,PlotRange->All]
Histogram[c1112,{.005},"Probability",ImageSize->Large]
cd1112=SmoothKernelDistribution[c1112]
DataDistribution[<<SmoothKernel>>,{69601}]
cp1112=Plot[PDF[cd1112,x],{x,-10,10},PlotRange->All,PlotStyle->{Blue,Thick
  },PlotLegends->"edot11_12",AxesOrigin->{0,0},LabelStyle->{FontFamily->
    "Arial",FontSize->24,FrameLabel->{"Strain
```

```
Rate","PDF"}},Frame->{{True,False},{True,False}},Axes->False,TicksStyle
  ->Thickness[0.1]]
Extract voxels from phase 2 that have grain boundaries with phase 2
cgb22=cgb2[[Flatten@Position[cgb2[[All,5]],2],All]];
Length[cgb22]
58506
c1122=cgb22[[All,9]];
cd1122=SmoothKernelDistribution[c1122]
DataDistribution[<<SmoothKernel>>,{58506}]
cp1122=Plot[PDF[cd1122,x],{x,-10,10},PlotRange->All,PlotStyle->
  {Blue,Thick},PlotLegends->"c11_22",AxesOrigin->{0,0},LabelStyle->
  {FontFamily-> "Arial",FontSize->24,FrameLabel->{"Strain
Rate","PDF"}},Frame->{{True,False},{True,False}},Axes->False]
Extract all rows that have grain boundaries with phase 1
cgb1=craw2[[Flatten@Position[craw2[[All,6]],1],All]];
Length[cgb1]
112557
Extract voxels from phase 2 that have grain boundaries with phase 1
cgb21=cgb1[[Flatten@Position[cgb1[[All,5]],2],All]];
Length[cgb21]
5808
c1121=cgb21[[All,9]];
cd1121=SmoothKernelDistribution[c1121];
cp1121=Plot[PDF[cd1121,x],{x,-10,10},PlotRange->All,PlotStyle->
  {Blue,Thick},PlotLegends->"c11_21",AxesOrigin->{0,0},LabelStyle->
  {FontFamily-> "Arial",FontSize->24,FrameLabel->{"Strain
      Rate","PDF"}},Frame->{{True,False},{True,False}},Axes->False]
Extract voxels from phase 1 that have grain boundaries with phase 1
cgb11=cgb1[[Flatten@Position[cgb1[[All,5]],1],All]];
Length[cgb11]
106749
c1111=cgb11[[All,9]];
cd1111=SmoothKernelDistribution[c1111];
cp1111=Plot[PDF[cd1111,x],{x,-10,10},PlotRange->All,PlotStyle->
  {Blue,Thick},PlotLegends->"c11_11",AxesOrigin->{0,0},LabelStyle->
  {FontFamily-> "Arial",FontSize->24,FrameLabel->{"Strain
      Rate","PDF"}},Frame->{{True,False},{True,False}},Axes->False]
Extract all rows that are not in grain boundaries
cgb0=craw2[[Flatten@Position[craw2[[All,6]],0],All]];
Length[cgb0]
21480
```

```
Length[cgb1]+Length[cgb0]+Length[cgb2]
262144
Extract voxels that are within grains of phase 1, no grain boundaries
cgb01=cgb0[[Flatten@Position[cgb0[[All,5]],1],All]];
Length[cgb01]
20267
c1110=cgb01[[All,9]];
cd1110=SmoothKernelDistribution[c1110];
cp1110=Plot[PDF[cd1110,x],{x,-10,10},PlotRange->All,PlotStyle->
  {Blue,Thick},PlotLegends->"c11_10",AxesOrigin->{0,0},LabelStyle->
  {FontFamily-> "Arial",FontSize->24,FrameLabel->{"Strain
      Rate","PDF"}},Frame->{{True,False},{True,False}},Axes->False]
Extract voxels that are within grains of phase 2, no grain boundaries
cgb02=cgb0[[Flatten@Position[cgb0[[All,5]],2],All]];
Length[cgb02]
1213
c1120=cgb02[[All,9]];
cd1120=SmoothKernelDistribution[c1120];
cp1120=Plot[PDF[cd1110,x],{x,-10,10},PlotRange->All,PlotStyle->
  {Blue,Thick},PlotLegends->"c11_20",AxesOrigin->{0,0},LabelStyle->
  {FontFamily-> "Arial",FontSize->24,FrameLabel->{"Strain
Rate","PDF"}},Frame->{{True,False},{True,False}},Axes->False]
Plot all together
Show[cp1112,cp1122,cp1121,cp1110,cp1120,cp1111,PlotRange->All]
Show[cp1112,cp1110,cp1120,cp1111,PlotRange->All]
Show[cp1122,cp1121,PlotRange->All]
Plot Distribution of Stress of Specific Voxels. Percolate Structure
import stress field data
praw=Import["/Users/Loet/Documents/VPFFT/LANL_2014/3_001_110_Pv_
  110_-110MgO_30strain/Percolate_30strain/StrainRateDist/dfieldstat.out"
  ,"Table"];
Length[praw]
262145
Remove header
praw2=Rest[praw];
Length[praw2]
262144
Calculate distribution for all voxels
pd33all = praw2[[All,9]];
Length[pd33all]
262144
```

```
pd33alldist=SmoothKernelDistribution[pd33all]
DataDistribution[<<SmoothKernel>>,{262144}]
DataDistribution[<<"SmoothKernel">>,{262144}]

DataDistribution[<<SmoothKernel>>,{262144}]
pp33all=Plot[PDF[pd33alldist,x],{x,-10,10},PlotRange->All,PlotStyle->
  {Green,Thick},PlotLegends->"edot33_all",AxesOrigin->{0,0},LabelStyle->
  {FontFamily-> "Arial",FontSize->24,FrameLabel->{"Strain
      Rate","PDF"}},Frame->{{True,False},{True,False}},Axes->False,TicksStyle
  -> Thickness[0.1]]
Extract all rows that have grain boundaries with phase 2
pgb2=praw2[[Flatten@Position[praw2[[All,6]],2],All]];
Length[pgb2]
126474
Extract voxels from phase 1 that have grain boundaries with phase 2
pgb12=pgb2[[Flatten@Position[pgb2[[All,5]],1],All]];
Length[pgb12]
94523
p1112=pgb12[[All,9]];
Length[p1112]
94523
ListPlot[p1112,PlotRange->All]
Histogram[p1112,{.005},"Probability",ImageSize->Large]
pd1112=SmoothKernelDistribution[p1112]
DataDistribution[<<SmoothKernel>>,{94523}]
pp1112=Plot[PDF[pd1112,x],{x,-10,10},PlotRange->All,PlotStyle->
  {Green,Thick},PlotLegends->"pedot11_12",LabelStyle->{FontFamily->
    "Arial",FontSize->24,FrameLabel->{"Strain
      Rate","PDF"}},Frame->{{True,False},{True,False}},Axes->False]
Extract voxels from phase 2 that have grain boundaries with phase 2
pgb22=pgb2[[Flatten@Position[pgb2[[All,5]],2],All]];
Length[pgb22]
31951
p1122=pgb22[[All,9]];
pd1122=SmoothKernelDistribution[p1122];
pp1122=Plot[PDF[pd1122,x],{x,-10,10},PlotRange->All,PlotStyle->
  {Green,Thick},PlotLegends->"p11_22",LabelStyle->{FontFamily->
    "Arial",FontSize->24,FrameLabel->{"Strain
      Rate","PDF"}},Frame->{{True,False},{True,False}},Axes->False]
Extract all rows that have grain boundaries with phase 1
pgb1=praw2[[Flatten@Position[praw2[[All,6]],1],All]];
```

```
Length[pgb1]
33946
Extract voxels from phase 2 that have grain boundaries with phase 1
pgb21=pgb1[[Flatten@Position[pgb1[[All,5]],2],All]];
Length[pgb21]
33946
p1121=pgb21[[All,9]];
pd1121=SmoothKernelDistribution[p1121];
pp1121=Plot[PDF[pd1121,x],{x,-10,10},PlotRange->All,PlotStyle->
  {Green,Thick},PlotLegends->"p11_21",LabelStyle->{FontFamily->
    "Arial",FontSize->24,FrameLabel->{"Strain
      Rate","PDF"}},Frame->{{True,False},{True,False}},Axes->False]
Extract all rows that are not in grain boundaries
pgb0=praw2[[Flatten@Position[praw2[[All,6]],0],All]];
Length[pgb0]
101724
Length[pgb1]+Length[pgb0]+Length[pgb2]
262144
Extract voxels that are within grains of phase 1, no grain boundaries
pgb01=pgb0[[Flatten@Position[pgb0[[All,5]],1],All]];
Length[pgb01]
101724
p1110=pgb01[[All,9]];
pd1110=SmoothKernelDistribution[p1110];
pp1110=Plot[PDF[pd1110,x],{x,-10,10},PlotRange->All,PlotStyle->
  {Green,Thick},PlotLegends->"p11_10",LabelStyle->{FontFamily->
    "Arial",FontSize->24,FrameLabel->{"Strain
      Rate","PDF"}},Frame->{{True,False},{True,False}},Axes->False]
Extract voxels that are within grains of phase 2, no grain boundaries
pgb02=pgb0[[Flatten@Position[pgb0[[All,5]],2],All]];
Length[pgb02]
0
Show[pp1112,pp1122,pp1121,pp1110,PlotRange->All]
Plot Distribution of Stress of Specific Voxels. Random Structure
Import stress field data
rraw=Import["/Users/Loet/Documents/VPFFT/LANL_2014/3_001_110_Pv_
  110_-110MgO_30strain/Random_30strain_001_110_Pv/StrainRateStats/
  dfieldstat.out","Table"];
Length[rraw]
262145
Remove header
```

```
rraw2=Rest[rraw];
Length[rraw2]
262144
Calculate distribution for all voxels
rd33all = rraw2[[All,9]];
Length[rd33all]
262144
rd33alldist=SmoothKernelDistribution[rd33all]
DataDistribution[<<SmoothKernel>>,{262144}]
DataDistribution[<<"SmoothKernel">>,{262144}]

DataDistribution[<<SmoothKernel>>,{262144}]
rp33all=Plot[PDF[rd33alldist,x],{x,-10,10},PlotRange->All,PlotStyle->
  {Purple,Thick},PlotLegends->"edot33_all",AxesOrigin->{0,0},LabelStyle->
  {FontFamily-> "Arial",FontSize->24,FrameLabel->{"Strain
      Rate","PDF"}},Frame->{{True,False},{True,False}},Axes->False,TicksStyle
  -> Thickness[0.1]]
Extract all rows that have grain boundaries with phase 2
rgb2=rraw2[[Flatten@Position[rraw2[[All,6]],2],All]];
Length[rgb2]
112213
Extract voxels from phase 1 that have grain boundaries with phase 2
rgb12=rgb2[[Flatten@Position[rgb2[[All,5]],1],All]];
Length[rgb12]
52839
r1112=rgb12[[All,9]];
Length[r1112]
52839
ListPlot[r1112,PlotRange->All]
Histogram[r1112,{.005},"Probability",ImageSize->Large]
rd1112=SmoothKernelDistribution[r1112]
DataDistribution[<<SmoothKernel>>,{52839}]
rp1112=Plot[PDF[rd1112,x],{x,-10,10},PlotRange->All,PlotStyle->
  {Purple,Thick},PlotLegends->"r11_12",AxesOrigin->{0,0},LabelStyle->
  {FontFamily-> "Arial",FontSize->24,FrameLabel->{"Strain
      Rate","PDF"}},Frame->{{True,False},{True,False}},Axes->False]
Extract voxels from phase 2 that have grain boundaries with phase 2
rgb22=rgb2[[Flatten@Position[rgb2[[All,5]],2],All]];
Length[rgb22]
59374
r1122=rgb22[[All,9]];
```

```
rd1122=SmoothKernelDistribution[r1122]
DataDistribution[<<SmoothKernel>>,{59374}]
rp1122=Plot[PDF[rd1122,x],{x,-10,10},PlotRange->All,PlotStyle->
  {Purple,Thick},PlotLegends->"r11_22",AxesOrigin->{0,0},LabelStyle->
  {FontFamily-> "Arial",FontSize->24,FrameLabel->{"Strain
      Rate","PDF"}},Frame->{{True,False},{True,False}},Axes->False]
Extract all rows that have grain boundaries with phase 1
rgb1=rraw2[[Flatten@Position[rraw2[[All,6]],1],All]];
Length[rgb1]
93242
Extract voxels from phase 2 that have grain boundaries with phase 1
rgb21=rgb1[[Flatten@Position[rgb1[[All,5]],2],All]];
Length[rgb21]
4664
r1121=rgb21[[All,9]];
rd1121=SmoothKernelDistribution[r1121];
rp1121=Plot[PDF[rd1121,x],{x,-10,10},PlotRange->All,PlotStyle->
  {Purple,Thick},PlotLegends->"r11_21",AxesOrigin->{0,0},LabelStyle->
  {FontFamily-> "Arial",FontSize->24,FrameLabel->{"Strain
      Rate","PDF"}},Frame->{{True,False},{True,False}},Axes->False]
Extract voxels from phase 1 that have grain boundaries with phase 1
rgb11=rgb1[[Flatten@Position[rgb1[[All,5]],1],All]];
Length[rgb11]
88578
r1111=rgb11[[All,9]];
rd1111=SmoothKernelDistribution[r1111];
rp1111=Plot[PDF[rd1111,x],{x,-10,10},PlotRange->All,PlotStyle->
  {Purple,Thick},PlotLegends->"r11_11",AxesOrigin->{0,0},LabelStyle->
  {FontFamily-> "Arial",FontSize->24,FrameLabel->{"Strain
      Rate","PDF"}},Frame->{{True,False},{True,False}},Axes->False]
Extract all rows that are not in grain boundaries
rgb0=rraw2[[Flatten@Position[rraw2[[All,6]],0],All]];
Length[rgb0]
56689
Length[rgb1]+Length[rgb0]+Length[rgb2]
262144
Extract voxels that are within grains of phase 1, no grain boundaries
rgb01=rgb0[[Flatten@Position[rgb0[[All,5]],1],All]];
Length[rgb01]
54700
r1110=rgb01[[All,9]];
```

```
rd1110=SmoothKernelDistribution[r1110];
rp1110=Plot[PDF[rd1110,x],{x,-10,10},PlotRange->All,PlotStyle->
  {Purple,Thick},PlotLegends->"r11_10",AxesOrigin->{0,0},LabelStyle->
  {FontFamily-> "Arial",FontSize->24,FrameLabel->{"Strain
      Rate","PDF"}},Frame->{{True,False},{True,False}},Axes->False]
Extract voxels that are within grains of phase 2, no grain boundaries
rgb02=rgb0[[Flatten@Position[rgb0[[All,5]],2],All]];
Length[rgb02]
1989
r1120=rgb02[[All,9]];
rd1120=SmoothKernelDistribution[r1120];
rp1120=Plot[PDF[rd1110,x],{x,-10,10},PlotRange->All,PlotStyle->
  {Purple,Thick},PlotLegends->"r11_20",AxesOrigin->{0,0},LabelStyle->{
    FontFamily-> "Arial",FontSize->24,FrameLabel->{"Strain
      Rate","PDF"}},Frame->{{True,False},{True,False}},Axes->False]
Plot all together
Show[rp1112,rp1122,rp1121,rp1110,rp1120,rp1111,PlotRange->All]
Show[rp1112,rp1110,rp1120,rp1111,PlotRange->All]
Show[rp1122,rp1121,PlotRange->All]
Plot Distribution of Stress of Specific Voxels. Triple Structure
Import stress field data
traw=Import["/Users/Loet/Documents/VPFFT/LANL_2014/3_001_110_Pv_
  110_-110MgO_30strain/Triple_30strain/StrainRateDist/dfieldstat.out",
  "Table"];
Length[traw]
262145
Remove header
traw2=Rest[traw];
Length[traw2]
262144
Calculate distribution for all voxels
td33all = traw2[[All,9]];
Length[td33all]
262144
td33alldist=SmoothKernelDistribution[td33all]
DataDistribution[<<SmoothKernel>>,{262144}]
DataDistribution[<<"SmoothKernel">>,{262144}]

DataDistribution[<<SmoothKernel>>,{262144}]
tp33all=Plot[PDF[td33alldist,x],{x,-10,10},PlotRange->All,PlotStyle->
  {Orange,Thick},PlotLegends->"edot33_all",AxesOrigin->{0,0},LabelStyle->
```

```
  {FontFamily-> "Arial",FontSize->24,FrameLabel->{"Strain
      Rate","PDF"}},Frame->{{True,False},{True,False}},Axes->False,
  TicksStyle -> Thickness[0.1]]
Extract all rows that have grain boundaries with phase 2
tgb2=traw2[[Flatten@Position[traw2[[All,6]],2],All]];
Length[tgb2]
145285
Extract voxels from phase 1 that have grain boundaries with phase 2
tgb12=tgb2[[Flatten@Position[tgb2[[All,5]],1],All]];
Length[tgb12]
87412
t1112=tgb12[[All,9]];
Length[t1112]
87412
StandardDeviation[t1112]
1.18319
ListPlot[t1112,PlotRange->All]
Histogram[t1112,{.005},"Probability",ImageSize->Large]
td1112=SmoothKernelDistribution[t1112]
DataDistribution[<<SmoothKernel>>,{87412}]
StandardDeviation[td1112]
1.18779
Median[td1112]
-0.722433
Mean[td1112]
-0.880461
tp1112=Plot[PDF[td1112,x],{x,-10,10},PlotRange->All,PlotStyle->
  {Orange,Thick},PlotLegends->"t11_12",AxesOrigin->{0,0},LabelStyle->
  {FontFamily-> "Arial",FontSize->24,FrameLabel->{"Strain
      Rate","PDF"}},Frame->{{True,False},{True,False}},Axes->False]
Extract voxels from phase 2 that have grain boundaries with phase 2
tgb22=tgb2[[Flatten@Position[tgb2[[All,5]],2],All]];
Length[tgb22]
57873
t1122=tgb22[[All,9]];
td1122=SmoothKernelDistribution[t1122]
DataDistribution[<<SmoothKernel>>,{57873}]
StandardDeviation[td1122]
1.51399
Median[td1122]
-1.50715
```

```
Mean[td1122]
-1.57446
tp1122=Plot[PDF[td1122,x],{x,-10,10},PlotRange->All,PlotStyle->
  {Orange,Thick},PlotLegends->"t11_22",AxesOrigin->{0,0},LabelStyle->
  {FontFamily-> "Arial",FontSize->24,FrameLabel->{"Strain
      Rate","PDF"}},Frame->{{True,False},{True,False}},Axes->False]
Extract all rows that have grain boundaries with phase 1
tgb1=traw2[[Flatten@Position[traw2[[All,6]],1],All]];
Length[tgb1]
74261
Extract voxels from phase 2 that have grain boundaries with phase 1
tgb21=tgb1[[Flatten@Position[tgb1[[All,5]],2],All]];
Length[tgb21]
5744
t1121=tgb21[[All,9]];
td1121=SmoothKernelDistribution[t1121];
StandardDeviation[td1121]
1.63799
Median[td1121]
-1.53792
Mean[td1121]
-1.58962
tp1121=Plot[PDF[td1121,x],{x,-10,10},PlotRange->All,PlotStyle->
  {Orange,Thick},PlotLegends->"t11_21",AxesOrigin->{0,0},LabelStyle->
  {FontFamily-> "Arial",FontSize->24,FrameLabel->{"Strain
      Rate","PDF"}},Frame->{{True,False},{True,False}},Axes->False]
Extract voxels from phase 1 that have grain boundaries with phase 1
tgb11=tgb1[[Flatten@Position[tgb1[[All,5]],1],All]];
Length[tgb11]
68517
t1111=tgb11[[All,9]];
td1111=SmoothKernelDistribution[t1111];
StandardDeviation[td1111]
1.05913
Mean[td1111]
-0.745198
Median[td1111]
-0.61126
tp1111=Plot[PDF[td1111,x],{x,-10,10},PlotRange->All,PlotStyle->
  {Orange,Thick},PlotLegends->"t11_11",AxesOrigin->{0,0},LabelStyle->
  {FontFamily-> "Arial",FontSize->24,FrameLabel->{"Strain
```

```
      Rate","PDF"}},Frame->{{True,False},{True,False}},Axes->False]
Extract all rows that are not in grain boundaries
tgb0=traw2[[Flatten@Position[traw2[[All,6]],0],All]];
Length[tgb0]
42598
Length[tgb1]+Length[tgb0]+Length[tgb2]
262144
Extract voxels that are within grains of phase 1, no grain boundaries
tgb01=tgb0[[Flatten@Position[tgb0[[All,5]],1],All]];
Length[tgb01]
41340
t1110=tgb01[[All,9]];
td1110=SmoothKernelDistribution[t1110];
StandardDeviation[td1110]
1.01267
Mean[td1110]
-0.775909
Median[td1110]
-0.654412
tp1110=Plot[PDF[td1110,x],{x,-10,10},PlotRange->All,PlotStyle->
  {Orange,Thick},PlotLegends->"t11_10",AxesOrigin->{0,0},LabelStyle->
  {FontFamily-> "Arial",FontSize->24,FrameLabel->{"Strain
      Rate","PDF"}},Frame->{{True,False},{True,False}},Axes->False]
Extract voxels that are within grains of phase 2, no grain boundaries
tgb02=tgb0[[Flatten@Position[tgb0[[All,5]],2],All]];
Length[tgb02]
1258
t1120=tgb02[[All,9]];
td1120=SmoothKernelDistribution[t1120];
StandardDeviation[td1120]
1.22804
Mean[td1120]
-1.42894
Median[td1120]
-1.37346
tp1120=Plot[PDF[td1110,x],{x,-10,10},PlotRange->All,PlotStyle->
  {Orange,Thick},PlotLegends->"t11_20",AxesOrigin->{0,0},LabelStyle->
  {FontFamily-> "Arial",FontSize->24,FrameLabel->{"Strain
      Rate","PDF"}},Frame->{{True,False},{True,False}},Axes->False]
Plot all together
Show[tp1112,tp1122,tp1121,tp1110,tp1120,tp1111,PlotRange->All]
```

```
Show[tp1112,tp1110,tp1120,tp1111,PlotRange->All]
Show[tp1122,tp1121,PlotRange->All]
Plot Distribution of Stress of Specific Voxels.
Single Phase Perovskite Random Structure
Import stress field data
rsraw=Import["/Users/Loet/Documents/VPFFT/LANL_2014/3_001_
  110_Pv_110_-110MgO_30strain/Random_30strain_001_110_Pv/fftpvsingleph/
  StrainRateStats/dfieldstat.out","Table"];
Length[rsraw]
262145
Remove header
rsraw2=Rest[rsraw];
Length[rsraw2]
262144
Calculate distribution for all voxels
rsd33all = rsraw2[[All,9]];
Length[rsd33all]
262144
rsd33alldist=SmoothKernelDistribution[rsd33all]
DataDistribution[<<SmoothKernel>>,{262144}]
DataDistribution[<<"SmoothKernel">>,{262144}]

DataDistribution[<<SmoothKernel>>,{262144}]
rsp33all=Plot[PDF[rsd33alldist,x],{x,-10,10},PlotRange->All,PlotStyle->
  {Magenta,Thick},PlotLegends->"edot33_all",AxesOrigin->{0,0},LabelStyle->
  {FontFamily-> "Arial",FontSize->24,FrameLabel->{"Strain
      Rate","PDF"}},Frame->{{True,False},{True,False}},Axes->False,
  TicksStyle -> Thickness[0.1]]
Extract all rows that have grain boundaries with phase 1
rsgb1=rsraw2[[Flatten@Position[rsraw2[[All,6]],1],All]];
Length[rsgb1]
205455
Extract voxels from phase 1 that have grain boundaries with phase 1
rsgb11=rsgb1[[Flatten@Position[rsgb1[[All,5]],1],All]];
Length[rsgb11]
205455
rs1111=rsgb11[[All,9]];
rsd1111=SmoothKernelDistribution[rs1111];
rsp1111=Plot[PDF[rsd1111,x],{x,-10,10},PlotRange->All,PlotStyle->
  {Magenta,Thick},PlotLegends->"rs11_11",AxesOrigin->{0,0},LabelStyle->
  {FontFamily-> "Arial",FontSize->24,FrameLabel->{"Strain
```

```
      Rate","PDF"}},Frame->{{True,False},{True,False}},Axes->False]
Extract all rows that are not in grain boundaries
rsgb0=rsraw2[[Flatten@Position[rsraw2[[All,6]],0],All]];
Length[rsgb0]
56689
Length[rsgb1]+Length[rsgb0]
262144
Extract voxels that are within grains of phase 1, no grain boundaries
rsgb01=rsgb0[[Flatten@Position[rsgb0[[All,5]],1],All]];
Length[rsgb01]
56689
rs1110=rsgb01[[All,9]];
rsd1110=SmoothKernelDistribution[rs1110];
rsp1110=Plot[PDF[rsd1110,x],{x,-10,10},PlotRange->All,PlotStyle->
  {Magenta,Thick},PlotLegends->"rs11_10",AxesOrigin->{0,0},LabelStyle->
  {FontFamily-> "Arial",FontSize->24,FrameLabel->{"Strain
      Rate","PDF"}},Frame->{{True,False},{True,False}},Axes->False]
Plot all together
Show[rsp1110,rsp1111,PlotRange->All,ImageSize->Large,FrameTicksStyle -> Thick]
Show[cp1111,rp1111,tp1111,rsp1111,ImageSize->Large,FrameTicksStyle -> Thick]
Show[rp1111,rsp1111,AxesOrigin->{0,0},ImageSize->Large,FrameTicksStyle -> Thick]
Show[rp1110,rsp1110,AxesOrigin->{0,0},ImageSize->Large,FrameTicksStyle -> Thick]
Microstructure Comparison Plots
Show[rp1111,cp1111,tp1111,ImageSize->Large,FrameTicksStyle -> Thick]
Show[cp1110,pp1110,rp1110,tp1110,ImageSize->Large,FrameTicksStyle -> Thick]
Show[cp1112,pp1112,rp1112,tp1112,ImageSize->Large,FrameTicksStyle -> Thick]
Show[cp1121,pp1121,rp1121,tp1121,ImageSize->Large,FrameTicksStyle -> Thick]
Show[cp1122,pp1122,rp1122,tp1122,ImageSize->Large,FrameTicksStyle -> Thick]
Show[cp1120,rp1120,tp1120,ImageSize->Large,FrameTicksStyle -> Thick]
Show[cp33all,pp33all,rp33all,tp33all,ImageSize->Large,FrameTicksStyle -> Thick]
Plot Distribution of Stress of Specific Voxels. Random Structure Single
Phase MgO
Import stress field data
rs2raw=Import["/Users/Loet/Documents/VPFFT/LANL_2014/3_001_110_Pv_
  110_-110MgO_30strain/Random_30strain_001_110_Pv/fftmgosingleph/
  StrainRateStats/dfieldstat.out","Table"];
Length[rs2raw]
262145
Remove header
rs2raw2=Rest[rs2raw];
Length[rs2raw2]
```

```
262144
Calculate distribution for all voxels
rs2d33all = rs2raw2[[All,9]];
Length[rs2d33all]
262144
rs2d33alldist=SmoothKernelDistribution[rs2d33all]
DataDistribution[<<SmoothKernel>>,{262144}]
DataDistribution[<<"SmoothKernel">>,{262144}]

DataDistribution[<<SmoothKernel>>,{262144}]
rs2p33all=Plot[PDF[rs2d33alldist,x],{x,-10,10},PlotRange->All,
  PlotStyle->{Cyan,Thick},PlotLegends->"edot33_all",AxesOrigin->
  {0,0},LabelStyle->{FontFamily->
    "Arial",FontSize->24,FrameLabel->{"Strain
      Rate","PDF"}},Frame->{{True,False},{True,False}},Axes->False,TicksStyle
->
  Thickness[0.1]]
Extract all rows that have grain boundaries with phase 1 (MgO phase which
we will call phase 2 for comparison with two phase simulations)
rs2gb2=rs2raw2[[Flatten@Position[rs2raw2[[All,6]],1],All]];
Length[rs2gb2]
205455
Extract voxels from phase 1 that have grain boundaries with phase 1
rs2gb22=rs2gb2[[Flatten@Position[rs2gb2[[All,5]],1],All]];
Length[rs2gb22]
205455
rs21122=rs2gb22[[All,9]];
rs2d1122=SmoothKernelDistribution[rs21122];
rs2p1122=Plot[PDF[rs2d1122,x],{x,-10,10},PlotRange->All,PlotStyle->
  {Cyan,Thick},PlotLegends->"rs211_22",AxesOrigin->{0,0},LabelStyle->
  {FontFamily-> "Arial",FontSize->24,FrameLabel->{"Strain
      Rate","PDF"}},Frame->{{True,False},{True,False}},Axes->False]
Extract all rows that are not in grain boundaries
rs2gb0=rs2raw2[[Flatten@Position[rs2raw2[[All,6]],0],All]];
Length[rs2gb0]
56689
Length[rs2gb2]+Length[rs2gb0]
262144
Extract voxels that are within grains of phase 1, no grain boundaries
rs2gb02=rs2gb0[[Flatten@Position[rs2gb0[[All,5]],1],All]];
Length[rs2gb02]
```

```
56689
rs21120=rs2gb02[[All,9]];
rs2d1120=SmoothKernelDistribution[rs21120];
rs2p1120=Plot[PDF[rs2d1120,x],{x,-10,10},PlotRange->All,PlotStyle->
  {Cyan,Thick},PlotLegends->"rs211_20",AxesOrigin->{0,0},LabelStyle->
  {FontFamily-> "Arial",FontSize->24,FrameLabel->{"Strain
      Rate","PDF"}},Frame->{{True,False},{True,False}},Axes->False]
Plot all together
Show[rs2p1120,rs2p1122,PlotRange->All,ImageSize->Large,FrameTicksStyle -> Thick]
Single Phase vs. Two Phase and Single MgO vs Single Pv
Show[rsp33all,rs2p33all,rp33all,ImageSize->Large,FrameTicksStyle -> Thick]
Show[rs2p1120,rp1120,cp1120,tp1120,ImageSize->Large,FrameTicksStyle -> Thick]
Show[rs2p1120,rp1120,ImageSize->Large,FrameTicksStyle ->
  Thick,PlotRange->{{-8,8},{-0.1,2}}]
Show[rs2p1120,rsp1110,ImageSize->Large,FrameTicksStyle ->
  Thick,PlotRange->{{-8,8},{-0.1,2}}]
Show[rsp1111,rp1111,ImageSize->Large,FrameTicksStyle ->
  Thick,PlotRange->{{-8,8},{-0.1,2}}]
Show[rs2p1122,rp1122,ImageSize->Large,FrameTicksStyle ->
  Thick,PlotRange->{{-8,8},{-0.1,2}}]
Show[rs2p1122,rp1122,cp1122,tp1122,ImageSize->Large,FrameTicksStyle -> Thick]
Show[rsp1111,rp1111,ImageSize->Large,FrameTicksStyle ->
  Thick,PlotRange->{{-8,8},{-0.01,0.5}}]
Show[rsp1110,rp1110,ImageSize->Large,FrameTicksStyle ->
  Thick,PlotRange->{{-8,8},{-0.01,0.5}}]
```